1-1-1994

The masses and distances of planetary nebulae.

David, Buckley
University of Massachusetts Amherst

THE MASSES AND DISTANCES OF PLANETARY NEBULAE

A Dissertation Presented

by

DAVID BUCKLEY

Submitted to the Graduate School of the
University of Massachusetts Amherst in partial fulfillment
of the requirements for the degree of

DOCTOR OF PHILOSOPHY

September 1994

Department of Physics and Astronomy

THE MASSES AND DISTANCES OF PLANETARY NEBULAE

A Dissertation Presented

by

DAVID BUCKLEY

Approved as to style and content by:

Stephen E. Schneider, Chair

Ronald L. Snell, Member

Morton M. Sternheim, Outside Member

John F. Dubach, Department Head
Department of Physics and Astronomy

Acknowledgments

The route to this Ph.D. has been a circuitous one. I was first accepted as a grad student in Astronomy at UMass way back in 1981. But Penn State offered me a TA first – plus they had big-time college football (a passion of mine) – so I went there for my Masters. Feeling a bit burned out after 2 years, I went for the bucks and the yuppie career. I worked at RCA aerospace satellite division for two great years doing remote sensing, but the third year they wanted to turn me into a "star-warrior" and I didn't like living for the weekends so I looked for an academic job. I got a temporary position as the resident astronomer at SUNY Oswego making far less than I was before, but it felt like the right move. As it turned out it was; I met my wife Carolyn there in the fall of '86. Needless to say it was the best move and best year of my life. Naturally, I had to get a Ph.D. to get a permanent academic position, so I re-applied to UMass. (It might have been more expedient to go back to Penn State, but 2 years in State College, PA is enough for one lifetime, thank you! Plus I felt I would learn more if I was exposed to another program.) So that's how I got back here. Of course after 2 years here I had a family and was broke; so it was a choice of going back into industry and quitting (kind of a waste, really) or get a teaching job that would allow me to finish "in-absentia". So I did the latter. It has not been an especially easy route, working full time and doing a thesis. But I woudn't trade the last four years for anything. (Well... maybe not for *anything*, but I wouldn't trade them for, say, being a full time graduate student.) I've taught astronomy to about 1500 students in that time – and some of them even learned it! I even had my first "advisee" go on to grad school in astronomy at Wichita State. So it's been a rewarding, if stress-filled, four years.

So where are the acknowledgements!? (Sorry, this may be my only chance to ever tell my life's story.) Here they come. First the professional ones. My biggest professional thanks, of course, goes to Steve Schneider. It's not impossible to do a dissertation "in abstentia", but you have to be lucky enough to find an exceptional advisor to succeed. To say I couldn't have done it without his guidance and help is a tremendous understatement. I am also grateful to him for taking me on as a student even when he was against the "in-absentia" deal in the first place. In retrospect, he was probably right. It would've been much easier if I had large blocks of uninterrupted time to work on this thesis. But I will be forever grateful to him for giving me a shot anyway, and showing such a great deal of interest and involvement in the project. I owe my career to him more than any other person. I also want to thank my "consultant" David Van Blerkom, especially for helpful discussions to help set up this project in the first place, for his healthy skepticism and for being an all around good-guy! There are numerous other faculty to thank: Ron Snell for keeping me scared that I might not make it (and of course, for serving on my committee)! Mort Sternheim for cheerfully accepting to be a last minute replacement on my committee. Big thanks go to Jim Walker for helping me with various administrative problems (even up to the last couple of weeks) and for his guidance in helping me get my masters degree in physics. Also thanks go to: Bob Krotkov for originally being on my committee during my thesis proposal. John Kwan for a brutally difficult but brilliantly useful Astrophysics II course. Ted Harrison for Astrophysics I and for being someone to look up to. Pete Schloerb for not complaining when I did very little work on a summer assistantship for him because of last minute problems with my second year project and my son's health problems in the summer of '90 (I still feel guilty about that). And Tom Arny for his publisher leaving mars, starburst and milky way bars on my office doorknob at ESU one morning while hawking his text book.... but mostly for reviewing Chapter 1 and being a nice guy.

As for my fellow grad students, how can I remember all the help? Thanks to Pat Knezek, mostly for just being a good friend. Thanks to Ted Bergin for helping me unravel the mysteries of supermongo; to John Spitzak and James Case for miscellaneous computer help; to John Carpenter especially for helping me with the LaTeX thesis macros and other computing intricacies; to Doug McGonnigle for help with optics problems; to Lori Allen for giving me lots of useful references; and to Mark Horvath for studying problems with me for the quals (the most difficult month of my life – up to now).

I also want to thank my department chairpersons at E. Stroudsburg University, Dr. Illa Shwe and Dr. Mary Ann Mogus for setting up my teaching schedule in a way that allowed me to do my dissertation research (and for travel money to go to the Innsbruck PN conference in '92 and Arecibo in Jan. '94). Also, thanks to Dr. Paul Kicska, who recently passed away, for heading the search commitee that hired me. Thanks also to the other Physics Dept. faculty at ESU (P. Houle, J. Cheng & T. Wagner) for helping me along when I was getting my feet wet. And thanks to my "student" Tim Lawlor for helping with some of the tedious data collection used in Chapter 5. Also, I should thank my friend and former mentor at RCA, Dave Hogan. Many of the coding techniques that helped me write the computer programs necessary for this thesis were learned under his "tutelage". Long live FORTRAN!

Most of all, I want to thank my family. First my loving and supportive wife Carolyn for getting on this ride with me in the first place. (I'm not sure she knew what she was in for!) She has been an absolute pillar of strength for me whenever I needed her, from taking that lousy insurance company job to support us in '88 and '89, to moving the family back forth from PA to western Mass, to helping me cope with the stress of finishing this Thesis. I hope I can give her half the support in her future academic endeavors that she has given me. I could not have done it without her – and I really mean that sincerely. This degree is equally hers. Second,

but really 1-A, I thank my Mom and Dad. From encouraging my interests as a kid (buying me my first telescope and letting me stay up late to watch the moonwalks), to understanding when I gave up my aerospace carreer to take a temporary job, to bailing us out when we needed some cash – they have always been there for me and have been unquestioningly supportive. Finally, but not least, I want to thank my wonderful kids, Tristan and Trudyann. It's probably logistically about 10 times easier to get through grad school if you don't have kids. But the emotional lift and love they give me makes up for that a hundred fold. I am more proud to be their Dad than anything else in my life.

And, of course, I thank God for all of the above.

Abstract

THE MASSES AND DISTANCES OF PLANETARY NEBULAE

September 1994

David Buckley, B.A., Rutgers University

M.S., Pennsylvania State University

M.S., University of Massachusetts Amherst

Ph.D., University of Massachusetts Amherst

Directed by: Professor Stephen E. Schneider

Planetary nebulae (PNs) that evolve from relatively high mass progenitor stars can "masquerade" as low mass objects. We simulate the evolution of PNs and their central stars based on simple models, using various wind speeds and mass loss rates. Even when our nebulae become ionized beyond the characteristic dense inner shell, a faint halo can comprise most of ionized matter while contributing little luminosity. For such PNs, standard techniques severely underestimate ionized mass. Curiously, ionized masses that would be observationally derived for our model nebulae ("Shklovsky masses") are insensitive to variations in the model's input parameters. For evolved PNs, the Shklovsky mass remains a few tenths of a solar mass, despite the total ionized mass varying over two orders of magnitude in our simulations. We show that this is consistent with the range of masses determined for PNs with independent distance estimates. This small mass variance should produce only ~30% distance errors using Shklovsky's constant mass method and may explain why this method is successful despite the incorrect assumption of low ionized mass.

We describe a new distance method for PNs based on a theoretical/empirical relationship between their radii and radio surface brightnesses. This method requires only readily available radio flux and angular size measurements. We use Galactic bulge PNs along with PNs with independent distances to establish, calibrate, and

test this method. Our distance method appears to yield errors of only $\sim$20% using the best available data. We also find that the Shklovsky method predicts the distances of large, low surface brightness PNs well, but overestimates distances of smaller PNs.

We have also made deep radio observations of two PNs, NGC 6804 and NGC 6826, to examine their halo masses. Despite large dynamic ranges, we detect inner halos of both nebulae. Derived halo-to-shell mass ratios demonstrate that the halos contain >60% of the total ionized mass while contributing <25% of the emission.

We further test our distance method by comparison with kinematic distances derived using measured radial velocities of a sample of PNs. Our method agrees with Galactic kinematics within limits of measurement uncertainties and velocity dispersion.

Table of Contents

List of Tables

List of Figures

Chapter 1

Introduction and Motivation

The name "planetary nebula" conjures up images of planets; perhaps planets condensing from a nebular cloud in much the same way that our solar system is thought to have formed. In fact, in the early 1800's this was a scenario that was thought to be plausible, until the expansion of the nebular shells were discovered. But planetary nebulae do not form planets; in fact they have nothing at all to do with planets. The name "planetary nebula" is a relic of visual astronomy. Over 200 years ago, William Herschel coined the term because he thought these objects resembled the appearance of distant planetary disks in a telescope. In reality, planetary nebulae are glowing gaseous envelopes ejected from red giant stars. The ejected gas is heated and ionized by high energy photons from the exposed core of the dying star, resulting in a visible spectrum which is rich in emission lines. There is, of course, much more to understand about PNs. In this Chapter, we hope to give a general overview of PNs, stressing the properties and problems that we try to address in this dissertation.

Morphologically, PNs are an odd lot. Herschel was the first to conclude that PNs were actually gaseous shells when he detected a centrally located star in an extended "atmosphere" in the PN that would later be catalogued as NGC 1514 (see Pottasch 1984). The star, he thought, was too perfectly centered to be a chance alignment, and the nebulosity was too faint and diffuse to be a collection of stellar objects. Many PNs show this classical ring or shell-like structure which is either circular or slightly flattened with a hot star located directly in the center. Those that are flattened or elongated tend to be brighter at the end of their short

axis and dimmer at the end of their long axis (see Gurzadayan 1969). Some PNs that are much brighter along one axis appear bipolar. There are many variations of these broad descriptions, making PNs impossible to easily classify. In addition, there are often peripheral structures such as double-shells and giant halos around many PNs (see Kaler 1985).

Spectroscopically, PNs have been extensively studied for almost 150 years. In fact, it is their strong emission lines that distinguish PNs from other galactic sources and make detection of unresolvable PNs possible. PN spectra classically consist of hydrogen and helium recombination lines along with collisional lines of other relatively light elements and ions. Doppler shifts of these spectral lines show that PN shells exhibit expansion velocities typically on the order of $\sim$25 km s^{-1}. These typical expansion velocities, coupled with measurements of PN radii (typically on the order of a few tenths of a parsec) imply ages of PNs on the order of $\sim 10^4$ years. This, along with the population statistics of PNs throughout the galaxy, suggests that the PN stage is an extremely brief portion of a star's overall evolution.

A significant early clue to the nature of PNs was the fact that the optical luminosity of the glowing nebula is generally much greater than that of the central star (sometimes called the PN nucleus or PNN for short). The mystery of the energy source was solved by Hubble in 1922, who showed that all nebulae ultimately glow by the light from stars; either by reflection or atomic excitation and ionization (see Khromov 1988). In 1927, Zanstra expanded on this idea by showing that PN shells glow by fluorescence (see Gurzadayan 1969): the nebular gas absorbs high energy ultraviolet (UV) radiation from the PNN and redistributes this energy into visual wavelengths through atomic recombination lines. This also shows that PNNs emit the great majority of their radiation in the ultraviolet, suggesting that they are exceptionally hot stars.

Zanstra's method estimates PNN temperatures by their recombination line fluxes, which are directly related to the total UV radiation absorbed by the nebula. This method assumes, however, that all the UV radiation is absorbed by the nebula; that is, the PN is "optically thick" to UV radiation. Since some PNs are believed to be thin enough to let some of this UV radiation escape (i.e. "optically thin" in the UV), this method gives only a lower limit to the temperature of the PNN. Still, Zanstra showed that this method implies temperatures for PN central stars typically between ~80,000 K and ~150,000 K; much greater than the hottest main sequence stars (~50,000 K). In fact PNNs are the hottest stellar objects known. These high temperatures, when combined with distance estimates, also show the that PNNs are very luminous, often approaching the total or "bolometric" luminosities of main sequence O and B stars, although their visual brightness is usually significantly lower since most of their energy output is in the UV.

1.1 The Evolution of Planetary Nebulae

In the late 1950's, Shklovsky noted the similarity of the spatial distribution of PNs within our galaxy to that of red giant stars. He therefore proposed that PNs were derived from red giants (Shklovsky 1978). The formation of a nebular shell containing only a few tenths of a solar mass was thought to occur by a single ejection event during the red giant phase, possibly caused by radiation pressure or thermal pulses.

In the past decade or so, it has become clear that the ejection of the nebular shell is not a single event, but is likely the result of a relatively continuous high-mass stellar wind ($\sim 10^{-5}$ - 10^{-4} $M_{\odot}$ yr $^{-1}$, ~10 km s^{-1}) during the asymptotic giant branch (AGB) stage of stellar evolution (Kwok *et al.* 1978). The remnant shell, expanding into the interstellar medium, remains neutral until

almost all of the star's envelope is lost and the hot core is exposed. The exposed PNN quickly ionizes the inner portion of the remnant AGB wind. UV observations (Cerruti-Sola & Perinotto 1985) have also shown that many PNN's exhibit a relatively low-mass but high velocity "fast wind" ($\sim 10^{-7}$ $M_{\odot}$ yr^{-1}, $\sim$2000 km s^{-1}) ; which is thought to be caused by resonant line absorption of UV photons by the gas in the meager envelope that remains after the cessation of the superwind. The fast wind rapidly overtakes the more slowly expanding remnant AGB wind, but retains its momentum as it sweeps up material from the inner edge of the AGB material, causing a "snow-plow" effect. This bunching-up of the remnant AGB wind results in a relatively high density shell around the central star, generally expanding at a terminal velocity of a few tens of km s^{-1}. As long as the fast wind continues to dump momentum into the dense shell, the shell continues to increase in mass as it propagates outward into the lower density remnant. This is the essence of the interacting stellar winds (ISW) model (Kwok 1982).

Concurrent with the expansion of the nebular shell, the central star is rapidly evolving. Theoretical models by Schönberner (1981) and others suggest that the PNN initially evolves at constant luminosity but rapidly increasing temperature (see Figure 1.1). Clearly, this increases the amount of ionizing radiation dramatically. One would expect the PN's ionization region to grow substantially during this phase. As the PNN finally exhausts its fuel supply, it begins to drop in luminosity and slowly cool.

One therefore expects the amount of ionized mass in the PN shell might reach a maximum somewhere near the time that the PNN curve reaches its maximum temperature. As the PNN luminosity drops, so would the ionized mass of the PN shell. However, as the shell continues to grow its mean density decreases. Thus, during the later stages, the growth of the nebula should be dominated by the

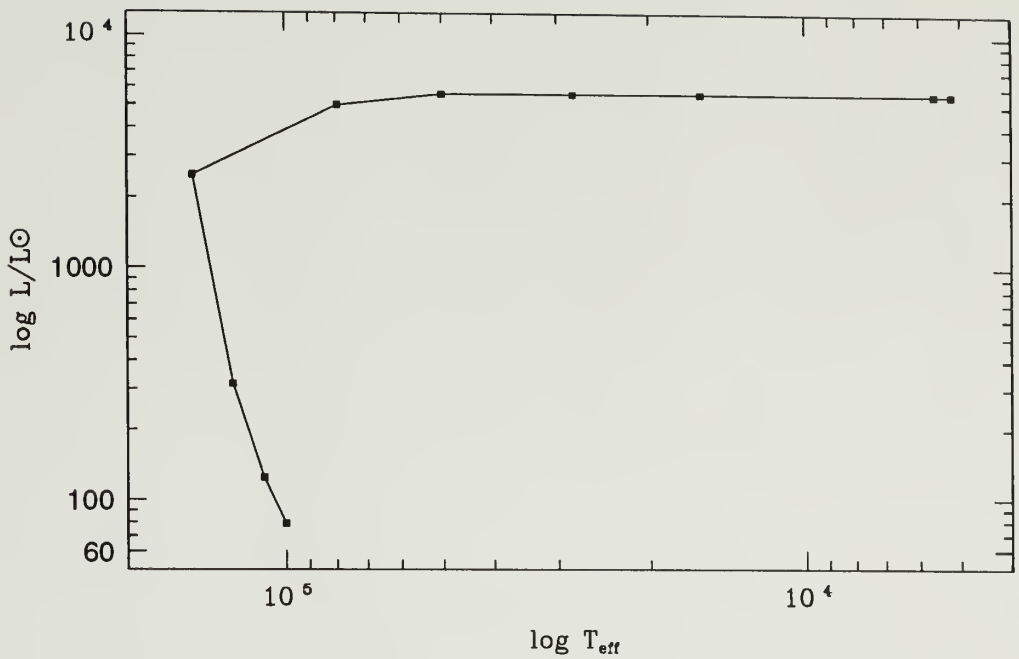

Figure 1.1. Evolution of a 0.6 $M_{\odot}$ PN central star (from Schönberner 1981). The time steps, in thousands of years are (upper right to lower left): 0, 1, 2, 3, 4.5, 6, 9, 10, 12, 40.

expansion; the lowered density makes the shell easier to ionize by reducing the rate of recombinations (which roughly goes as the square of the electron density). We therefore expect the growth and decline of planetary nebulae to be determined by the interaction between the expanding outer envelope and the evolving central star.

1.2 Masses of Planetary Nebulae

Until recently, planetary nebulae were thought to form from relatively low mass ($\sim$1 $M_\odot$) progenitors. While the mass distribution of PNN's peaks rather sharply at $\sim$0.6 $M_\odot$ (Weidemann 1989) and the ionized mass of the PN shell rarely exceeds a few tenths of a solar mass, it now appears likely that the mass of a typical PN progenitor may be significantly higher than the sum of the PN's observationally determined ionized mass and central star mass. It seems, in fact, that PNs may evolve from progenitor stars with masses up to $\sim$8 $M_\odot$ (Weidemann and Köester 1983), contrary to what is commonly taught in introductory astronomy text books!

Theoretical studies by several authors suggest relatively high mass progenitors for PNs (see Bedijin 1988, for example). The observed mass distribution of white dwarfs, like PNNs, also peaks at $\sim$0.6 $M_\odot$ (Weidemann and Köester 1983). For this and other reasons, PNNs are thought to be the precursors of white dwarfs (WDs). Initial–final mass relations for white dwarfs can be determined empirically for white dwarfs in clusters of known age. A lower limit to the progenitor mass for a WD in a cluster is estimated by presuming that the white dwarf's initial mass must be greater than the mass of stars at the cluster's turn-off point. If a cluster WD mass and approximate cooling age is known spectroscopically, one can then backtrack to the age of the cluster when the star was on the AGB. The progenitor's mass can then be estimated from theoretical evolutionary ages of AGB stars as a function of mass. Weidemann and Köester used this method to

find an empirical initial-final mass relation for white dwarfs in clusters that suggests that WDs and, by inference, PNNs are produced from progenitor stars in our galaxy with masses in the range of roughly 2 to 8 $M_{\odot}$.

Shells of neutral atomic and molecular material have also been found surrounding many PNs in the last decade or so (see Dinerstein 1991 for a review), but the total masses of neutral shells discovered thus far at best account for only on the order of a tenth of a solar mass. Thus, it appears that a PN arises from a progenitor of several solar masses. The resulting nebula typically contains a central star of $\sim$0.6 $M_{\odot}$, a shell of $\sim$0.2 $M_{\odot}$ and, in some cases, neutral material amounting to less than $\sim$0.1 $M_{\odot}$. This leads to the obvious question: *where is all the mass hiding if the progenitor mass is so much greater than the visible mass of the PNN and the surrounding gas?*

1.3 Distances of Planetary Nebulae

Distance is absolutely fundamental to our understanding of the nature of PNs. The quantitative determination of intrinsic PN properties like mass, size and luminosity described above is closely dependent on the measurement of PN distances. Yet the distance problem has remained a conundrum for quite some time. Virtually all PNs lie at distances beyond the reach of direct geometric parallax measurements. Also, since the central stars of PNs cannot be readily classified according to temperature and luminosity, as main sequence and giant stars are, it is impossible to estimate their distances via temperature classification (spectroscopic parallax). A handful of PNs lie in clusters of known distance or have companion stars of known spectral characteristics, but such cases are rare and there are not enough of them to utilize their distances to determine general properties of PNs.

"Expansion distances" can be obtained by equating a PN's long term angular expansion with its measured doppler expansion. However, this rests on the somewhat uncertain assumption that the observed angular expansion is due just to the physical expansion of the material in the PN shell. The observed expansion could be caused by the propagation of an ionization front through the shell. There could be geometrical effects as well. For example, the PN might be expanding at a different rate across the line of sight (angular expansion) than along the line of sight (doppler expansion).

Interstellar reddening or extinction caused by dust grains in the galaxy can give clues to a PN's distance if it lies near the Galactic plane. This is a painstaking process, however, since a calibrated extinction–distance diagram must be built for the line of sight to each PN measured. This is done by measuring spectroscopic distances and reddening (B-V excesses) for stars within $\sim 1°$ of the PN being measured (see Pottasch 1984). The stars measured should have a range of distances, the more distant stars showing more reddening and the nearer stars showing less. The color excess of the PN then places it along the extinction–distance curve that has been calibrated using the stars in the vicinity of the PN, giving a distance estimate for the PN.

Some interesting astrophysical methods have recently been developed. One such method compares PNN absorption line profiles with profiles predicted by model atmospheres. Such a comparison yields estimates of the effective temperature and surface gravity of the star. If a stellar mass is assumed, this information gives the approximate size and luminosity of the central star. A simple comparison, then, with the star's apparent magnitude gives an estimate of the distance. The limiting factors in this method are the accuracy of the surface gravity measurements and the presumed model atmosphere (see Pottasch 1984). More recently, Zhang & Kwok (1992) obtained distances in a similar way, but by

using evolutionary model PNs very similar to the ones we use in Chapter 2. The advantage of their method is that the PNN temperatures, surface gravities and luminosities are determined via the analysis of distance independent parameters.

These methods for determining individual PN distances often require meticulous observations and exhaustive analyses that are subject to possible biases. Therefore much of PN research has continued to rely on simpler and more generally applicable techniques that require only straightforward, direct measurements of PNs. For the most part these general "statistical" distance methods are variations of the method developed by Shklovsky in the late 1950's.

The Shklovsky distance method relies on two major assumptions. First, it assumes that all PN shells are fully ionized (density bounded). Essentially, this says that the PN has run out of material to ionize, so that any expansion of the nebula is caused by the physical expansion of the shell. Thus, for the fully ionized shell, the total mass stays constant and, since it is fully ionized, the product of the electron density (n_e) and the volume (V) of the shell remains constant as the shell expands ($n_e V = constant$). The flux density of a PN depends on the square of the electron density (n_e^2), the volume (V), and inversely on the square of the distance (d^2). The total flux density S_ν from an optically thin nebula is therefore dependent on the ionized mass M_i, radius r, and distance d as:

$$S_\nu \propto \left(\frac{M_i}{r^3}\right)^2 r^3 \frac{1}{d^2} \tag{1.1}$$

ignoring various terms that appear to vary only weakly from PN to PN (see Chapter 2). Thus, the flux from an expanding PN of a given mass will decrease inversely as the volume ($S_\nu \propto r^{-3}$). A more useful expression can be found by rearranging the terms and substituting for the angular radius θ ($\propto r/d$), and solving for the distance in terms of the ionized mass and observable quantities:

$$d \propto M_i^{2/5} S_\nu^{-1/5} \theta^{-3/5} \, . \tag{1.2}$$

This expression can also be rewritten in terms of distance independent observable quantities of angular radius θ, and mean surface brightness $I_\nu = S_\nu/(\pi\theta^2)$ at radio wavelengths:

$$d \propto M_i^{2/5} I_\nu^{-1/5} \theta^{-1} \ . \tag{1.3}$$

The difficulty with the above expression, however, is that it is only useful if we know *a priori* the ionized mass of the nebula. This leads us to the second major assumption of the Shklovsky method; namely, all PNs have essentially the same ionized mass (usually assumed to be $\sim$0.2 $M_\odot$).

This is the essence of the Shklovsky method. The distance of a fully ionized, density bounded nebula depends only upon its mass and the two observables: flux density and angular size. Since distance is only weakly dependent on mass, an error in the assumed ionized mass does not introduce a large errors in distance. Classically, a scaling factor is introduced by using nearby PNs with independent distance determinations. This, however, often leads to propagation of uncertainties from the independent distance estimates for these few nearby calibration nebulae. We show in Chapters 2 and 3 that the Shklovsky method and variations thereof work quite well, within the limits of observational error, when compared with PNs of independently determined distance. We also show, in Chapter 3, that a modified method based on angular radius rather than mass, yields even better results than the classical mass-based Shklovsky method.

1.4 Motivation and Overview

The study undertaken in this dissertation was prompted by two related questions. (1) *How do planetary nebulae derived from progenitor stars of several solar masses "masquerade" as low mass objects?* and (2) *Why does the Shklovsky distance method work at all when its fundamental assumptions of a low mass*

($\sim$0.2 $M_\odot$), density bounded fully ionized nebula may be completely wrong? An additional motivation was the possibility of using PNs as distance indicators to be used for mapping the outer galactic rotation curve.

A possible answer to the above questions, we presumed, might be found in studying the interaction between the expanding PN envelope and radiation field of the rapidly evolving central star. Several investigators (Kwok 1985; Dopita and Meatheringham 1990) have modeled the evolution of the ionized shells of PNs using theoretical models of the evolving PNN. However, of all of the evolutionary models we had seen at the beginning of our study, none of them began with neutral envelopes of several solar masses. We thought that perhaps the evolutionary history of the central star and expanding massive envelope together might hold the key to understanding why so little ionized mass is observed in PNs.

We present our investigation of the evolution of planetary nebulae in Chapter 2. We examine the possible connection between PN evolution and their observationally determined ionized masses by simulating the evolution of PNs from high mass progenitors using published central star models and a computer code based on the interacting stellar winds model. We find that the total ionized *mass* of the simulated PNs vary wildly depending on the wind parameters and central star models used. However, we find that most of the *emission* of the PN comes from the relatively low mass, dense shell that has been "snow plowed" by the fast wind. Even when several solar masses of material beyond this dense shell is ionized by the central star, it generally forms a very low surface brightness halo, contributing only a small fraction of the PN's total emission. Such halos are normally not considered when making standard estimates of PN masses. Curiously, the mass discerned by an observer of any of our simulated PNs using the standard methods (a mass we call the "Shklovsky Mass") would always remain on the order of a few tenths of a solar mass. This result seems to be invariant,

regardless of wind parameters or central star models input to the simulations. We also show that these masses are consistent with masses derived for a sample of PNs with independent distances when observational uncertainties are properly taken into account.

In Chapter 3 we use our simulated nebulae along with a "local" sample of PNs with independent distances and a sample of PNs in the galactic bulge to derive a new distance method based on a relationship between PN radius and radio surface brightness. We show that the radius–surface brightness relationship found for our simulated PNs agrees well with both the bulge and local PNs. Since surface brightness is a distance independent quantity, and the relation between a PNs physical radius and angular radius depends only on the distance, the connection between radius and surface brightness makes it possible to determine distance using measurements of easily observable quantities: radio surface brightness and angular radius. We test the accuracy of this method and find that it is accurate to better than $\sim$25%. We also use these samples of PNs with independent distance to demonstrate that the Shklovsky method does, in fact, do well in predicting distances of large, low surface brightness PNs.

In Chapter 4 we explore the viability of deep radio synthesis images for determining the masses of faint PN halos. We describe the observation and analysis of two PNs with known optical halos, NGC 6804 and NGC 6826, using the Very Large Array. For both objects, we detected the inner halos and found that these faint halos contain roughly twice the mass of the bright inner shells while accounting for less than a quarter of the total radio continuum emission.

We further test our new distance method in Chapter 5, by applying it to PNs with accurately measured radio-derived angular radii and known radial velocities. We then test how well this distance method agrees when tested against galactic kinematics. We find that, with the exception of a few outliers, our method does

well (within the uncertainties due to the PN population's velocity dispersion) in placing these PNs along the Galactic rotation curve.

Chapter 6 summarizes the results from our study of PN evolution, masses and distances. We also present some initial results from our investigation into the properties of young PNs, and how these results impact on our previous studies. We then present a few future prospects for research relating to the study of planetary nebulae.

Chapter 2

The Ionized Mass of Planetary Nebulae

2.1 Introduction

Several lines of evidence indicate that planetary nebulae (PNs) arise from higher mass progenitors than has been classically assumed, probably from stars averaging to several solar masses. Such masses require that for many (although by no means all) PNs, a substantial amount of material must be contained in the nebula surrounding the central stars, since these PN nuclei (PNNs) have, with few exceptions, masses no greater than 0.7 $M_{\odot}$. Yet it is generally found that PNs have $\lesssim$0.5 $M_{\odot}$ of ionized gas, and, while recent searches have detected molecular gas in many PNs and atomic hydrogen in a few, the amount of neutral gas found is too small to balance the mass budget. This "missing mass" problem has confounded attempts to reconcile the population statistics of PNs with their individual characteristics.

Given the mass discrepancy in PNs, it is particularly puzzling that the Shklovsky method for determining distances has been so successful. The method is based on the assumptions that PNs are fully ionized ("density bounded") and that the ionized mass is a constant equal to only $\sim$0.1 $M_{\odot}$. Many authors apologize that the method should not yield distances to better than a factor of $\sim$3 (see, for example, Cahn, Kaler, & Stanghellini 1992), yet it remains widely used since direct tests show it to yield distances that are accurate to $\sim$30% (1σ) both based on statistical comparisons with kinematic distances derived from Galactic rotation (Schneider & Terzian 1983) and based on PNs located in the Galactic bulge

(Stasinska *et al.* 1991). We also demonstrate here (§ 2.2) that the Shklovsky method yields good agreement with independent distances measured for a sample of relatively nearby PNs studied by Gathier (1987)—a sample which has sometimes been used to argue against the Shklovsky method!

In this chapter we show how there can indeed be large masses in PN envelopes, sometimes fully ionized and sometimes not, but that the Shklovsky method can still work successfully despite its basic assumptions all being wrong. In effect, PNs can evolve from relatively high mass progenitor stars and still appear to have consistently small masses.

Our approach is based on computational simulations of PN evolution which predict the radio emission at frequencies where the PNs are likely to be optically thin. We employ the simple momentum-conserving model of Kwok, Purton, & FitzGerald (1978), but we also demonstrate that our results are consistent with a more sophisticated hydrodynamical model. This simple model does not reproduce any of the rich variety of morphologies that PNs exhibit, but we are interested primarily in just the total radio emission and the overall radii of the dense "snow-plowed" region of the PNs, and the momentum-conserving model is adequate to this task. Our goal here is to demonstrate the stability of observable parameters that the simulated PNs show even when their wind and other input parameters are allowed to vary over a very wide range. In Chapter 3, we will demonstrate that these simulated PNs also *quantitatively* reproduce the basic observables of real PNs.

Our study differs from previous ones in two important respects: First, we assume the PNs arise from relatively high mass progenitors, which result in nebular envelopes with masses $> 1 M_{\odot}$ —most previous papers truncate the PNs' envelopes at a few tenths of a solar mass to be consistent with the commonly quoted observational data on nebular masses. Second, we carry our analysis through the

additional step of "observing" our simulated nebulae and ask what ionized mass would be estimated if the resulting data were analyzed using standard techniques. We will attempt to demonstrate that the standard observationally-derived values for the ionized mass do not represent the true ionized masses of the nebulae, but that these observationally-derived values do share some interesting properties that allow them to be used as good distance indicators.

The range of expected nebular masses can be estimated from the characteristics of PNNs in a roundabout way. Based on stellar evolution calculations and observations of PNNs, the final masses of the great majority appear to lie between 0.55 and $0.65 M_{\odot}$ (Schönberner 1981; Weidemann 1989), although depending on the distance scale the assumed the masses might be as much as $\sim$0.1 $M_{\odot}$ higher (Heap & Augensen 1987). The progenitor masses of white dwarfs can in turn be estimated in clusters based on the cluster turn-off ages and the white dwarf cooling ages. In the 0.55–$0.65 M_{\odot}$ mass range, the estimated progenitor masses mostly lie between 2 and 4 $M_{\odot}$ (perhaps in one case as high as 6 $M_{\odot}$); there is also some suggestion of larger progenitor masses for larger PNN masses within this range (Weidemann & Koester 1983; Weidemann 1987). This would suggest that the majority of PNs should be surrounded by remnant envelopes in excess of $\sim 1.4 M_{\odot}$, although Weidemann (1987) proposes that $0.55 M_{\odot}$ PNN's may arise from stars as small as $1 M_{\odot}$.

Large masses for PN progenitors are also supported by theoretical calculations and population statistics. For example, Blöcker and Schönberner (1993) calculate the evolution of a $3 M_{\odot}$ star from the main sequence, through 9 thermal pulses in the AGB stage. The remaining PNN has a mass of $0.61 M_{\odot}$, which results in a remnant envelope with a mass in excess of $2 M_{\odot}$. And using death rates of main-sequence stars and the observed birthrates of PNs, as well as their low

average distances from the Galactic plane, Mallik (1985) argues that PNs have relatively high mass progenitors, up to approximately $8M_{\odot}$.

Because of the longstanding belief that the ionized masses of PNs were small, in the past few years there have been several searches for outer envelopes of neutral gas. In searches at 21 cm, a few PNs have been found to possess shells of atomic hydrogen (Schneider *et al.* 1987; Taylor *et al.* 1990), but the detections (and the upper limits) indicate there is generally $< 0.1M_{\odot}$ of atomic hydrogen. Detections of molecular material (e.g., Pottasch *et al.* 1987; Huggins & Healy 1989; Zuckerman *et al.* 1990) demonstrate that H_2 is more commonly present around PNs than H I. Molecular material has been found around even some well-evolved, extended planetaries that would traditionally be assumed to be fully ionized or "density bounded" (Huggins & Healy 1986; Zuckerman & Gatley 1988). However, the additional mass of these neutral envelopes again appears to account for only a fraction of a solar mass so that they do not yet "balance the mass budget."

The identity of the "missing mass" may already be suggested by deep optical images, which show that *most* PNs are surrounded by low surface brightness emission (Jewitt, Danielson, & Kupferman 1986; Chu, Jacoby, & Arendt 1987; Balick *et al.* 1992). The existence of faint outer shells has been known for many decades, but it has not been fully appreciated that the strong dependence of optical and radio emission on the local gas density allows a substantial amount of ionized mass to be present in PN halos without significantly contributing to the total emission. Detailed analyses have been carried out only recently for a few PN halos, which have shown that they can contain more mass than the highly visible inner core of the PNs (Manchado & Pottasch 1989; Plait & Soker 1990; Middlemass et al. 1991). Some optical halos may represent reflection nebulosity due to dust (Zuckerman & Gatley 1988), but we have recently observed the extended radio emission around NGC 6804 and NGC 6826, which provide even

more direct evidence that the halos contain more mass than the bright inner regions (see Chapter 4).

In PNs where no neutral gas has been detected, a large mass for the progenitors suggests that there should be several solar masses of ionized gas in the PNs. On the surface, this appears contradictory to the usual conclusion reached using the Shklovsky method which concludes that an ionized nebular mass of $\sim$0.1 $M_{\odot}$ is typical. And in the PNs where neutral gas has been found, the density-bounded assumption of the Shklovsky method is clearly contradicted. Yet after reviewing the Shklovsky method in § 2.2, we will show that it gives distances consistent with independent distance estimates to within $\sim$30% (1σ). However, the question arises: *Why does the Shklovsky method work at all if its fundamental assumptions are violated?*

In § 2.3, we describe the computer simulations we have employed, and in § 2.4 we use these simulations to examine how the basic observational parameters of PNs with envelopes of several solar masses might be affected under a variety of nebular conditions. This simple computer model exhibits a variety of behaviors like high-mass ionized halos that contribute little emission compared to the inner dense shell, and old nebulae in which recombination has occurred within the dense shell. What is remarkable is that for a wide range of wind parameters, and for a variety of possible PNNs, the apparent ionized masses one would derive through standard observations and analysis procedures remain almost always of order a few tenths of a solar mass. In fact in one of our simulations there is no fast wind and therefore no dense shell formation, yet the radii and masses still remain consistent with the other simulations!

Our computer simulations show that PNs can easily be mistaken for objects having much smaller ionized masses because of a combination of observational practices and analysis procedures used in the Shklovsky method that effectively

ignore the outer ionized envelopes. This misestimation is caused primarily by three factors: (1) the precipitous drop in (both optical and radio) surface brightness beyond the dense inner part of the ionized shell usually leads to an underestimate of the PN's actual ionized radius; (2) the halo may contain many times the mass of the dense inner shell and still contribute only a small fraction of the PN's luminosity; and (3) filling factors are often inappropriately used, and they rarely reflect the contribution of the halo gas even when a halo radius is used. Remarkably, the ionized masses of the model PNs estimated by the current procedures remain roughly constant throughout most of the observable lifetime of a PN and across a wide range of nebular conditions. This nearly constant, erroneously derived mass allows one to determine distances surprisingly well through the Shklovsky method; we therefore dub it the "Shklovsky mass."

We discuss the relationship of our simulated PNs to real PNs in § 2.5, in particular considering aspects of the nebular geometry that are not modeled. Finally, we summarize the main points of this chapter in § 2.6.

2.2 Ionized Masses of PNs

Estimates of the ionized masses of PNs are often made for PNs with independently known distances based on their H–α or radio continuum emission. And as Shklovsky pointed out in the 1950s, the distances to planetary nebulae could be estimated based on an assumed constant ionized mass, typically assumed to be $\sim$0.1 $M_{\odot}$ (see Osterbrock 1989). Moreover, because few PNs have any direct means for determining their distances, astronomers often rely on the Shklovsky method, and variants thereof, for the determination of distances, even though its assumptions appear to be incorrect. In this section we review the Shklovsky method and the ionized mass it implies.

2.2.1 *The Shklovsky Method*

The Shklovsky distance method relies on three major assumptions: First, that all PNs have essentially the same mass of gas. Second, that PN shells are fully ionized or "density bounded," which essentially means that the PN has run out of material to ionize. And third, that the ionized gas has a uniform density within the volume (not necessarily the entire volume of the nebula) where it is emitting. Under these assumptions, expansion of the nebula is reflected by a commensurate decrease in the density of emitting gas, so that the strength of the emission can be directly related to the physical size of the nebula.

The third assumption is often only implicitly stated in the use of a "filling factor" for a nebula, which expresses the fraction of the nebula that contains emitting gas. Since the filling factor proves to be critical to our analysis, we derive it for the more general case in which the density varies throughout the nebula.

The ionized mass can be derived from any of several sources of emission, but the simplest method is based on radio continuum emission at optically thin wavelengths, which avoids the problems of interstellar extinction. The thermal bremsstrahlung (free–free) radiation depends on the product of the electron density and the ion density (both $\propto n_i$) divided by the electron speed ($\propto \sqrt{T_e}$). Since the electron temperature can usually be assumed to be fairly constant throughout the ionized portions of the nebula, the mean value of the emission coefficient depends primarily on the density as

$$\langle j_\nu \rangle \propto \frac{\langle n_i^2 \rangle}{T_e^{1/2}} \,. \tag{2.1}$$

Therefore the integrated radio emission is a measure of the nebular density. And since the ionized mass of the nebula is proportional to the product of the ion density and the volume ($M_i \propto \langle n_i \rangle r_i^3$) we can write:

$$\langle j_\nu \rangle \propto \left[\frac{\langle n_i^2 \rangle}{\langle n_i \rangle^2} \right] \frac{M_i^2}{r^6 T_e^{1/2}} \,. \tag{2.2}$$

The term in brackets is a generalized form of the "filling factor" ϵ which is usually assumed to be of order unity or a value that can be estimated from the apparent geometry of a PN. The total flux density, S_ν, for an optically thin nebula at a distance d is then:

$$S_\nu \propto \frac{\langle j_\nu \rangle r^3}{d^2} \propto \frac{M_i^2}{\theta^3 d^5 \epsilon T_e^{1/2}} \tag{2.3}$$

where $\theta = r/d$ is the angular radius.

Our definition of the filling factor is more general than the common description that ϵ represents the fraction of the nebula containing emitting gas. The common description is correct (and ϵ reduces to this value) only if the gas has a uniform density wherever it is emitting and has zero density elsewhere. The emission is in fact strongly weighted toward the denser regions because of the n_i^2 dependence, but it is important to recognize that if some large fraction of the nebula contains low density gas, it may contribute significantly to $\langle n_i \rangle$ (and hence to the total mass) while making little difference in $\langle n_i^2 \rangle$.

Following Milne & Aller (1975), we can remove some minor terms that only weakly affect equation 2.3 by assuming typical He II and He III abundances and by letting $T_e \approx 10,000$ K in a logarithmic term. (Realistic deviations away from the mean values assumed have very little effect on the outcome.) Solving for the distance we then find:

$$d = 20.1 \text{ kpc} \left(\frac{M_i}{0.1 M_\odot}\right)^{2/5} \left(\frac{S_{5\text{GHz}}}{1 \text{ mJy}}\right)^{-1/5} \left(\frac{\theta}{1''}\right)^{-3/5} \left(\frac{\epsilon}{0.75}\right)^{-1/5} \left(\frac{T_e}{10,000 \text{ K}}\right)^{-1/10} \tag{2.4}$$

Note that the distance is weakly dependent on the mass, so that an error of a factor of two in the assumed ionized mass introduces an error of only ~30% in the distance. For the Shklovsky distance method the ionized mass is assumed to be constant, and since for practical purposes the filling factor and electron temperature are often assumed to be nearly constant as well, the distance in the

Shklovsky method is then determined by just two observables: flux density and angular size.

2.2.2 *The Ionized Mass of the PN Shell*

Inverting equation 2.4, we can derive the ionized mass in terms of the other quantities:

$$M_i = 5.54 \times 10^{-5} M_\odot \left(\frac{d}{1\ \mathrm{kpc}}\right)^{5/2} \left(\frac{S_{5\mathrm{GHz}}}{1\ \mathrm{mJy}}\right)^{1/2} \left(\frac{\theta}{1''}\right)^{3/2} \left(\frac{\epsilon}{0.75}\right)^{1/2} \left(\frac{T_e}{10,000\ \mathrm{K}}\right)^{1/4} \quad (2.5)$$

Note that the ionized mass determined from this equation is strongly dependent on the assumed distance and angular radius, but it is still only weakly dependent on the temperature. To determine the ionized mass we need a sample of PNs with independently determined, accurate distances, as well as accurate angular radii.

Based on his dissertation work, Gathier (1987) developed a sample of 30 PNs, each of which had distances determined using interstellar reddening, kinematic distances based on 21 cm absorption, or a combination of these methods with expansion distances (provided the combined distance measurements agreed with each other to within ~50%). The data for these PNs are summarized in Table 2.1. We have updated the data Gathier used and tabulated uncertainties for the various measurements, directly from their original sources where possible and otherwise estimated based on the nature of the data. Column (1) of Table 2.1 identifies the PNs by their common name, and column (2) gives the Galactic coordinate designation used in the *Strasbourg–ESO Catalog* (Acker et al. 1992). Columns (3) and (4) give the distances and their fractional uncertainties. We have adopted Gathier's distances and uncertainties, except for NGC 6572, which Masson (1989) finds is at a significantly larger distance based on a radio measurement of the angular expansion.

TABLE 2.1

PARAMETERS OF PNs WITH INDEPENDENT DISTANCE ESTIMATES

PN (1)	Designation (2)	d (kpc) (3)	$\frac{\Delta d}{d}$ (4)	T_e (10^4 K) (5)	$S_{5\mathrm{GHz}}$ (mJy) (6)	$\frac{\Delta S}{S}$ (7)	θ (arcsec) (8)	$\frac{\Delta\theta}{\theta}$ (9)	Source[a] (10)	M_{shk} ($M_\odot$) (11)	$\frac{\Delta M_{shk}}{M_{shk}}$ (12)	d_{shk} (kpc) (13)	$\frac{\Delta d_{shk}}{d_{shk}}$ (14)
NGC 6369	002.4 +05.8	2.0	0.35	1.25	1907	0.03	19.	0.2	O–CJA	1.2	0.86	0.56	0.32
NGC 6565	003.5 −04.6	0.9	0.44	1.04	39	0.21	6.	0.2	O–PK	0.0039	0.88	2.44	0.33
NGC 6537	010.1 +00.7	2.4	0.25	1.57	610	0.10	2.4	0.3	O–PM	0.051	0.99	2.44	0.35
NGC 6578	010.8 −01.8	2.0	0.4	1.02	148	0.23	4.3	0.2	O–PK	0.034	0.88	2.28	0.33
NGC 6567	011.7 −00.6	1.68	0.1	1.10	167	0.11	3.8	0.2	O–PK	0.020	0.87	2.40	0.32
NGC 6572	034.6 +11.8	1.7	0.47	1.03	1155	0.06	2.7	0.2	R–BD	0.032	0.86	2.00	0.32
NGC 7009	037.7 −34.5	0.58	0.43	0.98	702	0.05	10.7	0.2	O–CJA	0.013	0.86	0.97	0.32
NGC 6803	046.4 −04.1	3.0	0.33	0.96	89	0.18	2.8	0.3	O–PK	0.038	0.99	3.27	0.35
NGC 6886	060.1 −07.7	1.7	0.41	1.30	125	0.10	3.	0.3	O–PK	0.013	0.99	2.93	0.35
NGC 6720	063.1 +13.9	0.65	0.23	1.11	403	0.10	38.	0.1	O–CJA	0.091	0.78	0.50	0.31
Ps 1.....	065.0 −27.3	10.	0.1	1.31	5	0.50	1.	0.5	R–ZPB, JBT, GPG	0.042	1.35	10.8	0.44
NGC 6884	082.1 +07.0	1.8	0.39	1.03	171	0.08	3.1	0.3	O–PK, KM	0.017	0.99	2.70	0.35
NGC 7027	084.9 −03.4	1.1	0.27	1.24	6240	0.05	4.4	0.1	R–BD	0.054	0.78	1.06	0.31
NGC 7026	089.0 +00.3	2.18	0.32	0.91	254	0.05	6.3	0.3	O–CJA, Ba	0.096	0.99	1.63	0.35
NGC 7662	106.5 −17.6	0.98	0.36	1.28	620	0.03	7.6	0.2	R–TBB	0.029	0.86	1.22	0.32
NGC 7354	107.8 +02.3	1.5	0.33	1.22	586	0.04	11.5	0.1	O–CJA	0.15	0.78	0.96	0.31
NGC 246	118.8 −74.7	0.5	0.3	1.58	212	0.12	101.	0.1	R–ZPB	0.16	0.79	0.32	0.31
IC 1747.....	130.2 +01.3	2.5	0.4	1.01	110	0.07	5.2	0.2	O–CJA, Ba	0.068	0.86	2.16	0.32
NGC 1514	165.5 −15.2	0.5	0.3	1.40	239	0.20	68.	0.1	R–ZPB	0.092	0.79	0.40	0.31
NGC 2346	215.6 +03.6	0.8	0.25	1.36	77	0.16	17.	0.1	O–Ba	0.021	0.79	1.14	0.31

Continued, next page

TABLE 2.1 *(continued)*

PN (1)	Designation (2)	d (kpc) (3)	$\frac{\Delta d}{d}$ (4)	T_e (10^4 K) (5)	$S_{5\mathrm{GHz}}$ (mJy) (6)	$\frac{\Delta S}{S}$ (7)	θ (arcsec) (8)	$\frac{\Delta\theta}{\theta}$ (9)	Source[a] (10)	M_{shk} ($M_\odot$) (11)	$\frac{\Delta M_{shk}}{M_{shk}}$ (12)	d_{shk} (kpc) (13)	$\frac{\Delta d_{shk}}{d_{shk}}$ (14)
NGC 2440	234.8 +02.4	2.19	0.18	1.40	380	0.04	6.	0.4	R–ZPB	0.12	1.13	1.55	0.38
NGC 2452	243.3 −01.0	3.57	0.16	1.17	60	0.10	6.2	0.2	O–Ba	0.17	0.87	2.19	0.32
NGC 3242	261.0 +32.0	0.5	0.4	1.13	887	0.03	11.5	0.2	R–TBB	0.012	0.86	0.88	0.32
NGC 2792	265.7 +04.1	1.91	0.12	1.48	113	0.12	6.	0.2	O–PK	0.048	0.87	1.91	0.32
NGC 3132	272.1 +12.3	0.6	0.17	1.00	218	0.06	21.	0.1	O–JLMP	0.022	0.78	0.81	0.31
NGC 3211	286.3 −04.8	1.91	0.26	1.43	78	0.11	6.	0.3	O–PK	0.040	0.99	2.12	0.35
NGC 3918	294.6 +04.7	2.24	0.38	1.25	800	0.05	6.7	0.2	O–CHBW	0.22	0.86	1.25	0.32
NGC 5189	307.2 −03.4	1.73	0.31	1.27	356	0.11	16.	0.3	O–PR	0.28	0.99	0.87	0.35
NGC 5315	309.1 −04.3	2.62	0.39	0.92	478	0.05	2.5	0.3	O–PK	0.052	0.99	2.50	0.35
He 2–131	315.1 −13.0	0.6	0.33	1.02	325	0.12	2.9	0.3	O–PK	0.0014	0.99	2.47	0.35

[a]Sources of (O=optical, R=radio) angular radii: Ba (Balick 1987); BD (Basart & Daub 1987); CHBW (Clegg et al. 1987); CJA (Chu, Jacoby & Arendt 1987); GPG (Gathier, Pottasch, & Goss 1983); JBT (Johnson, Balick, & Thompson 1979); JLMP (Juguet et al. 1988); KM (Kohoutek & Martin 1981); PK (Perek & Kohoutek 1967); PM (Phillips & Mampaso 1988); PR (Phillips & Reay 1983); TBB (Terzian, Balick, & Bignell 1974); ZPB (Zijlstra, Pottasch, & Bignell 1989).

Column (5) gives the electron temperature as reported by Cahn, Kaler, & Stanghellini (1992). We estimate the temperature is typically uncertain by about 10%; but in any case the precise value of the temperature and its uncertainty proves unimportant here because of the weak dependence of either the distance or the mass on it.

The measured flux densities of the PNs at 5 GHz and their uncertainties are listed in columns (6) and (7) respectively. The values listed are averages (scaled when necessary to 5 GHz) based on the compilation of Higgs (1971), along with measurements by Milne & Aller (1975, 1982), Milne (1979), Zijlstra, Pottasch, & Bignell (1989), and the references quoted for radio measurements of the nebular size in column (10). The errors represent estimates of both the internal errors of these references and their disagreement with each other. A problematic case is Ps 1, which has a wide range of radio fluxes reported, probably because it is near the sensitivity limit of most of the measurements; we therefore make a best guess at the mean value and assign a large fractional error.

Columns (8) and (9) give the angular radii (actually the geometric mean of the radii along the major and minor axes) and our estimates of the fractional uncertainties in these sizes. Widely variant values of the angular radius are often used in the literature, but we attempt to present a consistent set of measurements here. We use the geometric mean of the radii in order to make a best guess at the emitting volume of the dense gas. If it were later determined that the dense region is better represented, for example, by an oblate spheroid, the major axis would probably be a better choice. Radio measurements are listed when available, but unfortunately few of these PNs have direct radio measurements of the angular sizes. Column (10) lists the type of measurement made (radio, R, or optical, O), and the source of the data used.

What is meant by "angular radius" is an important but subtle issue. Because the mean surface of a PN is constantly decreasing as the nebula ages, and because extinction affects the optical measurements in a distance-dependent way, the radius at a fixed surface brightness level will fail to identify any consistent region of nebula. In consequence, relative surface brightness levels are normally chosen at some fraction of the peak brightness—often 1/2 or 1/10 of the peak. (Examination of the radial surface brightness plots presented in § 3.2 may help to illustrate this point.) We find that at 1/2 of peak, not all of the dense region is always included, and this level is susceptible to problems of underestimating the size when there is significant smoothing due to seeing or telescope beam size (see Chapter 3). At 1/10 of peak, the measured radius sometimes extends beyond the dense shell into the low-density surrounding gas to various degrees, making it an unstable estimator of the volume of the dense region. We chose a level of $1/e$ (optically $\sim$1 mag) below the peak intensity because this level seems to be good at identifying the edge of the dense region without extending into the halo, and it is fairly stable against beam smoothing.

In practice, when contour plots or radial flux density plots were available, we determined the size at an isophotal level of $1/e$ of the peak intensity for centrally-brightened PNs, or of the mean of the two peaks in bipolar PNs, or of the mean around the brightened rim of shell PNs. We found good consistency between the radio and optical measurements at this level. Otherwise, we quote the optical size of the bright inner region, as is traditionally done, although this is potentially subject to large errors.

NGC 5189 is an example of how drastically the radius can affect estimates of the ionized mass. Gathier (1987) and other authors have usually assumed a radius of 70″, adopted from the larger values reported in the catalog of Perek & Kohoutek (1967); but we measure a $1/e$ mean radius of 16″ from the photometric

contours of Phillips & Reay (1983). Because of the $\theta^{1.5}$ dependence in equation 2.5, we therefore find a factor of ~10 smaller mass, which takes NGC 5189 from being the highest to near the average of all the ionized masses determined by Gathier. The 70 arcsec radius usually adopted probably represents a halo radius in this complexly structured PN. We suspected this even before uncovering the newer measurements because of discrepancies in the values cataloged by Perek & Kohoutek (1967). Unfortunately, many of the radii commonly adopted for PNs have only a single measurement—quite often passed down from the early part of this century—and there is little opportunity to identify these discrepancies. The poor state of affairs in the measurement of such a fundamental parameter for PNs is distressing, and clearly needs to be addressed in a much more systematic fashion. (Also see Chapter 3,)

Column (11) lists the ionized masses of the PNs derived from equation 2.5, assuming the filling factor $\epsilon = 0.75$ for all PNs as did Gathier (1987). We label this the "Shklovsky mass" (M_{shk}) as a reminder of the procedure used to derive it (use of a constant filling factor and the radius of the bright inner region), as well as to distinguish it from the total ionized mass that we can determine exactly for our PN simulations presented in § 2.3.

2.2.3 Statistical Analysis of the Derived Masses

Nominally, based on the data presented, the ionized masses range from about 10^{-3} to ~1 $M_{\odot}$, averaging to about 0.11 $M_{\odot}$. This certainly does not suggest that PNs have the substantial ionized masses we have argued must be present, and it appears to be strongly at odds with the Shklovsky method's assumption of a fixed mass. However, the statistical uncertainties in the measurements are substantial, making a more detailed statistical analysis necessary.

Column (12) gives the "fractional error" in the ionized mass based on the data used to derive it. A simple analysis of the propagation of errors gives the uncertainty in the mass as the quadratic sum of the errors in the individual quantities used to derive it. And as long as those individual uncertainties are small, they can be expanded relative to their mean values to give:

$$\frac{\Delta M_{shk}}{M_{shk}} = \sqrt{\left(\frac{5}{2}\frac{\Delta d}{d}\right)^2 + \left(\frac{3}{2}\frac{\Delta \theta}{\theta}\right)^2 + \left(\frac{1}{2}\frac{\Delta S}{S}\right)^2 + \left(\frac{1}{4}\frac{\Delta T_e}{T_e}\right)^2 + \left(\frac{1}{2}\frac{\Delta \epsilon}{\epsilon}\right)^2} \quad . \qquad (2.6)$$

The uncertainty in the filling factor was assumed to be 10%, but it should be noted that the filling factor may have a significantly greater uncertainty given the great uncertainty about the geometries of PN shells (see § 2.5.1).

The fractional errors we derive for M_i in Column (12) are obviously very large—typically ~100%. The reason for this is the dependence of the estimated mass on high powers of quantities that are themselves fairly uncertain. Equation 2.6 is only accurate when the errors are small, which is clearly untrue here. A 100% error is more appropriately understood as a factor of ~2 error. The best description of the error is in terms of the logarithmic value of the mass since the error is based on the product of other uncertain measurements. In this case, the error in $\log M_i$ equals 0.434 times the error quoted in column (12). Using the errors in this way, we find a weighted mean of the logarithms of the masses corresponding to $0.047 M_\odot$.

Given such large errors in the masses, it is no longer obvious whether the range of masses in Column (11) represents real or statistical variations relative to the mean. To test this, we use a simple χ^2 analysis of the logarithms of the masses relative to the mean value to determine whether the variations are larger than would be expected for the propagated errors. Relative to the mean mass of $0.047 M_\odot$, we find a reduced-χ^2 value of 2.28 for the 30 PNs. A reduced-χ^2 value of ≈ 1.0 would imply that all of the differences are due to the errors in the

measurements; a value of $\sim$2 implies that the variation in masses is produced about equally by intrinsic variations and by measurement errors.

To explain the entire range of masses seen (assuming that our propagated error estimates are accurate), our χ^2 analysis indicates that the intrinsic variability of $\log M_i$ must be 0.42 (1σ). This corresponds to a range of a factor of 2.6 larger or smaller than the mean mass. This appears large, but if one is calculating distances, it would cause less than 50% errors in the estimated distances.

A better way of testing the effect of mass variability on distance estimates is to directly calculate the Shklovsky distances for the PNs in Table 2.1. We apply the Shklovsky method in its simplest form, with constant temperature, $T_e = 10,000$ K, and constant filling factor, $\epsilon = 0.75$, and assume a fixed ionized mass of 0.047 $M_\odot$. The derived distances are listed in column (13) of Table 2.1. Despite the wide range of ionized masses listed, the Shklovsky distances only disagree by more than a factor of two in 4 of the 30 cases. In fact, given the uncertainties in Gathier's distances, and the errors in S_ν and θ, a χ^2 analysis shows that the Shklovsky distances are consistent with the independent distances if there is only a 28% (1σ) uncertainty in the constant of proportionality in equation 2.4—in other words, in the value of $M_i^{0.4}$ (ignoring possible variations in ϵ or T_e). Relative uncertainties of the Shklovsky distance are listed in column (13) based on a 30% intrinsic standard deviation, along with the errors propagated from the uncertainties in S_ν and θ. We remark that even though (or perhaps because) we have ignored possible differences in the filling factor and the temperature, the Shklovsky distances have fractional errors that are not substantially worse than those of the independently determined distances.

Thus, to within the errors the Shklovsky method does in fact work quite well when tested on a sample of relatively nearby PNs. We are not, however, advocating the adoption of equation 2.4 with the ionized mass found here because

we believe an even more accurate formulation can be developed which accounts for much of the variation of ionized mass with the growth of the nebula. We describe this new distance method in Chapter 3.

2.3 Simulated Planetary Nebulae

To address the questions of why so little ionized mass appears to be present and why the Shklovsky method works so well, we have employed a computer simulation based on a simple spherically-symmetric, momentum-conserving two wind model. By simulating the evolution of nebulae we hope to understand what the estimated ionized masses would be if these model nebulae were actually observed.

The simulation we use is clearly too simple to examine detailed questions about PN geometry or morphology. But it is not our objective to do that here. We are for the most attempting to simulate the PN's evolution with respect to just three basic parameters, two of which are directly observable: the PN's total radio emission and radius (which determine surface brightness and angular size) and its ionized mass (which is estimated from the former two). While other more sophisticated energy conserving models in 2- or 3-dimensions may better explain the detailed structure of the PNs, the gross properties we are interested in are primarily determined by the amount of material in the remnant AGB wind which is swept up and confined to a dense shell as well as the amount of ionizing radiation coming from the central star. The amount of material confined to the dense shell is in turn determined by the speed at which the shell propagates into the remnant AGB envelope due to the momentum of a fast-wind from the central star of the PN. Our model yields shell speeds and densities which are consistent with both the more sophisticated models and with observed expansion velocities

and shell sizes; therefore we expect our simple model to yield reasonable estimates of PNs' basic properties.

To help establish its validity, we also compare results from our simulations to density profiles from a more sophisticated energy-conserving model. The radial density and intensity profiles of our simple model proves to be quite similar to those of the more complex model, and it is these radial profiles which are most important in the determination of apparent radii, emission, and ionized masses. Moreover, the two-wind model is simple enough that we can readily explore the effects of changing various of its input parameters to search for *relative* effects when the nebular parameters are allowed to vary over a wide range, and it has few enough free parameters that it is unlikely for our results to hide some sort of fine-tuning within the model.

2.3.1 Density profiles

The dynamical evolution of planetary nebulae is modeled using the relatively simple two-wind, momentum-conserving model of Kwok et al. (1978; Kwok 1982, 1985). In this model the bulk of the mass loss from the progenitor star occurs as a wind during the AGB stage. After the hot core ($M_{\rm PNN} \approx 0.6 M_{\odot}$) of the star is exposed, the AGB wind ceases and a fast wind commences, with much higher velocities but about two orders of magnitude lower in its rate of mass loss. Due to the small collisional mean free path of the wind particles when they interact, the effect of the fast wind is to bunch-up or "snowplow" the inside edge of the remnant AGB wind into a high density shell.

Where they do not interact, the mass distributions of the remnant AGB wind and the fast wind follow an inverse square law for the assumed constant mass loss. The density profile is given by $\rho_{\rm AGB}(r) = \dot{M}_{\rm AGB}/4\pi r^2 V_{\rm AGB}$ for the AGB wind and

likewise $\rho_{\rm fast}(r) = \dot{m}_{\rm fast}/4\pi r^2 v_{\rm fast}$ for the fast wind. Where the fast wind impinges on the AGB wind a shell of swept-up material forms the dense shell.

We choose a fairly "typical" set of values for the two winds. The velocity for the AGB wind is $V_{\rm AGB} = 10$ km s^{-1} for most of our simulations. Bryce, Meaburn, & Walsh (1993) measured the expansion velocities of the giant halos of two PNs, which should mirror the velocity of the original AGB wind that formed the halo. They find a velocity of 7 km s^{-1} for NGC 6543 and 13 km s^{-1} for NGC 6826 using the assumption that the halo is an extended structure rather than a thin shell. We also assume a mass loss rate that might be found in the later stages before ionization of the nebula begins: $\dot{M}_{\rm AGB}$ of $\sim 10^{-5}$ M$_\odot$ yr^{-1}. There is almost certainly an evolution from a much lower mass loss rate at early stages up to this mass loss rate (which is sometimes called a "superwind"; Frank, Balick, & Riley 1990). Choosing a higher mass loss rate could be problematic if one was trying to model the later stages of PN evolution when the shell would be incorporating earlier wind material. However, since the radio emission we will be examining here is dominantly produced in the inner ionized region, and the nebula drops to uncharacteristically low surface brightnesses in its later stages, the "superwind" values are probably the better choice for our purposes.

The fast wind is also somewhat uncertain and presumably variable, but we set it to have a speed $v_{\rm fast}$ of a few thousand km s^{-1} and $\dot{m}_{\rm fast}$ of $\sim 10^{-7} M_\odot\, yr^{-}1$. Cerruti-Sola & Perinotto (1989) estimate somewhat smaller mass-loss rates on average, but the amount of momentum we use is necessary relative to our choice of AGB-wind parameters in order for the fast wind to accelerate the shell to the range of expansion speeds (of order a few tens of km s^{-1}) typically seen in PNs (Weinberger 1989). We can only increase or decrease the mass loss rates of both the AGB and fast winds in unison if we want to retrieve similar shell expansion speeds. We also use some fairly high values for the mass loss rates in several of our

models primarily to illustrate some of the interesting behavior when the central star cannot ionize the whole nebula.

Kwok *et al.* (1978) show that the two wind model produces a shell that propagates outward through the remnant AGB wind with a nearly constant terminal velocity. This depends on the mass loss rates and velocities of the two winds as:

$$V_{\rm shell} \approx \frac{(\dot{M}_{\rm AGB} - \dot{m}_{\rm fast}) + (v_{\rm fast} - V_{\rm shell})\sqrt{\frac{\dot{m}_{\rm fast}\dot{M}_{\rm AGB}}{v_{\rm fast}V_{\rm AGB}}}}{\left[\frac{\dot{M}_{\rm AGB}}{V_{\rm AGB}} - \frac{\dot{m}_{\rm fast}}{v_{\rm fast}}\right]} \ . \tag{2.7}$$

The mean radius of the shell at any time (t) after the fast wind commences is $r_{shell} \approx V_{shell}t$, and the mass of the shell is then given by:

$$M_{shell}(t) \approx \left[\frac{\dot{M}_{\rm AGB}}{V_{\rm AGB}} - \frac{\dot{m}_{\rm fast}}{v_{\rm fast}}\right] r_{shell}(t) - \dot{M}_{\rm AGB}t + \dot{m}_{\rm fast}t \ . \tag{2.8}$$

In more sophisticated energy-conserving models, it is thought that the mechanism for the expansion of this shell is the thermal pressure of a hot shocked bubble of gas inside the shell where the fast wind is colliding with the AGB wind (Volk & Kwok 1985). For our purposes, this has a secondary effect, primarily on the thickness of the dense shell region, since momentum-conservation is still required. The shell velocities we obtain from our model are of the same order as observed PN expansion velocities (Weinberger 1989), and it is the rate at which material is swept up by this shell, coupled with the evolution of the central star that determines the gross observable properties of the PN.

To further check the validity of our model we compare it to density profiles from the two–wind energy conserving hydrodynamic models of Schmidt-Voigt & Köppen (1987). The density profiles are illustrated in Figure 2.1 where our simple model is compared to the more sophisticated model with the same wind parameters and at the same time steps. The two-wind model displays less structure within the shell, but otherwise it is qualitatively and quantitatively similar to the hydrodynamic model.

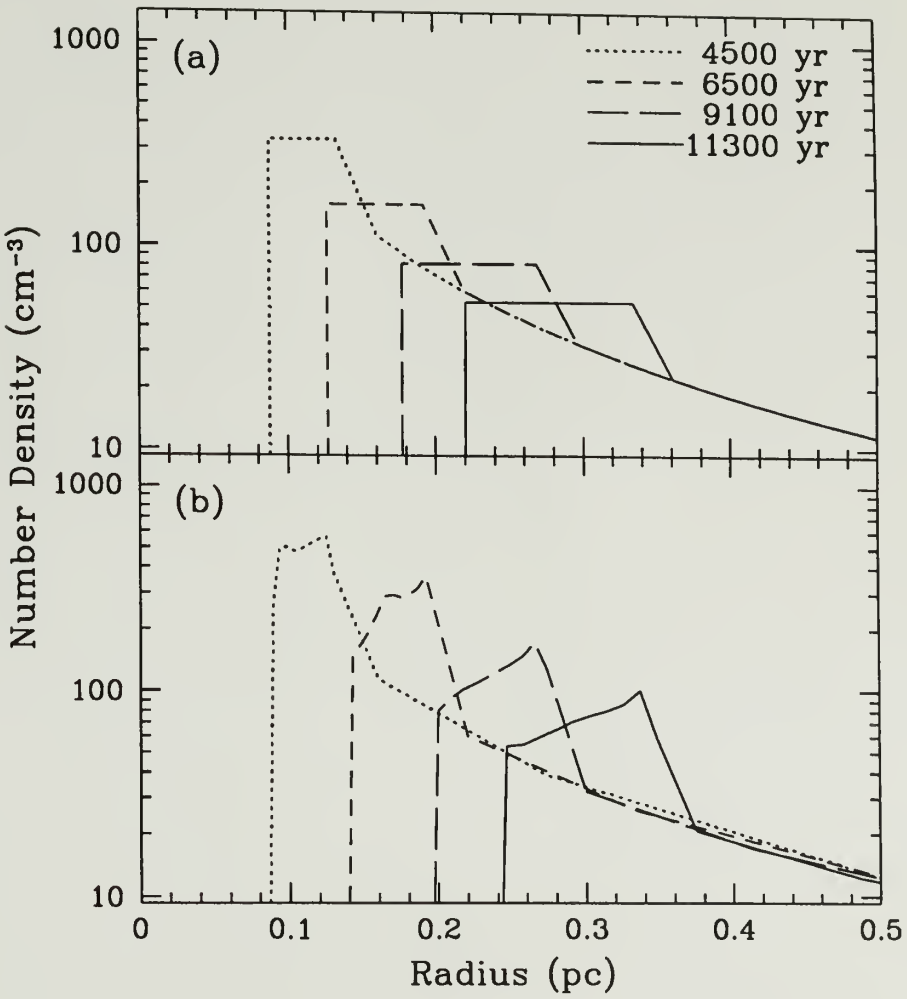

Figure 2.1. *(a)* Number density profile of the thick snow-plowed shell using the simple momentum conserving model. *(b)* Number density profile with the same input wind parameters for the 2-wind energy conserving model of Schmidt-Voigt & Köppen (1987).

We note, however, that the initial stages of shell formation are not well-defined in the two-wind model, nor are the late stages. This is both because the two-wind model assumes equilibrium conditions based on fixed parameters for the winds, and because the way the fast wind actually turns on and then evolves is not fully understood. We therefore restrict our simulations to PNs with ages between 3,000 and 12,000 yr. This is not a very limiting assumption, however, since the majority of PNs are likely to be in this range so that they will be both nonstellar and of high enough surface brightness to be easily detectable.

2.3.2 Ionization

For the calculation of ionized mass and radius of the PN, we can assume a steady state for each phase in the evolution of the central star since the time scales for ionization and recombination are short compared to both the dynamical time scale of the nebula and the temporal variability of the central star (Dopita & Metheringham 1990). In essence, we calculate the size of a Strömgren sphere for H II, He II and He III. Although recombinations for He III and He II can ionize H I, the radii of the H II, He II and He III regions can be approximately calculated by decoupling the ionization of the three main species (see Osterbrock, 1974, §2.4). If we denote the rate of ionizing photons (photons/sec) for ionization of H I as $Q_1(h_\nu > 13.6eV; \lambda < 912\AA)$, for He I as $Q_2(h_\nu > 24.6eV; \lambda < 504\AA)$, and for He II as $Q_3(h_\nu > 54.4eV; \lambda < 228\AA)$, we can approximate the ionization equilibrium equations by:

$$Q_1 \approx 4\pi\alpha_B(H\,I) \int_{r_{pnn}}^{R_s(H\,II)} n_e(r) n_{H\,II}(r) r^2 dr$$

$$Q_2 \approx 4\pi\alpha_B(He\,I) \int_{r_{pnn}}^{R_s(He\,II)} n_e(r) n_{He\,II}(r) r^2 dr \qquad (2.9)$$

$$Q_3 \approx 4\pi\alpha_B(He\,II) \int_{r_{pnn}}^{R_s(He\,III)} n_e(r) n_{He\,III}(r) r^2 dr$$

where the α_B's are the recombination coefficients in $cm^3 s^{-1}$, [$\alpha_B(H\,I) = 2.6 \times 10^{-13}$, $\alpha_B(He\,I) = 2.7 \times 10^{-13}$, $\alpha_B(He\,II) = 1.5 \times 10^{-12}$, for $T_e \approx 10^4 K$] and the n's are number densities in cm^{-3}.

We derive the flux of ionizing photons (the Q's in the above equations) from the temperature and luminosity of the central star assuming it is a perfect blackbody. The runs of temperature and luminosity of the PNN as a function of time were obtained from the model evolutionary tracks by Schönberner (1989) for PNN's of 0.565, 0.598, and 0.644 $M_\odot$. Although this may seem a minor difference in mass, it spans the range of most observed PNNs and the small mass difference yields significantly different evolutionary time scales, with the more massive PNN evolving much more rapidly. The approximate ionized PN radius and mass are thus obtained by integrating numerically from the PN's central star out to the Strömgren radius.

2.3.3 Radio Continuum Emission

The radio continuum emission for frequencies where planetary nebulae are generally optically thin ($\nu > 2GHz$) is obtained by integrating numerically along lines of sight at a series of impact parameters (p) from the center of the nebula. The emission coefficient (j_ν) for thermal bremsstrahlung (free-free) radiation in an ionized region is given by Milne & Aller (1975):

$$j_\nu = \frac{3.75 \times 10^{-38}}{4\pi\sqrt{T_e}} n_e \left[(n_{H\,II} + n_{He\,II}) \ln\left(\frac{4.95\times10^{-2}T_e^{3/2}}{\nu}\right) + 4n_{He\,III} \ln\left(\frac{2.47\times10^{-2}T_e^{3/2}}{\nu}\right)\right] \qquad (2.10)$$

in cgs units. The intensity (I_ν) for an optically thin emitting cloud is just the emission coefficient integrated along the line of sight (s) within the cloud

($I_\nu = \int j_\nu ds$). The expression for I_ν is then just:

$$I_\nu = \int K n_e [A(n_{H\,II} + n_{He\,II}) + B n_{He\,III}]\, ds \tag{2.11}$$

or

$$I_\nu = K \left(A \int n_e n_{H\,II}\, ds + A \int n_e n_{He\,II}\, ds + B \int n_e n_{He\,III}\, ds \right) \tag{2.12}$$

in (erg cm^{-2} s^{-1} Hz^{-1} ster^{-1}) where $K = 3.75 \times 10^{-38}/(4\pi\sqrt{T_e})$,
$A = \ln(4.95 \times 10^{-2} T_e^{3/2}/\nu)$, and $B = \ln(2.47 \times 10^{-2} T_e^{3/2}/\nu)$. The integration is done numerically for a number of impact parameters (p) from the center of the PN ($p = 0$) out to the Strömgren radius of the H II region ($p = R_s$).

The flux density for a PN at a distance from the observer of 1 kpc is computed from the intensity profile. The flux density is given by:

$$S_\nu = \int I_\nu d\Omega = 2\pi \int I_\nu \theta d\theta \tag{2.13}$$

$$S_\nu = \frac{2\pi}{d^2} \int_0^{R_s} I_\nu(p) p dp \tag{2.14}$$

and is evaluated numerically for all impact parameters.

As a further check on the two-wind model, we compare it again to the hydrodynamic model of Schmidt-Voigt & Köppen (1987), but now to examine the intensity profiles that would be observed from both models (Figure 2.2). Here also the models agree well, both in terms of the shape of the intensity profile, the $1/e$ radius (0.13, 0.21, 0.27, and 0.35 pc versus 0.14, 0.20, 0.27, and 0.32 pc at the four time steps in the hydro and simple models respectively), and the "Shklovsky mass" (0.10, 0.27, 0.27, and 0.30 $M_\odot$ versus 0.11, 0.18, 0.24, and 0.25 $M_\odot$). From the basic agreement, we conclude that the simple two-wind momentum-conserving model is an adequate approximation for our purposes.

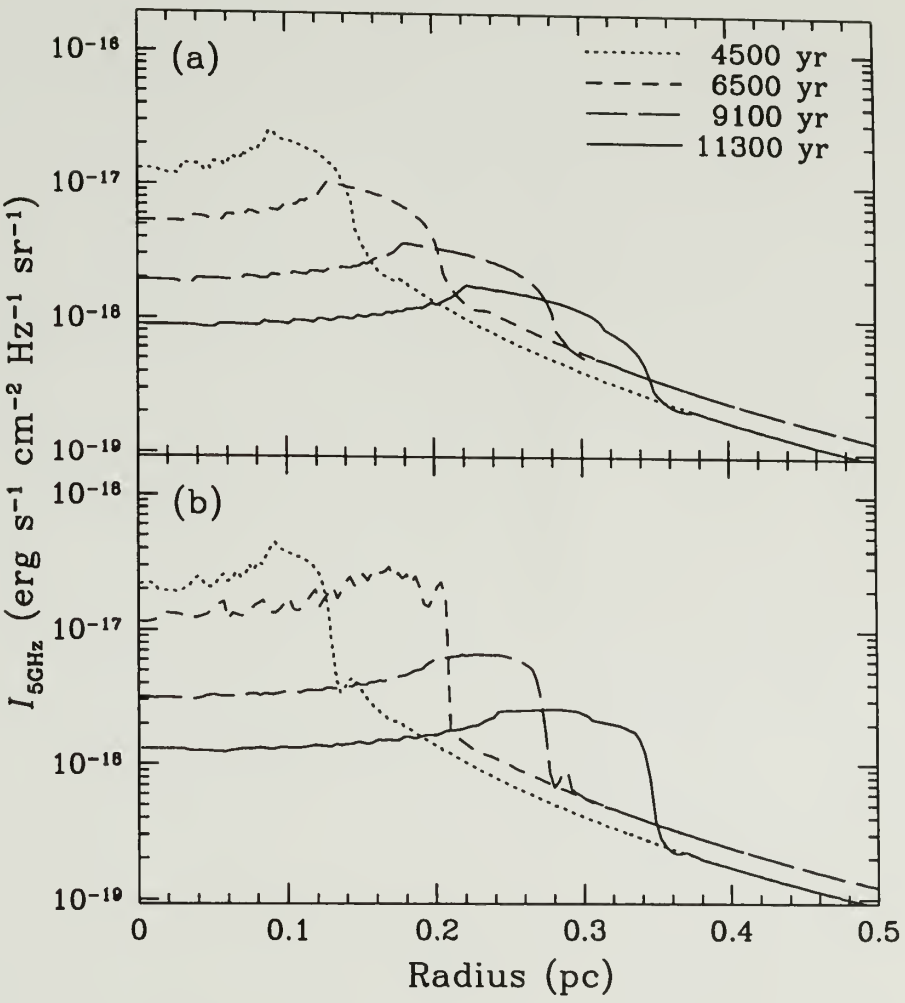

Figure 2.2. *(a)* Radio continuum intensity profile at 5 GHz for the simple momentum conserving model. *(b)* Intensity profile with the same input wind parameters for the 2-wind energy conserving model of Schmidt-Voigt & Köppen (1987).

2.3.4 *Simulation Parameters*

The properties of the simulated PNs were explored by varying each of the simulation parameters over a wide range, and determining the effects on observable properties, in particular, the Shklovsky mass. For most of our simulations we use a 0.598 $M_{\odot}$ PNN, which is near the peak of the PNN mass distribution. We also examined the effects on our models of both a low-mass ($0.565 M_{\odot}$) and high-mass ($0.644 M_{\odot}$) central star. According to the initial/final mass relation of Weidemann (1987; see also §1), we might expect a higher envelope mass for a high-mass PNN, and a smaller envelope mass for the low-mass PNN.

The input parameters used are given in Table 2.2. Column (1) lists the model number. Column (2) gives the mass of the central star, column (3) the mass of the envelope, and column (4) the fraction of helium assumed. Columns (5) and (6) list the velocity and mass loss rate chosen for the AGB wind, and columns (7) and (8) the corresponding values for the fast wind. Columns (9) and (10) give the shell velocity and fractional thickness of the shell derived for each simulation. The fractional thickness we list is the thickness of the shell relative to its outer radius; thus the "filling factor" as it is usually calculated from the geometry of the nebula would be $\epsilon = 1 - (1 - \Delta R/R)^3$.

The results of our simulations at 3000 yr time steps are listed in Table 2.3. A brief description of each model, comparing it to Model 1, is given on a single line followed by four lines showing the resultant parameters for the model PN at the times after termination of the AGB wind listed in column (1). Columns (2), (3), and (4) list, respectively, the radii of the ionization front, the outer edge of the dense shell, and the $1/e$ radio isophote (which we call the "Shklovsky radius").

TABLE 2.2
PARAMETERS OF PN SIMULATIONS

Model (1)	M_{PNN} ($M_\odot$) (2)	M_{env} ($M_\odot$) (3)	$\frac{n_{He}}{n_H}$ (4)	V_{AGB} (kms^{-1}) (5)	$\dot{M}_{AGB}$ ($M_\odot yr^{-1}$) (6)	v_{fast} (kms^{-1}) (7)	$\dot{m}_{fast}$ ($M_\odot yr^{-1}$) (8)	V_{sh} (kms^{-1}) (9)	$\frac{\Delta R_{sh}}{R_{sh}}$ (10)
1	0.598	2.4	0.11	10.	1.0×10^{-5}	2000.	1.0×10^{-7}	24.0	0.29
2	0.598	2.4	0.11	10.	3.0×10^{-6}	2000.	3.0×10^{-8}	24.0	0.29
3	0.598	2.4	0.11	10.	3.0×10^{-5}	2000.	3.0×10^{-7}	24.0	0.29
4	0.644	2.4	0.11	10.	1.0×10^{-5}	2000.	1.0×10^{-7}	24.0	0.29
5	0.565	2.4	0.11	10.	1.0×10^{-5}	2000.	1.0×10^{-7}	24.0	0.29
6	0.644	2.4	0.11	10.	3.0×10^{-5}	2000.	3.0×10^{-7}	24.0	0.29
7	0.565	2.4	0.11	10.	3.0×10^{-5}	2000.	3.0×10^{-7}	24.0	0.29
8	0.598	1.0	0.11	10.	1.0×10^{-5}	2000.	1.0×10^{-7}	24.0	0.29
9	0.598	10.0	0.11	10.	1.0×10^{-5}	2000.	1.0×10^{-7}	24.0	0.29
10	0.565	1.0	0.11	10.	1.0×10^{-5}	2000.	1.0×10^{-7}	24.0	0.29
11	0.598	2.4	0.03	10.	1.0×10^{-5}	2000.	1.0×10^{-7}	24.0	0.29
12	0.598	2.4	0.30	10.	1.0×10^{-5}	2000.	1.0×10^{-7}	24.0	0.29
13	0.598	2.4	0.11	10.	3.0×10^{-6}	2000.	1.0×10^{-7}	35.4	0.13
14	0.598	2.4	0.11	10.	3.0×10^{-5}	2000.	1.0×10^{-7}	18.1	0.49
15	0.598	2.4	0.11	10.	1.0×10^{-4}	2000.	1.0×10^{-7}	14.4	0.68
16	0.598	2.4	0.11	3.	1.0×10^{-5}	2000.	1.0×10^{-7}	10.7	0.63
17	0.598	2.4	0.11	30.	1.0×10^{-5}	2000.	1.0×10^{-7}	53.8	0.10
18	0.598	2.4	0.11	10.	1.0×10^{-5}	2000.	3.0×10^{-8}	17.7	0.50
19	0.598	2.4	0.11	10.	1.0×10^{-5}	2000.	3.0×10^{-7}	34.1	0.15
20	0.598	2.4	0.11	10.	1.0×10^{-5}	600.	1.0×10^{-7}	17.5	0.51
21	0.598	2.4	0.11	10.	1.0×10^{-5}	6000.	1.0×10^{-7}	34.3	0.14
22	0.598	2.4	0.11	10.	1.0×10^{-5}				

TABLE 2.3
PLANETARY NEBULA SIMULATIONS

t (yr) (1)	R_i (pc) (2)	R_{sh} (pc) (3)	R_{shk} (pc) (4)	M_i ($M_\odot$) (5)	M_{sh} ($M_\odot$) (6)	M_{shk} ($M_\odot$) (7)	$S_{5\mathrm{GHz}}$ (mJy) (8)	$\frac{S(shell)}{S(total)}$ (9)
Model 1: Standard Model								
3000	2.48	0.09	0.09	2.39	0.042	0.056	142.	0.627
6000	2.51	0.18	0.18	2.37	0.084	0.128	96.	0.634
9000	2.54	0.27	0.26	2.36	0.127	0.189	62.	0.641
12000	2.57	0.36	0.34	2.34	0.169	0.219	38.	0.698
Model 2: $0.3 \times \dot{M}_{AGB}$ and $0.3 \times \dot{m}_{fast}$								
3000	8.20	0.09	0.09	2.40	0.013	0.017	13.	0.634
6000	8.23	0.18	0.18	2.39	0.025	0.040	9.	0.634
9000	8.27	0.27	0.27	2.39	0.038	0.059	6.	0.617
12000	8.30	0.36	0.35	2.38	0.051	0.078	4.	0.626
Model 3: $3 \times \dot{M}_{AGB}$ and $3 \times \dot{m}_{fast}$								
3000	0.85	0.09	0.09	1.67	0.127	0.149	1089.	0.676
6000	0.88	0.18	0.17	2.31	0.253	0.318	630.	0.704
9000	0.91	0.27	0.26	2.27	0.380	0.537	503.	0.708
12000	0.33	0.36	0.31	0.34	0.507	0.325	112.	1.000
Model 4: $M_{PNN} = 0.644 M_\odot$								
3000	2.48	0.09	0.09	2.39	0.042	0.066	197.	0.627
6000	2.51	0.18	0.17	2.37	0.084	0.112	78.	0.676
9000	2.54	0.27	0.26	2.36	0.127	0.166	51.	0.684
12000	2.57	0.36	0.34	2.34	0.169	0.218	37.	0.690
Model 5: $M_{PNN} = 0.565 M_\odot$								
3000	2.48	0.09	0.09	1.66	0.042	0.050	118.	0.637
6000	2.51	0.18	0.18	2.37	0.084	0.109	69.	0.634
9000	2.54	0.27	0.26	2.36	0.127	0.161	46.	0.653
12000	2.57	0.36	0.35	2.34	0.169	0.250	46.	0.652

Continued, next page

TABLE 2.3 *(continued)*

t (yr) (1)	R_i (pc) (2)	R_{sh} (pc) (3)	R_{shk} (pc) (4)	M_i ($M_\odot$) (5)	M_{sh} ($M_\odot$) (6)	M_{shk} ($M_\odot$) (7)	$S_{5\mathrm{GHz}}$ (mJy) (8)	$\frac{S(shell)}{S(total)}$ (9)
Model 6: $M_{PNN} = 0.644 M_\odot$, $3 \times \dot{M}_{AGB}$, and $3 \times \dot{m}_{fast}$								
3000	0.85	0.09	0.09	2.36	0.127	0.166	1385.	0.686
6000	0.15	0.18	0.14	0.09	0.253	0.104	125.	1.000
9000	0.22	0.27	0.22	0.17	0.380	0.177	99.	1.000
12000	0.30	0.36	0.29	0.23	0.507	0.241	76.	1.000
Model 7: $M_{PNN} = 0.565 M_\odot$, $3 \times \dot{M}_{AGB}$, and $3 \times \dot{m}_{fast}$								
3000	0.08	0.09	0.08	0.06	0.127	0.067	316.	1.000
6000	0.88	0.18	0.18	2.31	0.253	0.312	572.	0.674
9000	0.91	0.27	0.26	2.27	0.380	0.455	363.	0.709
12000	0.94	0.36	0.35	2.23	0.507	0.597	275.	0.758
Model 8: $M_{env} = 1.0 M_\odot$								
3000	1.05	0.09	0.09	0.99	0.042	0.054	136.	0.633
6000	1.08	0.18	0.18	0.97	0.084	0.124	90.	0.660
9000	1.11	0.27	0.26	0.96	0.127	0.182	58.	0.688
12000	1.14	0.36	0.34	0.94	0.169	0.210	35.	0.756
Model 9: $M_{env} = 10 M_\odot$								
3000	10.25	0.09	0.09	9.99	0.042	0.062	158.	0.665
6000	10.28	0.18	0.18	9.97	0.084	0.137	103.	0.610
9000	10.31	0.27	0.27	9.96	0.127	0.199	67.	0.628
12000	10.34	0.36	0.35	9.94	0.169	0.229	40.	0.663
Model 10: $M_{PNN} = 0.565 M_\odot$ and $M_{env} = 1.0 M_\odot$								
3000	1.05	0.09	0.09	0.69	0.042	0.049	114.	0.643
6000	1.08	0.18	0.18	0.97	0.084	0.105	65.	0.660
9000	1.11	0.27	0.26	0.96	0.127	0.154	43.	0.698
12000	1.14	0.36	0.35	0.94	0.169	0.237	42.	0.715
Model 11: $n_{\mathrm{He}}/n_{\mathrm{H}} = 0.03$								
3000	2.48	0.09	0.09	2.39	0.042	0.066	202.	0.627
6000	2.51	0.18	0.18	2.37	0.084	0.137	109.	0.634
9000	2.54	0.27	0.26	2.36	0.127	0.202	71.	0.641
12000	2.57	0.36	0.35	2.34	0.169	0.266	52.	0.652

Continued, next page

TABLE 2.3 *(continued)*

t (yr) (1)	R_i (pc) (2)	R_{sh} (pc) (3)	R_{shk} (pc) (4)	M_i ($M_\odot$) (5)	M_{sh} ($M_\odot$) (6)	M_{shk} ($M_\odot$) (7)	$S_{5\mathrm{GHz}}$ (mJy) (8)	$\frac{S(shell)}{S(total)}$ (9)
Model 12: $n_{\mathrm{He}}/n_{\mathrm{H}} = 0.30$								
3000	2.48	0.09	0.09	2.39	0.042	0.043	83.	0.627
6000	2.51	0.18	0.18	2.37	0.084	0.118	81.	0.634
9000	2.54	0.27	0.26	2.36	0.127	0.174	53.	0.641
12000	2.57	0.36	0.33	2.34	0.169	0.165	24.	0.723
Model 13: $0.3 \times \dot{M}_{AGB}$								
3000	8.20	0.12	0.12	2.40	0.023	0.038	27.	0.796
6000	8.23	0.23	0.23	2.40	0.046	0.082	17.	0.823
9000	8.27	0.35	0.35	2.40	0.069	0.121	11.	0.831
12000	8.30	0.47	0.46	2.40	0.092	0.160	8.	0.838
Model 14: $3 \times \dot{M}_{AGB}$								
3000	0.85	0.08	0.10	1.72	0.073	0.153	779.	0.445
6000	0.88	0.16	0.19	2.25	0.146	0.297	441.	0.515
9000	0.91	0.25	0.30	2.17	0.219	0.516	329.	0.492
12000	0.48	0.33	0.36	0.75	0.292	0.399	112.	0.744
Model 15: $10 \times \dot{M}_{AGB}$								
3000	0.12	0.09	0.11	0.34	0.133	0.277	1808.	0.669
6000	0.31	0.18	0.24	1.47	0.267	0.853	1651.	0.537
9000	0.34	0.28	0.32	1.00	0.400	0.898	783.	0.715
12000	0.36	0.37	0.32	0.51	0.534	0.346	112.	1.000
Model 16: $0.3 \times V_{AGB}$								
3000	0.74	0.06	0.06	1.63	0.077	0.102	1408.	0.529
6000	0.75	0.12	0.12	2.22	0.155	0.212	813.	0.554
9000	0.76	0.18	0.19	2.13	0.232	0.389	660.	0.551
12000	0.22	0.24	0.20	0.25	0.309	0.169	112.	1.000
Model 17: $3 \times V_{AGB}$								
3000	7.45	0.17	0.18	2.40	0.024	0.048	14.	0.735
6000	7.54	0.35	0.35	2.40	0.048	0.106	9.	0.750
9000	7.63	0.52	0.52	2.40	0.072	0.157	6.	0.751
12000	7.72	0.70	0.69	2.39	0.097	0.207	4.	0.762

Continued, next page

TABLE 2.3 *(continued)*

t (yr) (1)	R_i (pc) (2)	R_{sh} (pc) (3)	R_{shk} (pc) (4)	M_i ($M_\odot$) (5)	M_{sh} ($M_\odot$) (6)	M_{shk} ($M_\odot$) (7)	$S_{5\mathrm{GHz}}$ (mJy) (8)	$\frac{S(shell)}{S(total)}$ (9)
Model 18: $0.3 \times \dot{m}_{fast}$								
3000	2.48	0.08	0.10	2.37	0.023	0.056	94.	0.386
6000	2.51	0.16	0.20	2.35	0.046	0.130	64.	0.395
9000	2.54	0.25	0.31	2.32	0.069	0.193	41.	0.410
12000	2.57	0.33	0.40	2.29	0.092	0.234	27.	0.462
Model 19: $3 \times \dot{m}_{fast}$								
3000	2.48	0.11	0.11	2.40	0.073	0.105	247.	0.835
6000	2.51	0.23	0.22	2.39	0.146	0.240	165.	0.833
9000	2.54	0.34	0.34	2.38	0.219	0.358	108.	0.845
12000	2.57	0.45	0.44	2.37	0.292	0.413	62.	0.865
Model 20: $0.3 \times v_{fast}$								
3000	2.48	0.08	0.10	2.37	0.023	0.057	93.	0.378
6000	2.51	0.16	0.21	2.34	0.046	0.132	63.	0.387
9000	2.54	0.25	0.31	2.32	0.069	0.195	41.	0.403
12000	2.57	0.33	0.41	2.29	0.091	0.238	27.	0.456
Model 21: $3 \times v_{fast}$								
3000	2.48	0.11	0.11	2.40	0.073	0.107	249.	0.835
6000	2.51	0.23	0.23	2.39	0.147	0.244	166.	0.840
9000	2.54	0.34	0.34	2.38	0.220	0.362	108.	0.846
12000	2.57	0.46	0.45	2.37	0.293	0.418	63.	0.866
Model 22: No fast wind								
3000	2.48	0.03	0.04	2.40		0.023	205.	
6000	2.51	0.06	0.09	2.40		0.055	139.	
9000	2.55	0.09	0.13	2.40		0.079	92.	
12000	2.58	0.12	0.16	2.40		0.085	54.	

Columns (5), (6), and (7) likewise list the total ionized mass, the mass of the dense shell respectively, and the derived Shklovsky mass. Column (8) gives the total integrated flux density (mJy) that would be observed if the model nebulae were at a distance of 1 kpc. Finally, column (9) lists the fractional contribution of the dense shell to the total radio continuum flux.

We comment finally that the absolute scaling in these various models is not our primary focus. For example, the masses we derive appear to be higher on average than we estimated from the observations in §2.2.3. We suspect this may be attributed at least in part to the oversimplified spherical geometry we use and to the lack of local density variations in our model. (See the discussion in § 2.5.) While we have attempted to make fairly realistic choices for the parameters, we are certain that better choices and models could be made. The advantage is that the simplicity of these models allows us to explore the *relative* changes effected by fairly extreme variations in the evolution of PNs.

2.4 The Shklovsky Mass

In most of our simulations, we have tracked the evolution of each model PN from a high mass ($3M_{\odot}$) progenitor, varying several wind parameters and tracking the changes in the ionized envelope. We can now address the question of how the Shklovsky method works and reconcile the apparent theoretical and observational differences. We do this by, in effect, "observing" the models and estimating what mass would be calculated by the usual methods.

2.4.1 The Ionized Masses of Simulated PNs

From our simulations we can derive the apparent Shklovsky Mass of the ionized PNs (§2.2). We emphasize that this is not the actual ionized mass, but a value that would likely be derived from a standard analysis of observational

measurements of one of our model PNs. For this purpose, we need to review what standard practice has been.

First, it is common to consider only the radius of the bright inner portion of the ionized nebula without accounting for faint halo emission, as we described in §2.2.2. As an estimate of this practice we have defined a "Shklovsky radius" as the radius where the intensity of the PN falls to $1/e$ of the peak. This puts the observations on a unified scale and gives a value that agrees well with most of the radii reported in the literature. It is also similar to the actual criteria for angular sizes reported from radio measurements, which typically range between one tenth and one half of the peak brightness. Since there is usually a rapid drop of at least an order of magnitude in intensity at the outer edge of the dense shell (see Figure 2.2), the Shklovsky radius will not vary greatly for any other reasonable selection of relative isophotal level.

Second, generally the *integrated* radio flux from the nebula is used without considering the actual brightness distribution. As we showed in § 2.3, and as is apparent from column (9) of Table 2.3, this tends to be dominated by emission from the dense shell because of the n_i^2 dependence of the emission, so at least this assumption is consistent with the $1/e$ radius if one is estimating the mass of a PN's dense shell.

Third, a filling factor is typically used which reflects only the large-scale distribution of the brightest portions of the inner nebula. Often just an average value is applied to all PNs; for example, in §2.2 we adopted the value $\epsilon = 0.75$ used by Gathier (1987). Practically speaking, few PNs have observations sufficiently detailed to estimate ϵ much more accurately than this. Clearly the filling factor would be very much smaller if there was a large low-density halo, and the whole ionized nebula was considered (see §2.2.1).

The remarkable thing is that all three of these practices conspire to yield a Shklovsky mass which is far more nearly constant than the true ionized masses of planetary nebulae!

For PNs which are ionized beyond their dense shells (i.e. PNs which classically would be called "density bounded"), using measurements that reflect only the dense shell will effectively ignore the substantial mass of outer material. And for PNs that have not fully ionized their dense shells or that have very thin high-density shells, the use of an average filling factor tends to be an overestimate which causes the calculated ionized mass to be overestimated as well. Finally, in PNs with relatively weak fast winds, the shell density and mass are lower, but this allows a greater degree of ionization in the halo so that its emission can partially compensate for the smaller mass in the shell.

Without yet examining the properties of the individual models in detail, note that the Shklovsky mass in Table 2.3 remains generally in the range of a few tenths of a solar mass, even as the total ionized mass is sometimes over 100 times larger. The Shklovsky mass more nearly reflects the shell mass than the ionized mass, except when the shell grows too massive or is too dense (see the later time steps in Models 3 and 6 and the first time step in Model 7), and then the inability of the star to ionize the entire shell again yields a relatively small Shklovsky mass. Figure 2.3 illustrates the relationship between the total ionized mass and the Shklovsky mass relative to the fraction of emission arising in the dense shell. Note that the Shklovsky mass is a reasonable estimator of the true ionized mass only when ionization is limited to the shell ($M_i \leq M_{sh}$). Yet even though the fraction of emission from the shell never drops below ~40% in any of our models, the Shklovsky mass underestimates the total ionized mass by a factor of up to 170.

These models illustrate two important points: (1) the masses derived via standard methods bear little relationship to the true ionized mass of PNs, and (2)

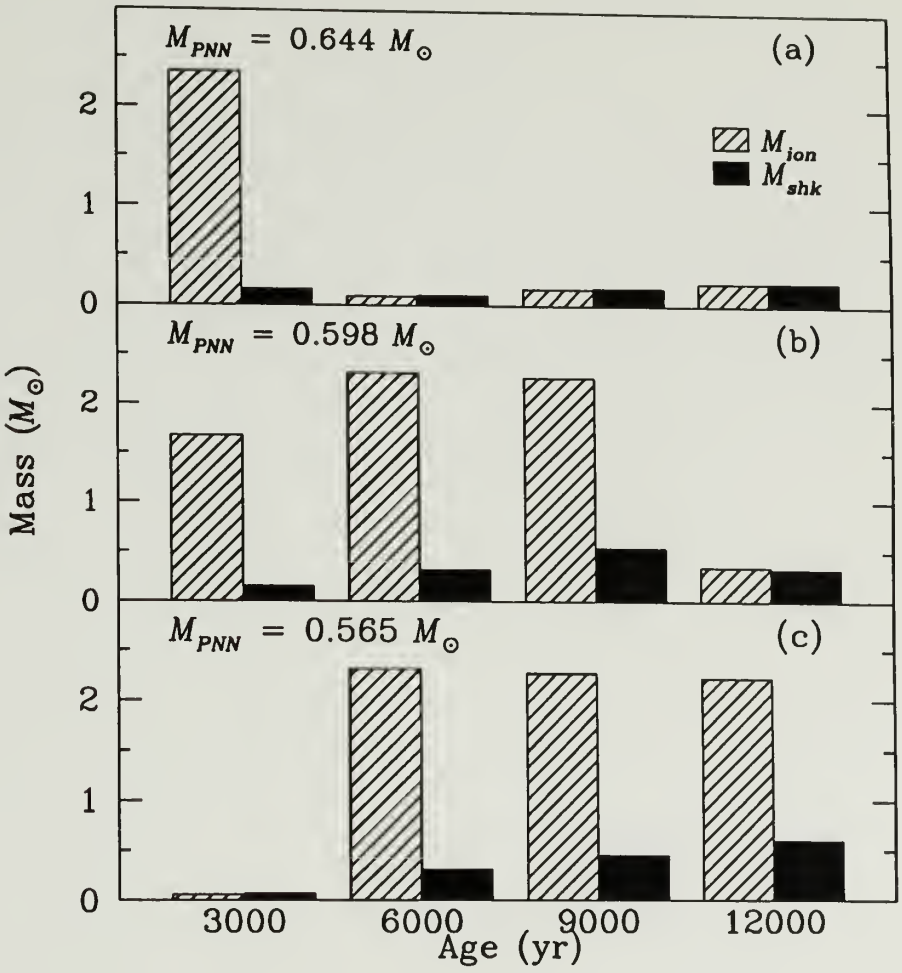

Figure 2.3. Total ionized mass (shaded bars) compared to the observed "Shklovsky mass" (unshaded bars) for the same nebular model, but with central stars of different masses. Because of their slower evolution, the less massive PNNs remain luminous enough to ionize the outer halo at later stages when the dropping nebular density makes ionization easier.

the derived masses generally remain around a few tenths of a solar mass for typical wind parameters. We turn next to a more detailed examination of the behavior of the individual simulations.

2.4.2 Behavior of the Model Nebulae

For most of the simulations, the Shklovsky masses and radii grow fairly steadily with time, even though the total ionized masses and the Strömgren radii vary quite radically. For the "typical" wind parameters chosen, the ionization encompasses all of the nebular material in most of the time steps of our simulations. (Differences from the total envelope mass of $\lesssim$3% usually result from incomplete ionization of the helium.) At times earlier than 3000 yr, the ionized mass must grow rapidly during the traditional "ionization bounded" phase as the central star increases in temperature.

Once the ionization front advances through the dense shell, the low density of the halo makes it relatively easy to ionize so that there can be fairly rapid jumps between when a small fraction and nearly the whole nebula are ionized. The Shklovsky mass remains generally about the same as the shell mass, typically on the order of tenths of a solar mass, and the bulk of the total ionized mass is present in the low density, low surface brightness remnant wind. In some models, this is followed by a decline in the ionized mass as the central star evolves to lower luminosities, so that the PNs are again ionization bounded. Also, in nebulae with very high AGB mass loss rates, the shell's high density can limit the ionization to just the inner part of the shell. This might correspond to the situation of well-evolved PNs that show outer neutral gas.

The general behavior of the nebula's growth in all the models can be understood by making some simple approximations. Normally, $\dot{M}_{\rm AGB} \gg \dot{m}_{\rm fast}$ and $v_{\rm fast} \gg V_{\rm AGB}$, so that equation 2.7 gives an approximate shell speed as:

$$V_{\rm shell} \sim V_{\rm AGB} \left(1 + \sqrt{\frac{\dot{m}_{\rm fast} v_{\rm fast}}{\dot{M}_{\rm AGB} V_{\rm AGB}}}\right) . \tag{2.15}$$

Likewise equation 2.8 yields an approximate shell mass of:

$$M_{\rm shell} \sim \sqrt{\frac{\dot{m}_{\rm fast} v_{\rm fast}}{\dot{M}_{\rm AGB} V_{\rm AGB}}} \dot{M}_{\rm AGB} t . \tag{2.16}$$

Thus the velocity and mass of the shell depend on the velocity and mass loss rate in the AGB wind, and somewhat more weakly on the ratio of the momenta of the two winds. The shell mass grows linearly with time while the shell velocity remains essentially constant.

A limitation of the two-wind model is that it requires the dense shell to be relatively thin so that momentum balance remains a reasonable approximation, yet at the same time the shell must not be too thin to be representative of the observed characteristics of PNs. These requirements place limits on the allowable range of wind parameters. The shell thickness depends primarily on the density distribution of the AGB wind and the momentum carried by the fast wind; it is roughly proportional to $V_{\rm shell}^{-1}$, so that a large momentum in the fast wind, a low AGB wind mass loss rate, or a high AGB wind speed all lead to a thinner shell. Some of the models (see column 10 of Table 2.2) have thinner shells than the appearance of real PNs would suggest is typical. It is not clear how the tuning between wind parameters is maintained in nature, although it may be that objects with very thin shells would not be classified as PNs. Another possibility is that exceptionally strong fast winds, which would otherwise produce thin shells, "break through" thinner regions of the envelope material, producing a normal thickness shell only in regions where the AGB wind is sufficiently dense. This would obviously deviate from the spherical geometry we assume here, although the calculations might still be reasonable for the fraction of the sphere where the snow-plowed shell arises.

In the other extreme, if the fast wind carries too little momentum, the internal pressure in the dense shell allows it to expand to such a degree that it no longer

obeys the thin-shell criterion. Several of our models encroach on this limit and may therefore be suspect. Yet some real PNs appear to have similarly large filling factors. To address this limit, we also consider (§2.4.2.6 below) a model in which there is *no* fast wind.

Beyond these general comments, the effects of each of the nebular parameters on the Shklovsky mass are not always obvious. We use Model 1 as a standard, and we consider the effects of variations of each parameter of our simulations individually:

2.4.3 Dependence on the Overall Mass Loss Rates

Model 1 has typical parameters that yield a reasonable shell thickness. With Models 2 and 3 we examine the effect of lowering and raising the mass loss rates for the two winds in unison. In this way, the ratio of wind momenta is conserved so that the shell velocity and thickness are maintained. The mass of the shell, however, goes approximately as $\sqrt{\dot{M}_{\rm AGB}\dot{m}_{\rm fast}}$, so that there is an order of magnitude range. (See equation 2.16.)

When the mass loss rates are both lower (Model 2), the dense shell is not very dense, so that the entire nebula can remain ionized. Furthermore, because of the low density, the emission from the nebula is very weak—possibly too weak to be identified as a PN given that its radio surface brightness is lower than any of the PNs in Table 2.1 even at the first time step.

The higher mass loss rate (Model 3) yields a more massive shell that the central star cannot keep fully ionized at all time steps. As a result the Shklovsky mass does not keep pace with the shell mass when it reaches its highest value in the last time step. Thus it seems likely that the Shklovsky mass is prevented from growing very large by the limited ability of the central star to ionize the nebula, and from being very small if it is to be identified as a PN.

2.4.3.1 *Dependence on the PNN Mass*

The differences in nebular properties over the range of PNN masses prove to be small when both the AGB and fast winds are fairly weak since the whole nebula becomes ionized. Models 4 and 5, which have higher and lower PNN masses, display virtually no difference in the derived Shklovsky masses and radii. At still lower mass loss rates, we find that the shell mass continues to decline and the Shklovsky mass also drops as $\sim \sqrt{\dot{M}_{\rm AGB}\dot{m}_{\rm fast}}$ (see equation 2.16), but the ionization of the outer envelope partially compensates for this lower mass.

However, when the winds are stronger and the shell is denser, the different ionizing abilities of the PNNs become apparent. Models 6 and 7 are like Model 3, except with higher and lower PNN masses. The high mass PNN begins with the highest luminosity and temperature, leading to a larger ionized mass initially, but because of the rapid evolution of the PNN, the ionized mass quickly drops. Conversely, the low mass PNN maintains a lower but steadier luminosity, so that its ionized mass remains large at later times. We illustrate this property in Figure 2.4, where we show the consequences of the different PNNs in the same high mass-loss-rate nebula.

For all three PNNs (Models 3, 6, and 7), the Shklovsky radii of the bright ionized regions are very similar as might be expected since the wind parameters are the same. The Shklovsky masses are also fairly similar, for the most part remaining in the range of a few tenths of a solar mass. The low-mass PNN produces the largest Shklovsky masses at later stages because of the laarger measured radio flux from the PN's ionized halo. Even so, its Shklovsky mass is only about three times larger than for the other two PNNs even though its total ionized mass is about ten times bigger.

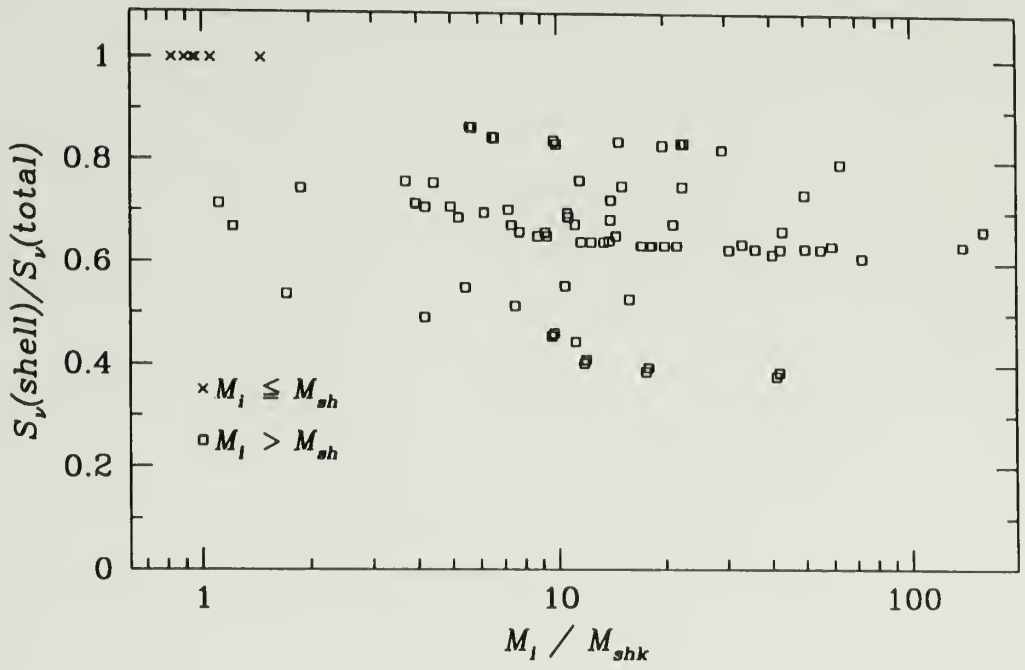

Figure 2.4. The fraction of the total radio continuum emission accounted for by the dense shell compared to the ratio of the true ionized mass to the Shklovsky mass. Note that the Shklovsky mass is close to the true ionized mass when all of the emission is from the dense shell, but the true ionized mass cannot be predicted even if the fraction of emission from the dense shell is known.

2.4.3.2 *Dependence on the Envelope Mass*

The effect of the total nebular mass on the estimated Shklovsky mass is very small. Models 8 and 9 are variants of Model 1, where we have assumed the presence of a 1 or 10 $M_{\odot}$ nebula. Even in a fully ionized 10 $M_{\odot}$ halo, $\sim$70% of the flux arises in the $< 0.3 M_{\odot}$ dense shell, and therefore the effects of the halo on the interpreted mass are minor.

We note in Model 10 the effect of a smaller nebular mass for the low-mass PNN, as one might expect if low-mass PNNs arise from lower mass progenitors (Weidemann 1987). The smaller available mass partially compensates for the higher level of ionization at later stages, particularly in the case of PNs with high mass-loss rates. This could reduce the variance of the low-mass PNN model from the others.

2.4.3.3 *Dependence on the Helium Fraction*

In Models 11 and 12 we show the effect of $\sim$3 times larger and smaller helium fractions than in Model 1. The Shklovsky masses remain in the range of a few tenths of a solar mass, but larger variations are seen when the helium abundance is larger (Model 12). This is a consequence of the helium ionization's greater sensitivity to temperature differences since it is ionized by the tail of the PNN's black body emission.

2.4.3.4 *Dependence on the AGB Wind*

The effects of varying the mass loss rate of the AGB wind are explored in Models 13–15, where $\dot{M}_{\rm AGB}$ is varied between 0.3 and 10 times the value in Model 1. Note that the Shklovsky mass is usually larger than the shell mass when it is particularly small. This appears to be due to the thinner shell that arises combined with our use of a fixed filling factor. On the other hand, for the highest AGB mass

loss rate (Model 15) the total ionized mass is smaller and the Shklovsky mass is only slightly larger than for the nebula with only 3% as large a mass loss rate. This occurs because of the star's inability to ionize the whole of a high-density shell.

The effects of varying the AGB wind speed between 3 and 30 km s^{-1} (Models 16 and 17) are quite significant on the total ionized mass, but fairly small with respect to the Shklovsky mass. A large V_{AGB} reduces the density of the AGB wind, making the interface between the two winds softer and the shell more easily ionized. The only substantial difference between the ionized masses in these two cases is during the final time step when the PNN has difficulty ionizing the whole dense shell arising from the 3 km s^{-1} wind.

2.4.3.5 Dependence on the Fast Wind

Changes in the fast wind's mass loss rate or speed (Models 18–21) produce nearly identical effects because the fast wind's overall momentum determines the density of the shell as it plows into the slower wind. A high-momentum fast wind will sweep up a more massive shell, but the difference in shell masses is not fully reflected in the Shklovsky mass again because of compensating emission from the halo when the momentum is smaller and difficulty in ionizing the whole high density shell when the momentum is higher. The net result is that with over a factor of ten variation in the fast wind momentum, less than a factor of two variation in the Shklovsky mass is seen at any time step.

We could not explore much lower momenta for the fast wind relative to the AGB wind because of the breakdown of the thin shell approximation in this case as we explained earlier. We therefore decided to consider a case in which there was *no* fast wind, and the nebula and central hole simply continued to expand at the original velocity V_{AGB}. With this "zero-momentum fast wind" (Model 22) the total radio fluxes are quite similar to the other models, but the Shklovsky radii are

somewhat smaller (and not as sharply defined), but the overall Shklovsky masses remain only a few times smaller than the values in Model 1. This suggests that low momentum fast winds should not produce results significantly different from those already tabulated.

2.5 Discussion

Despite widely variant characteristics of the simulations and despite substantially different *actual* ionized masses, we find basically consistent values for the "Shklovsky mass." We believe this resolves two important puzzles in PN research: why the Shklovsky distance method works as well as it does, and where the "missing matter" associated with high mass progenitors is located. Both appear to be related to a failure to consider the mass of the PNs halo, in the first case happily so! The model used, however, is rather simple, and several questions might be asked about its applicability to real PNs. We discuss these questions next.

2.5.1 Structure of the Nebula

The two-wind model does not reflect the complex geometry of most PNs, yet it does capture some essential features. It has a high-density inner shell, which dominates the emission from ionized gas in the nebula and effectively masks the significance of the emission from a low-density halo. Sometimes the high-density shell can even absorb all of the ionizing photons without becoming fully-ionized itself at later stages of a PN's lifetime, contrary to the usual assumption that the "ionization-bounded" phase occurs only early on. This permits the presence of a dense neutral region in older PNs, where molecules might be found as is observed in some cases. The model also displays what basic physical changes (density, shell

thickness, total radio emission) might occur when the characteristics of the colliding winds are varied.

The three-dimensional structure of PNs is probably better represented by a more nearly toroidal dense shell with lower density gas extending out in a bipolar fashion. Frank et al. (1993), for example, have demonstrated that the general appearance of the bright inner regions in most PNs can be explained by various projections of such a model generated in a two-dimensional hydrodynamic code. As far as the Shklovsky mass estimates are concerned, our spherical shell models suggest what one might expect if PNs were represented by a family of toroidal shells of similar geometry: the dense shells would still dominate the integrated emission, but the total emission would be smaller roughly in proportion to the solid angle filled by the dense shell. Indeed we wonder if the somewhat high Shklovsky masses we find for our simulations might be explained by such a non-spherical geometry. With our model as it stands, we can achieve lower Shklovsky masses while maintaining realistic shell thicknesses only by dropping the mass-loss rates to very low levels. At these low levels, the nebula is always fully ionized, which appears contrary to detections of neutral gas in many PNs.

Our model also does not consider multiple-shell geometries. These can occur when several shifts in wind speed occur during a star's mass loss phase. Whenever the wind becomes faster, it can "snowplow" into the older wind, yielding a series of outer shells rather than the smoothly declining density we assume here (e.g., Frank, Balick, and Riley 1990). Because of their higher density, these shells are more effective at processing photons from the PNN than a more continuous lower-density halo, but they are still of such a low density that the inner shell dominates the total emission from the nebula. Thus the Shklovsky mass estimates are not significantly altered.

Finally, there is a great deal of uncertainty about the actual transition period between the termination of the AGB wind and the beginning of the fast wind. Details of the wind properties at this early stage are important because they have a strong impact on the mass and size the dense shell will attain during the first few thousand years. This is a particularly critical stage because the PNN is evolving on a similar time scale. At later stages the concerns are relaxed somewhat, both because the dense shell has grown to incorporate more of the wind material (in effect, representing a time-averaged result) and the PNN has entered its slower cooling phase.

Some models assume that the fast wind does not start until 1000–3000 yr after the AGB wind stops, although it is probably more reasonable to tie the onset (and evolution) of the fast wind to the PNN's temperature and luminosity. We do not think a delayed onset would affect the Shklovsky masses much given our results for model 22, which had similar values and no fast wind at all. At later stages, we think that if the fast wind declines as the PNN cools, this would actually improve the consistency of the Shklovsky masses since the dense shell would not increase as much in mass.

2.5.2 Further Variations on the Model

In addition to the simulations already described, we have also examined a wide range of other models, with significantly larger and smaller wind speeds and mass loss rates (within the restrictions imposed on the ratio of the wind momenta). We also varied the basic parameters of the PNNs used, varying their temperatures and luminosities by factors of two. The *total* ionized masses and Strömgren radii of the model PNs did vary greatly depending on the wind parameters and central star model used, but it was rare that Shklovsky mass in excess of $1M_{\odot}$ ever arose.

Low Shklovsky masses ($\sim$0.01 $M_\odot$) could occur when both winds were significantly weaker than is usually suggested, but in those cases one might argue that any such objects in nature would not be identified as PNs because of their low surface brightnesses. The mean radio surface brightnesses averaged within the Shklovsky radii for these "weak-wind" PNs were fainter than those of any of the PNs in Table 2.1 even at the 3000 year time step.

The present model, like most others, doesn't deal with local density variations, or "clumpiness." The net effect of clumpiness is to increase the value of $\langle n_i^2 \rangle / \langle n_i \rangle^2$ everywhere in the nebula. In consequence, the use of a filling factor based on the gross geometry of the nebula would cause the ionized mass to be overestimated. Boffi & Stanghellini (1993) do in fact find filling factors several times smaller than the geometrically derived values when they compare the emission to independent electron density estimates. If the local value of $\langle n_i^2 \rangle / \langle n_i \rangle^2$ remains constant (Boffi & Stanghellini find no correlation with nebular size), then we can treat the clumpiness simply as an increased efficiency of recombination everywhere in the nebula.

Tripling the recombination rate to simulate the effect of clumpiness had a surprisingly minor effect on the estimated Shklovsky masses, generally changing it by less than 25% in any single time step, although larger effects were occasionally seen in the first time step (and in Model 22 where there was no fast wind). The Shklovsky mass increased when there were plenty of ionizing photons available, for example in the "weak-wind" cases discussed above. On the other hand, for some of the denser, more massive shells in which the ionization was incomplete, the greater recombination efficiency resulted in a smaller ionization zone and a smaller Shklovsky mass. These competing effects actually narrowed the range of derived Shklovsky masses slightly, and averaged over all our models reduced the mean Shklovsky mass by 3%.

2.5.3 *The Range of Masses and the Shklovsky Method*

In §2.2.2 we showed that distances derived by the Shklovsky method were surprisingly accurate; statistically they were consistent with the independent distance estimates to 28% (1σ) once the uncertainties in the radii, fluxes, and other distances were considered as well. It certainly remains true that some PNs have significantly different masses than the mean, but the extremely large—three orders of magnitude—spread sometimes quoted based on samples like Gathier's (1987) are unrepresentative.

The uncertainty in the Shklovsky distances arises from the variance of the mass along with the variances of the filling factor and electron temperature. The results of our simulations suggest that assuming a constant filling factor may actually help to narrow the range of derived Shklovsky masses, while the dependence on electron temperature is so weak that its variations are insignificant for this derivation. If we attribute the 28% uncertainty entirely to the variations of the Shklovsky mass, then since $d \propto M_{shk}^{0.4}$, the standard deviation of $\log M_{shk}$ should be 30%.

The Shklovsky masses found in our various simulations do not necessarily form a complete or representative sample of PN characteristics, but they do explore various extremes of possible behavior. The standard deviation of $\log M_{shk}$ determined at all the time steps of all 22 simulations is 34%. (When we put in the larger recombination rate to account for clumpiness, as described above, the standard deviation drops to 31%.) We think the similarity of the standard deviations of real and model PNs is not entirely fortuitous. We note that the variances of the Shklovsky masses at each individual time step are smaller still. This suggests that the Shklovsky mass is tied to the evolution of the PNN, so that perhaps the narrow range of Shklovsky masses is ultimately linked to the narrow range of PNN masses. In Chapter 3 we show that one can derive distances (both

in theory and practice) that have an even smaller variance by considering the Shklovsky radius relative to the mean nebular surface brightness.

The mean value of our model Shklovsky masses is 0.15 $M_{\odot}$, several times higher than the mean value we found in §2.2.2 when we examined PNs with independent distance estimates. We can only achieve such low masses within the model's assumptions by making the AGB and fast winds quite weak—so weak that the nebula's radio surface brightnesses are substantially lower than any observed PNs, and the nebulae are entirely ionized at all times. As we discussed above, an alternative explanation is that the geometry of the nebula is non-spherical with the dense shell incompletely surrounding the PNN. Another factor may be that the average observed PN is younger than the mean age (7500 yr) of our simulations. In fact, most PNs with independent distance estimates have higher surface brightnesses and are smaller than the mean of our sample. Our 3000 year old simulated PNs have a mean mass of 0.067 $M_{\odot}$ and surface brightnesses more nearly comparable to the average PN.

2.5.4 Supporting Observations

Deep optical CCD observations have shown that outer rings and halos are common features around PNs (see for example Schwarz, Corradi & Melnick 1992). Although these features are all thought to be a result of massive stellar winds during the AGB stage, such winds are probably not as constant as in our simple simulations. Many planetaries also show an inner halo just beyond the bright rim of the snowplowed shell as well as a fainter outer halo (Balick 1989), suggesting variations in mass loss rates of the AGB wind or interaction with the interstellar medium or red giant wind. Many PNs also show large, faint outer rings at the edge of their outer halos; possibly where the AGB wind plows into the ambient interstellar medium (Balick 1989). Also, most PNs exhibit geometries which are

certainly not spherically symmetric. Still, our simplistic approach demonstrates that it is generally not appreciated how massive the outer halos may be. It seems likely that most PNs have either massive neutral envelopes or extended faint emission.

The true ionized mass of a fully ionized PN, both core and halo, requires a detailed analysis of the faint emission from the radial density profile. High sensitivity radio imaging of the outer structure of PNs would be ideally suited for such mass estimates since the outer nebula is optically thin in the radio regime and the complexities of radiative transfer of optical emission lines in an expanding medium can be avoided. Radio imaging has the added advantage of eliminating any ambiguity between emission from ionized gas and reflection nebulosity from dust. We report on such observations for two PNs in Chapter 4, but many more PNs should be observed.

We also note that a major limitation of current observational data is the lack of a consistent and unambiguous method of defining and reporting nebular radii. We find that defining a "Shklovsky" radius at $1/e$ of the peak emission yields good consistency for Shklovsky masses and distances in our model PNs and in real PNs with independent distance estimates. Until these measurements have been put on an equal footing, we urge caution in using catalog data for drawing conclusions about nebular sizes or masses.

2.6 Chapter Summary

We have used a simple momentum-conserving two-wind model for evolving planetary nebulae to investigate how PNs that apparently evolve from relatively high mass progenitor stars "masquerade" as low mass objects. We simulated the evolution of PNs from high mass progenitors with remaining cores of $0.565 M_{\odot}$ to $0.644 M_{\odot}$. A progenitor mass of $3 M_{\odot}$ was used for most of the models because it

was consistent with initial/final mass relations for PNNs, but results for progenitors with substantially higher or lower masses does not change the results significantly as long as they produce PNNs with a final mass near $0.6M_{\odot}$ as has been found observationally. We used a variety of wind speeds and mass loss rates as input to the models and calculated the apparent ionized masses (Shklovsky masses) that would be measured from observations of these model PNs.

Because of the strong dependence of emission on density, our model PNs with extended, massive ionized halos can have more than 90% of their radio continuum flux emitted from less than 3% of the mass. Figure 2.4 shows the fraction of the total flux from the dense shell compared to the ratio of the total ionized mass to the mass of the dense shell. Even when the ionized mass is more than 100 times that in the shell, the shell still accounts for about half of the total flux. Larger or smaller nebular envelopes do not much affect the Shklovsky mass, since the dense snowplowed shell is the main source of emission.

The extent of ionization depends on the interplay between the expansion of the nebula and the evolution of the PNN. Fortunately, the important inputs such as the central star mass (which determines the star's luminosity/temperature evolution) and the mass loss rates and speeds of the winds seem to exhibit relatively narrow ranges. In general, a more massive central star has somewhat less success in ionizing the PN beyond the dense shell because its rapid evolution does not allow the nebula to expand to sufficiently low densities to diminish the recombination rate. This phenomenon can be seen most clearly when the mass loss rates are larger (as in models 3, 6, and 7). A low mass central star reaches the peak of its ionizing luminosity more slowly, when the PN has become sufficiently tenuous to be easily ionized beyond the dense shell. This, however, makes little difference in the total emission of the PNs since most of it comes comes from the relatively small amount of mass within the dense shell.

There are several consequences for observations of PNs implied by these models:

- For those nebulae that are ionized beyond the dense "snow-plowed" shell; a low density, low surface brightness ionized halo can comprise the great majority of actual ionized matter while contributing only a small fraction of the total luminosity of the nebulae.
- Standard techniques for estimating PN ionized mass use only the bright inner portion of the PN. We call the resulting ionized mass the "Shklovsky mass" for our model nebulae. Since halos have generally not been used in the standard techniques for calculation of ionized mass of PNs with independently determined distances, the actual ionized mass of the PNs may be severely underestimated.
- The observed Shklovsky masses for our model PNs are quite insensitive to variations in wind parameters and the central star models used as input to our simulations. The Shklovsky masses of moderate aged PNs in our sample consistently remained on the order of a few tenths of a solar mass, even though the total ionized mass was ten times bigger in some cases.
- An error analysis of the derived "Shklovsky masses" of PNs with independent distance estimates (Gathier 1987) shows that the intrinsic variability of $\log M_i$ is 42% (1σ) when the propagation of errors in the input quantities is carefully considered.
- The small variance of the observed Shklovsky mass may explain why the Shklovsky distance method has been successful—we find a standard deviation in these "statistical distances" of 28%—despite the apparent error in its basic assumptions.

Chapter 3

The Distances of Planetary Nebulae and the Galactic Bulge

3.1 Introduction

The question of the distances of planetary nebulae (PNs) has remained a thorny problem for at least four decades. The problem has been reviewed numerous times (see, for example, Liller & Liller 1968, and Terzian 1993), without much seeming advancement toward a solution. A very few PNs have had distances determined by painstaking observations, but no simple and direct estimator has been found for the great majority of PNs. In this chapter we propose a new method which is supported by both theoretical simulations (Chapter 2) and empirical data for PNs. The method is similar to the Shklovsky (constant ionized mass) method, being based on straightforward measurements of just the angular size and radio flux density of the PNs, and appears to be accurate to better than 25% (1σ).

The determinations of ionized masses and distances of PNs have been closely interrelated ever since the 1950's when Shklovsky pointed out the connection between these quantities together with nebular fluxes and angular radii (see Chapter 1 and Osterbrock 1989). Unfortunately, the distances of PNs are fundamental to the determination of all of their other basic properties, and the determination of a PN's ionized mass depends strongly on its distance. Shklovsky's method sidesteps these problems by declaring the nebulae to have a constant fixed ionized mass. The method is particularly appealing now that radio continuum measurements of PNs are widely available, which do not require

corrections for interstellar extinction. Since the Shklovsky distance depends only weakly on the assumed mass ($M_i^{0.4}$), even a factor of two range in the true ionized masses would result in only 30% errors in the distances.

The constant mass assumption has been widely criticized as being too simplistic. A common attack is to argue that, based on PNs with independently determined distances, the inferred masses have much too wide a range to satisfy the constant mass assumption. However such an attack is meaningless unless the uncertainties in the derived masses are considered. As we demonstrated in Chapter 2, a sample of PNs with independently derived distances (Gathier 1987), which is sometimes used to argue against the constant mass assumption, is in fact consistent with the Shklovsky method distances to within ~30%. Such small errors would make these "statistical distances" more accurate than almost any other available method for determining PN distances.

Our simulated PNs in Chapter 2 show tremendous variations in the total ionized mass during their lifetimes. However, what is remarkable is that despite the variability of the total ionized mass, we also find that the Shklovsky method determines distances fairly well—not because the ionized masses are constant, but because of the way in which nebular masses are normally (mis)estimated. Based on a series of simulations, we found that under a wide variety of plausible nebular conditions the "Shklovsky mass" determined from the radio flux and the dimensions of the dense inner shell of PNs (as it is commonly measured in practice) rises gradually during a PN's lifetime, yet it could be wrong by more than two orders of magnitude relative to the total ionized mass at various stages of the PN's evolution.

The main objection to the Shklovsky method has been based on the behavior of the highest surface brightness and presumably youngest PNs. It has been previously suggested, and our simulations in Chapter 2 support the idea, that

these PNs have systematically lower ionized masses than the rest of the population. Consequently their distances are overestimated by the Shklovsky method. These young PNs are classically called "ionization bounded," on the assumption that they have not yet fully ionized the surrounding nebular gas, which is thought to occur later in a PN's lifetime when it becomes "density bounded" and, under the Shklovsky method's assumption, reaches a constant mass.

Several methods have been offered as "patches" for the Shklovsky method during the early period of PN development, using the surface brightness (which is distance independent at radio wavelengths) as the basis for re-estimating the mass. Daub (1982) proposed that PNs' ionized masses grow inversely in proportion to their surface brightnesses when they are young. Daub based his model on 14 PNs with independent distance estimates, although the "non-Shklovsky" portion of the relationship essentially relied on just four PNs. Milne (1982) on somewhat more theoretical grounds argued that the ionizing flux during the ionization bounded phase ought to be relatively constant so that the total PN luminosity would also be constant. Milne then chose a value for this luminosity to match the mean of 13 PNs that had been previously labeled as density bounded by different authors. Finally, Amnuel *et al.* (1984) proposed essentially the same method as Milne, but with a smooth transition to the later constant mass phase, and a slightly different choice for the scaling factors. The problem with all of these methods is that they were based on very small collections of nearby PNs with independent distance estimates, and no attempt was made to ascertain the completeness of the samples or the accuracy of the measurements.

Since these earlier attempts at modifying the Shklovsky method, a few dozen more PNs have had their distances determined fairly reliably by independent methods. We discussed in Chapter 2 the PNs from the work of Gathier (1987), which is the largest sample in which an attempt has been made to quantify the

uncertainty in the distances. Unfortunately, almost all of the available distances rely on methods which are subject to potentially large and systematic errors. A subtle problem is that most of the distances resulting from these methods are difficult to analyze properly because they have errors which are highly asymmetric. Thus, reddening, expansion, or foreground gas absorption data often permit very large distances within their range of uncertainty, although the errors are usually quoted as being symmetric. The remaining methods, which include a variety of clever astrophysical determinations, are too uncertain and potentially biased to be useful in calibrating the new distance method we propose here.

A potentially much larger sample of PNs with independently known distances is available in the Galactic bulge, and recent observational work has provided the data needed to test the Shklovsky method and its modifications. We make use of a sample of PNs selected on the basis of their small angular separations from the Galactic center, which are likely to be at the distance of the Galactic bulge given the PN population's strong concentration in this direction. Since it is not obvious that small angular separations equate to small physical separations from the Galactic center, we will examine this question in detail and address the dispute between Stasinska et al. (1991) and Pottasch & Zijlstra (1992) over the validity of the Shklovsky method for these PNs. Having established their degree of concentration to the Galactic center, we are also able to use these PNs to test and calibrate the new distance method we propose here.

Our new distance method is based on the observation that our simulations in Chapter 2 showed a fairly steady increase in "Shklovsky mass" during their lifetimes, at first rapidly and then more slowly at later times (and even decreasing somewhat in some of the simulations). By comparison, the distance scales of Daub (1982) and Milne (1982) essentially represent attempts to approximate the increasing mass during the early stages with a simple power law relationship

between the mass and surface brightness. We find that no single power law relationship is adequate over any extended period of the PN's development, although the observed behavior of the population as a whole approaches something like the Shklovsky relationship at late stages. Actually, we find it is better to examine the relationship between the nebular radius and surface brightness, since measurement errors introduce a smaller scatter in the radius than in the mass. We find that our simulations in Chapter 2 reproduce the observed relationship between these quantities very well, allowing us to establish a clear relationship between radio flux density, angular radius, and distance.

We begin in § 3.2 by examining the distribution of PNs in the direction of the Galactic center and showing the degree to which they are actually concentrated in the Galactic bulge. In § 3.3 we describe the available data for these PNs. In § 3.4 we examine the relationship between radius and nebular surface brightness for the Galactic bulge PNs, our simulated nebulae from Chapter 2, and Gathier's (1987) sample. We then introduce our new distance estimator. Finally, in § 3.5, we discuss possible implications of our new distance method, and its possible application to future PN studies.

3.2 Galactic Bulge PNs

The distribution of PNs with Galactic longitude (Figure 3.1) quite clearly indicates that a large fraction of PNs in the direction of the Galactic center must in fact be located inside the bulge. The gradual decrease in counts from $\sim$15° out to the anti-center region reflects the general exponential decline of stars within the Galactic disk, but the sharp rise in counts within 10° of the Galactic center can only be explained by a large excess within $R < R_0 \sin 10°$ (where R_0 is the distance of the Sun from the Galactic center). The location of these PNs within the bulge is

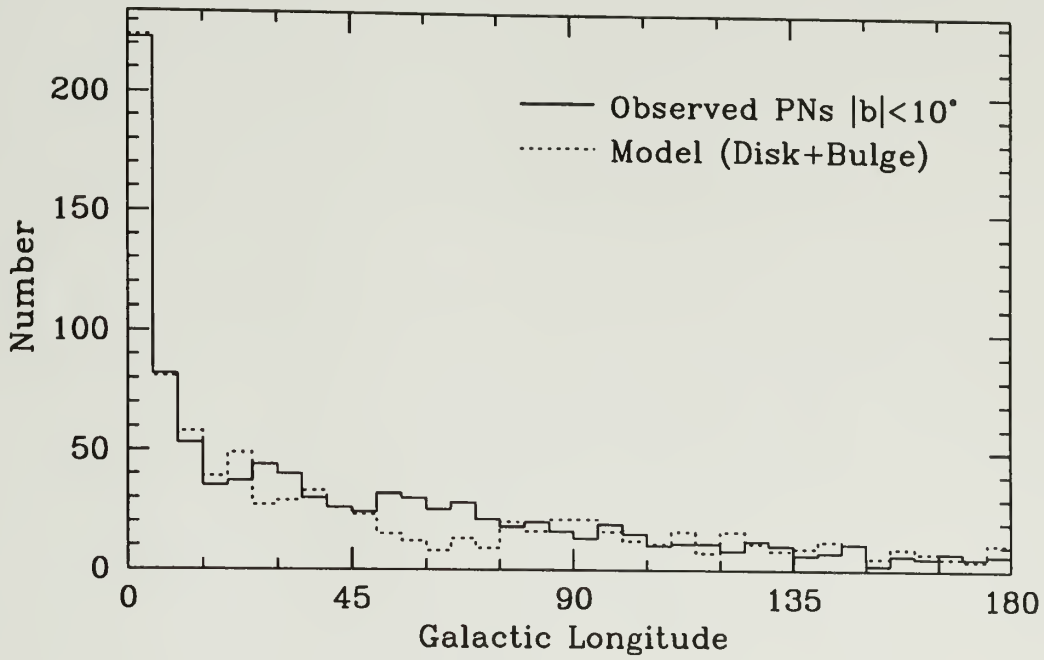

Figure 3.1. The distribution of $|b|$ <10° PNs in Galactic longitude. Data for the solid-line histogram are "true and probable" PNs from the *Strasbourg–ESO Catalog.* The dashed-line histogram shows the results of synthesized model distribution of Galactic PNs described in the text.

also demonstrated by the large radial velocities measured, often at velocities forbidden by normal Galactic rotation (see Schneider et al. 1983).

We limit our study to the 1143 "true and probable" PNs from Acker et al. (1993, hereafter the *Strasbourg–ESO Catalog*) in order to maintain a relatively uniform sample. A number of "possible" PNs have been identified, but they are less uniformly selected. The data in Figure 3.1 reflect the counts for the 947 PNs in the *Strasbourg–ESO Catalog* with $|b| < 10°$.

In Figure 3.1, if we simply extrapolate the counts from large longitudes, it appears that ~90 of the PNs with $|l| < 10°$ are actually disk PNs, and the remaining ~215 are then within the bulge. Thus PNs in this direction have, at least statistically, a fairly well-determined distance. We develop this idea more carefully in this section and then examine the available data for PNs in this direction in § 3.3.

To better quantify the range of distances of PNs angularly close to the Galactic center we synthesize the spatial distribution of a simulated population of PNs within the Galaxy and match them to the observed Galactic longitude distribution. We assume there are disk and bulge populations of PNs declining as e^{-R/R_s}, each with their own scale length, R_s. The Sun is assumed to be at a distance of 7.8 kpc from the center (Feast 1987) both because this appears to be a somewhat better estimate than the IAU standard of 8.5 kpc and in order to facilitate more direct comparison with the work of Pottasch & Zijlstra (1992). The values of R_s are treated as free parameters, and the PN populations are also allowed a range of possible scale heights perpendicular to the disk of order a few hundred pc.

To determine the *observed* distribution also requires a selection function. Here we assumed a fairly simple form for the probability of detecting a PN based on the fact that most of the *Strasbourg–ESO Catalog* PNs were identified based on their visible angular extent. Thus at any distance d the minimum physical radius of a

PN is $r_{min} = d\theta_{min}$, where θ_{min} is the minimum detectable angular radius. PNs grow approximately linearly with time and can be detected until their surface brightnesses become too low. We estimated the variation of surface brightness with radius from the PNs with independent distances (Gathier 1987; Chapter 2).

The run of surface brightness with radius was determined from radio data for which extinction is unimportant, and then was scaled to optical values and corrected for Galactic extinction. To estimate the Galactic extinction, we used *H I* and *CO* data from Burton & Gordon (1978) and Clemens, Sanders, & Scoville (1988). The extinction was scaled to the total hydrogen by yet another free parameter, but was required to approximately match the general extinction of $\sim$1.5 mag/kpc locally. We set θ_{min} to values ranging from 1–5″ and the limiting surface brightness to a fairly wide range of values similar to fainter nearby PNs.

We ran Monte-Carlo simulations of the PNs using various scale lengths and heights and varying the inputs to the selection function. It was again obvious that a separate highly-centrally peaked (small R_s) bulge population of PNs was necessary to explain the longitudinal distribution. We present one of our better fits to the observed data in Figure 3.1 with a dashed line. The disk scale length of this population is 3 kpc and the bulge has a scale length of 0.25 kpc. Actually we could have given the bulge an $r^{1/4}$-law distribution equally well; the large Galactic extinction near $b = 0$ unfortunately obscures the behavior at the very small radii where the behaviors might be distinguished.

We want to stress that the synthetic distribution we present is certainly not unique. There are many possible distributions and selection functions which reproduce a longitude distribution similar to that in Figure 3.1. The model we chose also reproduces the Galactic latitude distribution and PN angular size distributions fairly well, but this is a minor sidelight to the current investigation. For our purposes, *the synthetic distribution allows us to estimate what fraction of*

the PNs concentrated angularly close to the Galactic center are physically located there, and this result is quite insensitive to the details of which distribution was used.

The distribution of distances for PNs within 10° of the Galactic center in our synthetic distribution is shown in Figure 3.2. The distribution is strongly peaked at the Galactic center distance, but there are a fairly large number of nearby PNs that are selected as well. As a result the mean distance of the synthetic distribution is slightly smaller than the value of R_0 assumed: $7.36 \pm 2.06(1\sigma)$ kpc. Some of the PNs obviously nearer to the Sun than the Galactic center can be excluded by requiring the angular radius to be smaller than the largest expected angular size for PNs at the distance of the Galactic bulge ($\theta \lesssim 10$") and by requiring the total flux densities to be modest ($S_\nu \lesssim 100$ mJy), as suggested by Pottasch & Zijlstra (1992). In our synthetic data, these two requirements eliminate 34 of the 305 PNs within 10° of the Galactic center, and the resulting distribution is shown in Figure 3.2 with a dashed line. The resultant distribution has a mean distance of $7.77 \pm 1.64(1\sigma)$ kpc, reducing the scatter and bias about the Galactic center distance.

Also shown in Figure 3.2 is what 20% distance errors do to the apparent distribution of distances in the Galactic center direction, which is somewhat more representative of what one might anticipate measuring for PNs observed in this direction supposing that a good distance estimator had been found. This distribution is somewhat broader than one might expect given the sharp peak in the original data because of the large wings on the original distribution. The final distance and scatter (7.76 ± 2.32 kpc) is in line with what one would expect based on a simple sum (in quadrature) of the 20% error with the intrinsic scatter in distances. This suggests that it should be possible to estimate the accuracy of a

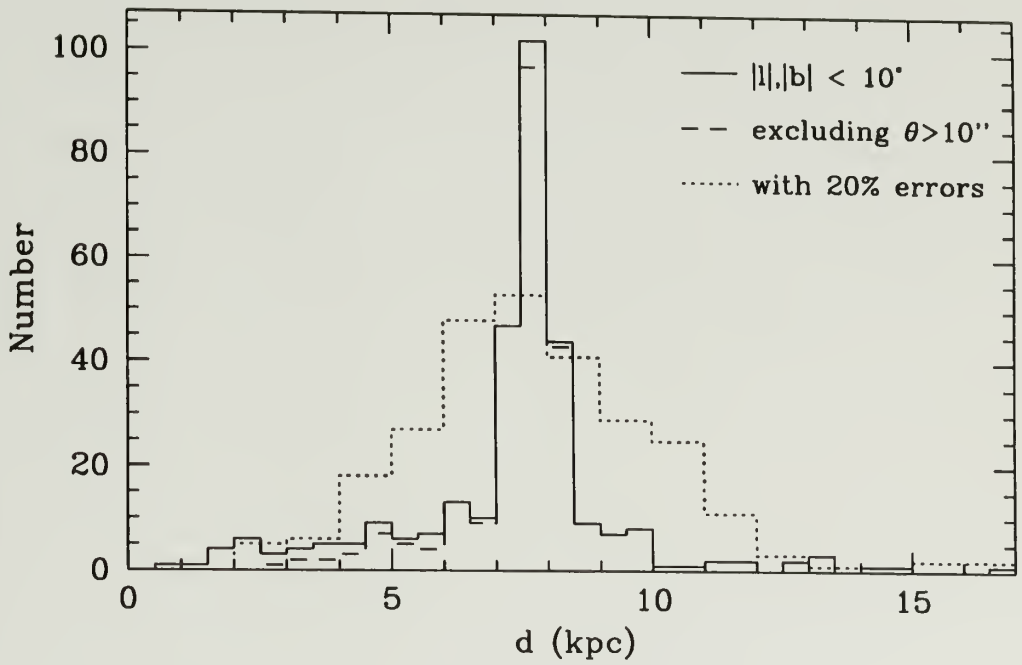

Figure 3.2. The expected distance distribution of PNs in the direction of the Galactic center. PNs with $|l|$ <10° and $|b|$ <10° were selected from our synthesized distribution and their distance distribution is presented as a solid-line histogram. By requiring that the angular size and flux densities be small (θ <10″ and S_ν <100 mJy) we can reject some nearby PNs, resulting in the dashed-line histogram. Finally we show the effects of 20% errors on these distance with a dotted-line histogram, where we have also doubled the bin width to make comparisons with the data for real PNs easier.

distance method for real PNs in the Galactic center direction by subtracting (in quadrature) a ~1.7 kpc intrinsic scatter.

Besides the synthetic distribution shown in this paper, we ran dozens of other models with differing scale lengths, scale heights, extinction laws, and selection criteria that were similarly successful in reproducing the longitudinal distribution of the PNs. They were not quite as favorable in their reproduction of the latitude, size, or "zone of avoidance" distribution of the PN population, but they all gave very similar mean distances for PNs within 10° of the Galactic center: from ~7.6 to 8.2 kpc. This is not particularly surprising since the longitudinal distribution requires the majority population of bulge PNs to be within $7.8 \sin 10° = 1.4$ kpc. The scatter in the distances did tend to be larger, because the distributions were skewed toward selecting nearer or more distant PNs, although the secondary selection criteria (maximum angular size and flux density) prevented much bias toward small distances.

3.3 The Galactic Bulge Data

In order to compare the bulge PNs to our nebular simulations in Chapter 2 and to test our new distance method we need both total radio flux densities and angular sizes. We select 5 GHz flux densities because PNs are normally optically thin at this frequency and measurements are widely available. Occasionally higher frequency data were the only available, in which case we scaled them to 5 GHz assuming the flux density is proportional to $\nu^{-0.1}$. We compiled data for both confirmed and and other possible PNs with both $|l| < 10°$ and $|b| < 10°$. A total of 305 confirmed *Strasbourg–ESO Catalog* PNs are located within this region, about half of which have adequate information to allow us to make distance estimates. Another 66 objects have been proposed as possible PNs and have radio flux

densities and radii available to test our distance method upon; we will return to consider these unconfirmed PNs in § 3.4.

Fortunately, several radio surveys have been conducted in the general Galactic center direction using both the VLA and Westerbork synthesis arrays (see Zijlstra, Pottasch, & Bignell 1989 and references therein) so that good flux densities and direct radio measurements of the radii are available for many of the bulge PNs. We used Zijlstra et al. to locate most of these data, but referred to the papers individually to ensure the accuracy of the values, and we incorporated data from more recent publications (notably Aaquist & Kwok 1990; Ratag et al. 1990; and Ratag & Pottasch 1991). Over 100 PNs have such measurements available, so that it is possible to base our primary tests on this sample of PNs alone, although we also examine results for PNs with optical radii and single-dish secondarily.

The total radio flux densities for angularly large PNs are sometimes underestimated by synthesis arrays because of a lack of short u–v spacings (also see Tylenda et al. 1992), but since our bulge sample includes only PNs with $\theta < 10''$ this is not likely to be a significant problem. To make sure of this and for PNs that had no synthesis measurements, we examined the single dish radio data from sources listed in the *Strasbourg–ESO Catalog.* In general the agreement was good, although many of the single-dish measurements were slightly larger. Most of the disagreements were for PNs with very small flux densities which were close to the sensitivity limits of those instruments, and often when a large discrepancy was present, there were large discrepancies between the different single-dish measurements as well. This suggests that the disagreements are due to confusion in the single-dish observations. In general, we average all of the synthesis data, and include the single-dish data when they are self consistent and the flux densities are greater than 50 mJy. A few exceptions with unexplained discrepancies are described below.

A much more significant concern is the accuracy of the angular radii. In fact, Pottasch & Zijlstra (1992) claim that the results of Stasinska et al. (1991) for Galactic bulge PNs are completely vitiated by the use of inaccurate angular radii. As we pointed out in Chapter 2, the situation regarding the angular measurements of PNs is in a sorry state. Authors frequently cite sizes from catalogs and compilations which ultimately can be traced back to very old sources like the hand-sketched figures of Curtis (1918). That the Shklovsky distance method has achieved *any* measure of success using such haphazard data appears remarkable.

The saving grace is that the best radius to use for the purpose of the Shklovsky method is the outer edge of the dense shell, which usually stands out in photographs (or even sketches). This can fail, though, when a single deep optical photograph is used to measure the radius. In this case the saturated PN image may extend into a low surface brightness halo. We suspect this is the explanation for the much smaller radii being found with modern CCD and synthesis imaging of a number of PNs in the Galactic center direction (Pottasch & Zijlstra 1992; Bedding & Zijlstra 1994). Actually, optical radii that are not saturated generally show excellent agreement with the radio measurements. However, to avoid uncertainties about the photographic measurements we restrict our primary analysis here to those PNs with radio-synthesis or modern calibrated optical estimates of the radius. As it happens, all of the PNs for which we found optical CCD data (primarily from Bedding & Zijlstra) also had radio synthesis measurements, so the radii were averaged.

The edge of the dense shell is not always well-defined, so we adopted a scheme in Chapter 2 of finding the radius where the surface brightness drops to $1/e$ of the average maximum brightness. This level is deep enough to incorporate the main body of dense gas, but not so deep that it would extend out into the halo. However, another complication arises for most of the bulge PNs. Here the angular

sizes are so small that the radio and optical measurements do not resolve the nebula well. In these cases it is still possible to estimate the radius of the dense shell according to the broadening of the image relative to the radio synthesized beam or optical point spread function. Unfortunately again, this has rarely been done properly or consistently.

In order to estimate the size of a PN whose image has been convolved with a beam, one must assume a brightness distribution and then calculate the broadening that the beam introduces. There are a variety of brightness distributions that might be used to describe an unresolved nebula, including an optically thin sphere, a uniform brightness disk, or a spherical shell. As Bedding & Zijlstra (1994) show, results for a disk model typically fall between the shell and sphere; therefore, since the actual degree of shell development is usually unknown, we adopt the disk model as a compromise.

The disk model is considered by Panagia & Walmsley (1978), and many authors quote this paper as justification for applying a factor of 1.8 correction to their "Gaussian diameters" (defined as the difference in quadrature of the convolved PN image diameter and the beam width). However, as Panagia & Walmsley show, a factor of 1.8 is only appropriate when the source is at least several times smaller than the beam, which is rarely the situation for these measurements. The correction factor becomes smaller as the PN's size grows larger relative to the beam. To understand this behavior as a function of the convolved image size, we have performed the convolution of a Gaussian beam with a disk model, like Panagia & Walmsley, but over a wider range of image diameters. We find that the diameter (Θ_{PN}) of the disk can be estimated quite accurately from the half-power beam width (Θ_{beam}) and the convolved half-power image diameter (Θ_{obs}) as:

$$\Theta_{PN} \approx \Theta_{obs} \left(1.0 + 0.8e^{-0.7\Theta_{obs}/\Theta_{beam}}\right) . \qquad (3.1)$$

Another complication arises from the fact that most authors (including Panagia & Walmsley) apparently fit a Gaussian to the convolved image rather than directly measuring its size. A Gaussian will always underestimate the diameter of a disk even when it is well resolved so that for a the full width at half maximum of the Gaussian fit (Θ_{gauss}) the PN diameter is:

$$\Theta_{PN} \approx \Theta_{gauss} \left(1.23 + 0.57 e^{-0.7\Theta_{gauss}/\Theta_{beam}}\right) . \tag{3.2}$$

Note that this also provides some additional justification for our preference of the $1/e$ radius, since this radius is 1.2 times larger than a Gaussian's half-power radius. Finally, when the beam is elongated, as is usually the case for northern radio synthesis observations of the Galactic center, the corrected radius should be estimated as the geometric mean of equation 3.2 using the major and minor axis beam diameters.

We have applied the above procedure to the papers which quote Gaussian diameters for their PNs (Kwok, Purton, & Keenan 1981; Gathier et al. 1983; Pottasch et al. 1988; Ratag et al. 1990; Ratag & Pottasch 1991). The beam sizes for the individual observations were not listed in any of these papers, so we adopted typical values for Galactic center observations depending on the array used: $0''.4 \times 0''.8$, $1''.1 \times 2''.2$, $3'' \times 6''$, and $5'' \times 25''$ for the VLA A–, B–, and C–arrays, and Westerbork array respectively. Several of these papers also mention that some small number of (unidentified) PNs were reduced in a different way if they were clearly resolved, but without more specific information we cannot treat them separately—at least, though, with the above scheme we are not applying very large corrections to the most easily resolved nebula. Finally, we directly adopted diameters that were themselves based on a deconvolution of the PN image size (Phillips & Mampaso 1988; Zijlstra et al. 1989; and θ_{disk} in Bedding & Zijlstra 1994). Aaquist & Kwok (1990) apparently handled some PNs in each way,

multiplying their Gaussian diameters by 1.8, but since it was uncertain which were handled this way, we simply adopted their values.

A few PNs require special treatment because conflicting values are reported in the literature. PN359.8+06.9 has a radio diameter of 2″.2 according to Zijlstra et al. 1989, but Ratag & Pottasch list its radio diameter as 9″.8 (after we apply equation 3.2) and it has an optical diameter of 10″ according to the *Strasbourg–ESO Catalog*, so we have adopted the latter value. PN006.4+02.0 has a radio diameter of 7″ according to Zijlstra et al., but Bedding & Zijlstra (1994) give an optical CCD diameter of 2″.2 and indicate that the radio diameter is unreliable, so we adopt the optical size. The flux density of PN356.9+04.5 reported by Pottasch et al. (1988) is only about 10% of values reported by several other authors and is assumed to be in error. PN005.8–06.1 has a reported flux density of 3.5 mJy according to Zijlstra et al. (1989), but Isaacman (1984) reports a synthesis measurement of 16 mJy, and single-dish measurements lie in between; we adopt an intermediate value of 10 mJy

As Pottasch & Zijlstra (1992) suggest, and as we have described in § 3.2, we do not assume that PNs with large radio flux densities or large angular sizes are in the Galactic bulge. A total of nine objects were eliminated as a result of these criteria, leaving us with a sample of 118 PNs. (Of the 191 bulge PNs with any kind of measurement of the radius and flux density, 18 would be eliminated.) We note that as a fraction of the sample the 9/127 (or 18/191) removed is similar to the 34/305 removed in the synthetic distribution of Galactic PNs presented in § 3.2.

Another 44 *Strasbourg–ESO Catalog* PNs met all of these criteria, but they had only photographic measurements of the radius available and their flux densities were mostly measured with single-dish instruments; since the radii of these PNs are potentially incorrect, we treat them as a secondary sample. Finally, we have a third sample of 66 objects that meet these criteria, but which are not

yet confirmed to be PNs. Most of these objects were detected in radio surveys of objects with PN-like far-infrared colors, although a few are objects whose identity is still in dispute and were therefore placed on the "possible" list in the *Strasbourg–ESO Catalog.*

Based on the analysis in § 3.2, we expect the PNs in this sample to have an average distance of $7.80 \pm 1.64 kpc$, but we note again that skewing of the distribution could occur if the true selection function is different than we assume. Variations in the selection function should not much affect the *peak* of the distribution (since the PNs concentrated in the bulge all obey approximately the same selection rule), but it could substantially affect the outlying distribution. This should be kept in mind particularly for the inverse problem of determining the distance to the Galactic center based on the *average* of the distances of the Galactic center PNs.

3.4 The Radius–Surface Brightness Distance Method

As we saw in Chapter 1.2, the distance equation 1.3 shows that the distance to a PN can be measured using an assumed ionized mass along with the distance independent observable quantities of angular radius θ, and mean surface brightness I_ν. The Shklovsky method proposes that PNs' ionized masses are all the same, so that the M_i term in equation 1.3 becomes part of the constant of proportionality. However, it is clear that at least in the case of young "ionization bounded" PNs whose ionization fronts have not yet expanded very far into the circumstellar material, the mass dependence cannot be ignored. In these cases the Shklovsky method overestimates the distance since it overestimates M_i.

As we discussed in § 3.1, the usual way of avoiding this problem is to identify the young PNs and to assign them progressively smaller masses when they are younger. The best way to identify young PNs appears to be by their mean surface

brightness $I_\nu = S_\nu/(\pi\theta^2)$, which is a distance-independent quantity at radio wavelengths. For example, given a constant ionized mass, the surface brightness is much higher when the nebular radius is smaller: $I_\nu \propto M_i^2/r^5$. Even if the ionized mass is smaller than the constant Shklovsky value, as long as it does not depend on the radius more strongly than $r^{5/2}$, the surface brightness will continue to be a monotonically decreasing function of radius.

Variations on the Shklovsky method work essentially by identifying a new mass–surface brightness relationship. Milne's (1982) constant-luminosity assumption gives a distance at early stages of $d_{cl} \propto S_\nu^{-1/2}$, or equivalently $M_i \propto r^{3/2}$ so that the mass depends on surface brightness as $I_\nu^{-3/4}$. Daub's (1982) inverse-surface-brightness assumption ($M_i \propto I_\nu^{-1}$) is equivalent to a mass–radius relationship of $M_i \propto r^{5/3}$, and yields a distance $d_{isb} \propto S_\nu^{-3/5}\theta^{-1/5}$. Both of these variations revert to the Shklovsky method at later stages when the ionized mass reaches the Shklovsky value of $\sim 0.1 M_\odot$ and the nebula should be "density bounded."

These alternative methods were calibrated using a few young PNs—far too few PNs to accurately test the validity of the methods' assumptions about the nebular growth. But this may not have been their biggest problem; attempts to determine ionized mass as a function of surface brightness can prove treacherous for several reasons: (1) M_i depends on a high power of the distance ($d^{5/2}$), and the independent distances are often very uncertain. (2) M_i also depends on the angular size and flux density, so they can contribute large uncertainties too. Moreover, (3) the neglected nebular temperatures and filling factors seem likely to change systematically as a function of a nebula's age and may therefore affect the mass–surface brightness relationship in some unknown way.

An alternative approach is to note that all of the above methods can be cast in terms of a relationship between the surface brightness and *radius* of a PN, with the

advantage that the radius is affected much more weakly by errors in distance or other nebular parameters. Recast this way, Shklovsky's constant mass assumption implicitly defines a relationship $r \propto I_\nu^{-1/5}$. The constant luminosity relationship gives $r \propto I_\nu^{-1/2}$, and the inverse surface brightness relationship gives $r \propto I_\nu^{-3/5}$.

In Figure 3.3 we plot the radii and surface brightnesses for the Galactic center PNs assuming they are all at a distance of 7.8 kpc. In addition we plot local PNs with independent distances and our simulated PNs from Chapter 2. It is immediately apparent that all three samples show a well-defined relationship between radius and surface brightness. The bulge PNs are generally higher in surface brightness, which we believe is a selection effect derived from the requirement of optical identification combined with the large extinction toward the Galactic center. Conversely, our simulated PNs are mostly restricted to low surface brightnesses since we traced their behavior only after 3000 years (because of the large uncertainty in initial and early conditions). Nevertheless, throughout the range of overlap, all three samples agree with each other remarkably well, defining a theoretical/empirical relationship between radius and surface brightness.

We also show in Figure 3.3 a straight line describing the constant mass (Shklovsky) relationship, along with the relationships adopted by Daub (1982) and Milne (1982). Note that for the large, low surface brightness PNs the Shklovsky relationship is in good agreement with the empirical relationship defined by the data. However, it overestimates the radii of high surface brightness PNs by a factor that grows larger for PNs of successively higher surface brightnesses. Daub's and Milne's relationships predict smaller radii for these high surface brightness PNs, but they substantially over-correct the problem. Also note that most of the local PNs with independent distance estimates are of lower surface brightnesses, which explains the generally good agreement we found between the Shklovsky and independent distance estimates in Chapter 2. Based on Figure 3.3, though, we can

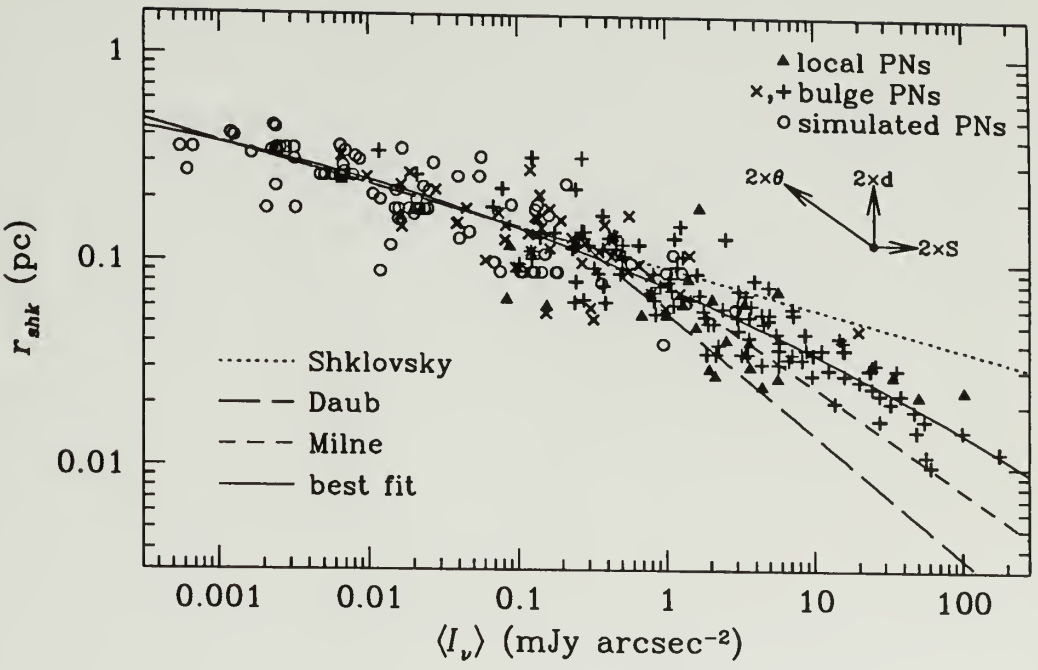

Figure 3.3. The radius–surface brightness relationship of PNs. We plot the radius of the dense shell ("Shklovsky radius") against the mean 6-cm radio surface brightness (defined as the total flux density divided by the area of the dense shell) for PNs with independent distance information. Plotted are (△) local PNs with various distance estimates (see Chapter 2), (+) bulge PNs from our primary sample, (×) bulge PNs with photographic estimates of the radii, and (○) simulated PNs from Chapter 2 (Table 2.3). The lines show the relationship predicted between radius and surface brightness under Shklovsky's constant mass assumption, Milne's (1982) constant luminosity modification, Daub's (1982) inverse surface brightness modification, and our own second-order best fit. The arrow show the effects on a data point of doubling the angular size, flux density or distance.

anticipate that the Shklovsky method will overestimate the distances of many of the bulge PNs and the other two methods will underestimate them.

The data for the real PNs do not appear to obey any simple power law or even a pair of power laws over different ranges as assumed by Daub and by Milne. The points seem to follow a smooth curve in the $\log I_\nu$–$\log r$ plane. As the simplest of approximations to this behavior, we have made a second-order polynomial fit:

$$\log r = a(\log\langle I_\nu\rangle)^2 + b(\log\langle I_\nu\rangle) + c \; . \tag{3.3}$$

The coefficients of the least-squares best fit to the primary Galactic center sample (+'s in diagram) together with the local PNs are: $a = -0.0264$; $b = -0.307$; $c = 1.113$, where $\langle I_\nu\rangle$ is measured in $mJyarcsec^2$ at 5 GHz and r is given in parsecs. The solid curve shows this fit to the data. This is not the most elegant of formulations, but it is relatively simple to calculate the distance then as:

$$\log d = \log r - \log\theta + \log 206.265 \tag{3.4}$$

where d is measured in kpc, r in pc, and θ in arcsec.

The important aspect of this new relationship is its relatively small scatter. The primary sample of bulge PNs shows a standard deviation around the best fit curve of ± 0.134 in $\log r$, which corresponds to a 36% variance in r (1σ). Note that this error does *not* correct for the intrinsic spread of ~22% expected for the distances in the bulge PN sample. Subtracting that variance leaves only a 27% scatter unaccounted for. Even this uncertainty does not account for scatter introduced by measurement errors in S_ν or θ. The best fit relationship therefore appears to be accurate to better than ~25%.

Likewise, we can test the best fit relationship against the local PNs with independent distances (see Chapter 2), shown as triangles in Figure 3.3. These PNs agree to better than 15% in the mean (within a few percent if several outliers are ignored), but they display a somewhat greater scatter about the best fit line of

± 0.196 in $\log r$ (56% in r). After adjusting for the uncertainties in the independent distances, the flux densities, and the radii, the remaining scatter is about 35%. This is not quite as good as for the bulge PN sample, but we have suspicions about the validity of some of the independent distances, so we believe the scatter in the bulge PNs is more representative.

Another way of examining the accuracy of the relationship is to directly test the distances it predicts. In Figure 3.4 we show a histogram of the predicted distances of the bulge PNs like that in Figure 3.2 using three different methods.

The dotted-line histogram shows the distances predicted by the Shklovsky method. Stasinska et al. (1991) and Pottasch & Zijlstra (1992) produced essentially similar graphs to argue, respectively, in favor of and against the Shklovsky method. In Figure 3.4 the histogram of Shklovsky distances matches poorly with the Galactic center distance, in seeming agreement with Pottasch & Zijlstra. However, this is not entirely fair because we could have produced a better fit by changing the Shklovsky mass to a smaller value so that the mean distance for all the PNs was smaller. Lowering the Shklovsky mass would be equivalent to a downward shift of the line for the Shklovsky model in Figure 3.3, which would still leave the small PNs with systematically large distances and the large PNs with systematically small distances. This choice of Shklovsky mass (or the constant of proportionality in equation 1.3) appears to be the main source of the dispute between Stasinska et al. and Pottasch & Zijlstra. Based on the changing slope of the r–$\langle I_\nu \rangle$ relationship, we would argue that the Shklovsky method works well for low surface brightness PNs.

Also shown in Figure 3.4 is the distribution of distances predicted by Daub's (1982) method (dashed line). As anticipated, Daub's method underestimates the distance of high surface brightness PNs (in contrast to Shklovsky's method), and this proves to be a particularly severe problem here because so many of the selected

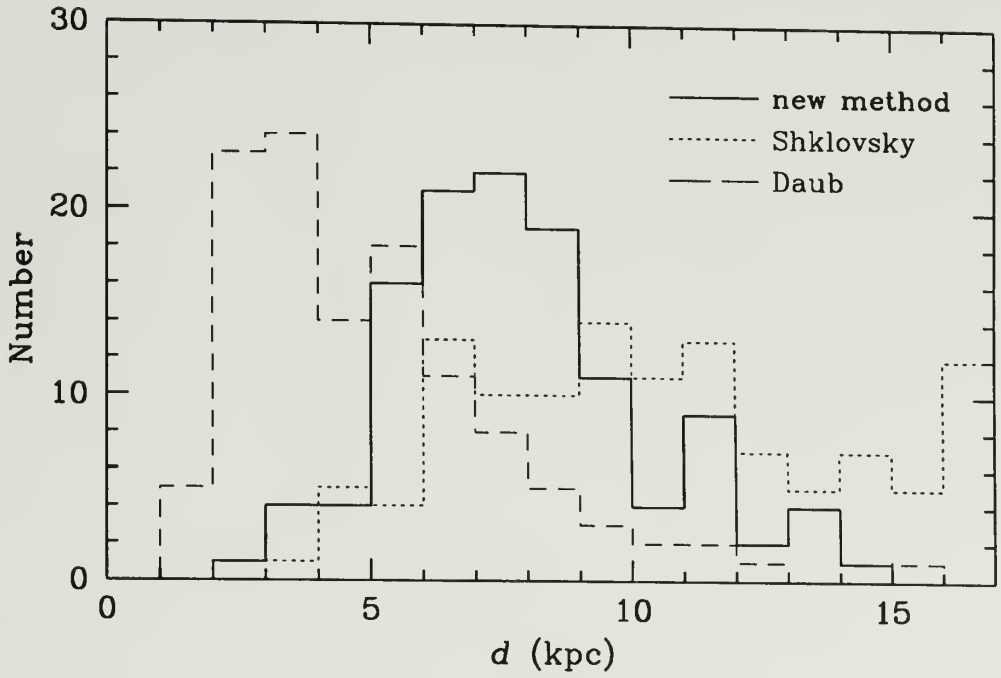

Figure 3.4. The distance distribution of bulge PNs from our primary sample. We show histograms of the predicted distances of bulge PNs using Shklovsky's method, Daub's (1982) method, and the new method proposed here.

PNs have high surface brightnesses. Milne's (1982) method likewise underestimates most of the PNs' distances, although not as severely as Daub's method.

Finally, in Figure 3.4 we show with a solid line the distribution of distances resulting from our new method. Obviously, since we assigned the mean distance of the Galactic center to these PNs, it is no surprise that we recover a good match to this distance in the mean. What is encouraging, though, is how small the scatter is around this mean and how similar it looks to the synthesized distribution of distances with 20% errors in Figure 3.2. For the 118 PNs in our primary bulge sample, the mean and standard deviation of the distances given by our method is $7.89 \pm 2.36 kpc$. The set of model PNs with 20% distance errors in Figure 3.2, have a mean and standard deviation of $7.76 \pm 2.32 kpc$. Thus, our distance method appears to be achieving an accuracy of $\sim$20% based on this comparison, even though we use imperfect measurements of the angular sizes and flux densities.

One helpful factor in keeping the scatter so small is that errors in angular size or flux density move points at only a small angle relative to the best fit line in the $\log r$–$\log\langle I_\nu \rangle$ plane. The arrows in Figure 3.3 show the effect of doubling S_ν, θ, or d while keeping the other variables fixed. The effect of measurement errors on the distance can be found by taking the partial derivatives of equation 3.4 with respect to S_ν and θ, yielding:

$$\Delta(\log d) \approx -[0.053(\log\langle I_\nu \rangle) + 0.307]\Delta(\log S_\nu) \tag{3.5}$$

and

$$\Delta(\log d) \approx [0.106(\log\langle I_\nu \rangle) - 0.386]\Delta(\log \theta)\ , \tag{3.6}$$

where $\langle I_\nu \rangle$ is measured in $mJyarcsec^{-}2$ as before. Assuming that the errors in θ and S_ν were uncorrelated, we could estimate the *measurement* uncertainty in $\log d$ by the sum in quadrature of the two above terms.

Note that errors in θ for high surface brightness PNs ($\log\langle I_\nu \rangle > 0$) move points in the $\log r$–$\log\langle I_\nu \rangle$ plane (Figure 3.3) almost parallel to the best fit line, which means that the derived distance is only weakly affected by errors in θ. For the highest surface brightnesses in our sample of $\sim$100 $mJyarcsec^{-}2$, equation 3.6 indicates that the error in $\log d$ is less than 20% of the error in $\log \theta$, so that an error of a factor of 2 uncertainty in θ would introduce only a $\sim$15% uncertainty in d. This is fortuitous since these smallest PNs generally have the hardest sizes to measure. Conversely, the distances of the lowest surface brightness PNs are little affected by errors in S_ν, which is again fortuitous because the flux densities are more uncertain for the largest PNs.

Given this weak dependence on the measurement errors, we would expect that PNs with more uncertain measurements should still show a relatively small scatter in their distances. This is in fact borne out by the data for bulge PNs in our secondary sample, which had optical estimates of their radii and mostly single-dish flux densities. These 44 PNs had a mean distance and standard deviation of 8.18 ± 3.00, which implies errors of $\sim$30% in the distance after subtracting off the expected uncertainty in distances for our bulge PNs.

We have also applied the method to the 64 "possible" bulge PNs. These have a mean and standard deviation of $9.86 \pm 3.85 kpc$, but the problem appears to be confined to $\sim$15 PNs which all have distances larger than 13 kpc implied by the method. The remainder were as tightly clustered around the expected Galactic center distance as the primary sample of bulge PNs.

Because we are uncertain about the precise contribution of errors in the measurements of θ and S_ν, it remains difficult to determine the level of *intrinsic* uncertainty in our new distance method. Since the method shows only $\sim$20% errors for the best-measured bulge PNs, and because the errors in θ and S_ν enter so weakly, we will conservatively estimate the intrinsic uncertainty as 20% (1σ). In

fact, the intrinsic uncertainty may be still smaller, but such a determination awaits more accurate measurements of more PN distances along with accurate sizes and flux densities. For the time being, we would recommend estimating the error at 20% added quadratically to the propagated observational errors in equation 3.5 and equation 3.6.

3.5 Discussion

The distance method for PNs proposed here differs from previous "statistical" methods in two important respects: (1) much more independent distance data is made available by using properly-selected bulge PNs, and (2) we focus on the radius–surface brightness relationship instead of masses and surface brightnesses. We illustrate the importance of this latter point by producing a plot of the mass dependence of PNs in Figure 3.5, calculated assuming the PNs all have an electron temperature of 10^4 K and a filling factor of 0.75 (see Chapter 2). In contrast to the radii in Figure 3.3, the trend of masses with surface brightnesses is not as consistent for the different samples of real and simulated PNs. There is also a much larger scatter in the masses, but this is roughly in proportion to the larger effect of distance on the mass ($d^{5/2}$ vs. d^1 for the radius).

It is possible to use the mass data and invert the process—deriving distances based on the masses for a given PN's surface brightness—in exactly the same way as we earlier made a best fit to the radii. Using the same set of PNs and fitting a second order polynomial to the log–log relationship, the resulting scatter in PN distances of our primary bulge sample is ± 2.52 compared to ± 2.36 using our radius–surface brightness relationship. After subtracting the bulge PNs' intrinsic distance variation, this corresponds to a 25% uncertainty compared to a 22% uncertainty earlier. This increase in the uncertainties probably arises from the additional dependence of the mass on the flux density, and though it is small,

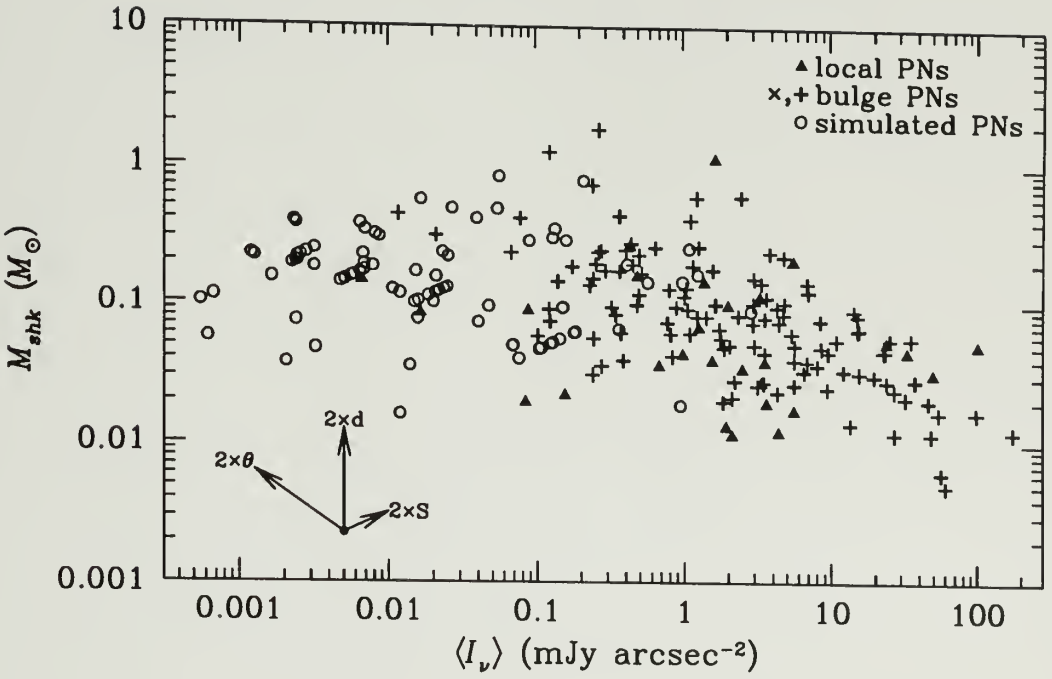

Figure 3.5. The mass–surface brightness relationship of PNs. The ionized masses for the same PNs shown in Fig. 3. Note that these are not true ionized masses, but "Shklovsky masses" (see Chapter 2).

there appears to be no advantage to using masses over radii. One significant problem that does arise in trying to find a mass–surface brightness model is that the fits for various subsamples of the data do not agree well with each other. There are much larger systematic differences between the mass behavior of the local, bulge, and simulated samples than in their radii.

The consistency of the nebular radii is one of the more interesting implications of this study. Perhaps this is not surprising since the radius of the dense shell is largely determined by basic momentum conservation, while the mass is sensitive to more aspects of the nebular wind parameters. We could have, for example, used the radius–surface brightness relationship as determined by the simulated nebulae of Chapter 2) to predict nebular distances. In fact, we carried out this calculation for the primary sample of bulge PNs, making a second-order fit to the logarithms just as we did earlier, and derived a mean distance and standard deviation of the bulge PNs of $8.30 \pm 2.59 kpc$. This standard deviation is nearly as small as that based on the fit to the actual bulge data, and *the mean value of 8.3 kpc is based on no* a priori *information about the Galactic center distance.* This agreement between simulations and real data indicates that the conclusion of Chapter 2 about good qualitative consistency between models with widely different parameters can be expanded to a conclusion about good quantitative consistency.

The agreement is rather surprising given the simplicity of our simulations. We suggest that it is evidence that the important aspects of nebular evolution are not determined by the complicated geometries that some PNs exhibit, but by properties of PNs that are similar: the central star masses, the wind speeds, and the mass loss rates in the late stages just before the PN forms. (The wind parameters at earlier stages of the AGB phase have little consequence for the dense ionized regions where the radio emission arises.) Presumably at the late stages prior to the PN's formation, the character of the mass loss changes as the

gravity weakens and the hot PN nucleus becomes exposed. It seems likely that what is initially a slow wind being driven by radiation pressure on grains forming at a large distance from the PN nucleus becomes a fast wind driven by resonant line absorption and gas heating close to the star. The narrow range of masses found for PN nuclei and the similarity of their wind parameters follow from the similar physical parameters required at the onset of this stage. We hope to extend the simulations of Chapter 2 into these early stages to try to reproduce the behavior of the PNs' radii, masses and surface brightnesses at early stages.

As further tests of this new distance method we need to examine additional samples of PNs. We perform an analysis in Chapter 5 to determine how consistent the distances predicted by this method are with the kinematics of Galactic rotation in an extension of the work of Schneider & Terzian (1983). It is also important to test the method against accurate new independent distance determinations, many of which are now becoming available through expansion and parallax studies. And finally, while the method appears to demonstrate good accuracy, it may ultimately be possible to obtain an even better estimator of PN distances by including other distance-independent observables in the analysis besides the surface brightness.

Chapter 4

Radio Continuum Observations of Planetary Nebulae with Faint Optical Halos

4.1 Introduction

As we have discussed in Chapter 2, it is now thought that planetary nebulae (PNs) derive from much higher mass progenitors than had been previously believed based on their Galactic kinematics, scale height, and population statistics, as well as on modeling of the late stages of stellar evolution. It is thought that PNs arise from progenitors averaging several solar masses even though observations indicate that the combined masses of the central star and observed ionized shell of a PN rarely exceeds one solar mass. We suspect that much of this "missing" mass might be accounted for through careful observation of the low surface-brightness halos that surround many PNs.

Our computer simulations in Chapter 2, based on the interacting stellar winds (ISW) model for PN evolution (Kwok, 1982) suggests the reason why there is such a disparity between the observed masses of PNs and the masses of their likely progenitors. In the ISW model, a slow, high mass wind from the asymptotic giant branch (AGB) progenitor star (the "AGB wind") rids the star of most of its outer envelope. The exposed core eventually develops a much lower mass, but high velocity "fast wind" which proceeds to pile-up or "snow-plow" the inner edge of the surrounding remnant AGB wind. Thus, when the central star (the PN nucleus, or PNN) begins to ionize the surrounding material, it has a structure consisting of a fairly high density, snow-plowed inner shell surrounded by a lower density remnant AGB wind.

Our simulations in Chapter 2 indicate that the extent of ionization depends on the interplay between the evolving PNN and the surrounding envelope. The PNN initially increases its temperature at nearly constant luminosity, then decreases its luminosity with only a small decrease in temperature (Schönberner, 1981). The timescale for this evolution is shorter for more massive PNNs, and longer for less massive ones. The density of the inner shell of the envelope depends primarily on the parameters of the interacting winds. Generally, a more massive and slow AGB wind coupled with a very high velocity fast-wind will yield an inner shell with the highest density. The higher density shells are more difficult for the PNNs to ionize completely, since the recombination rate increases as the square of the density. Also, the more massive the central star, the less likely the ionization front is to "punch through" the dense shell since these stars evolve so rapidly that the dense shells have less opportunity to thin out due to expansion.

Thus, there are two distinct possible outcomes to this evolution: (1) PNs which have a relatively high density shell or a low luminosity of ionizing photons will have their ionization fronts confined to the dense shell of the nebula, or (2) PNs with a lower density shell or a high luminosity of ionizing photons will be ionized beyond the dense shell, into the lower density remnant AGB wind. The first case is the scenario in which the PN is classically said to be "ionization bounded." Of primary interest to us in this study, however, is the latter case, where the low density, but high mass surrounding envelope is partially or fully ionized, creating a "halo" of emission around the bright core.

Because the surface brightness of free-free emission depends on the square of the density of ionized material, the dense inner shell can easily outshine the thinner extended halo even though the halo contains much more ionized material. Our simulations show that the PNN has a relatively easy time ionizing the entire halo once the ionization front gets past the dense shell. We also show that the low

surface brightness halos may contain many times the mass of the bright inner core even though they contribute only a small fraction of the total luminosity of the nebula.

Many PNs have been observed to have low surface brightness optical haloes (see Balick *et al.* 1992) but few have been analyzed for ionized mass. Plait and Soker (1990) studied the optical emission from the halo of NGC 6826 and derived a density profile which suggests that the ionized mass of the faint halo is more than two and one half times greater than the brighter inner shell. This is roughly consistent with the upper-limit halo-to-shell mass ratio for NGC 6826 of $\sim$2.2 found by Middlemass, Clegg & Walsh (1989) using long-slit spectroscopic techniques. They calculate this upper limit using line ratios of singly ionized oxygen to find an average electron density, assuming that the halo is uniformly filled (i.e. a filling factor of unity). They also studied another PN halo, NGC 6543, and found that its halo-to-shell mass ratio is *at least* 2.9 and possibly as much as $\sim$10. In a later similar study, Middlemass *et al.* (1991) found the halo mass of NGC 7662 to be roughly comparable to the mass of the dense inner shell.

The terminology regarding the structure of PNs has varied with time and author. Some authors refer to the dense, inner snow-plowed region as the "core", surrounded by a "shell" of rapidly decreasing density with radius. For the purposes of this paper we shall use terminology similar to that of Balick (1989), which we think more accurately describes the features of most typical PNs. The halo is the region thought to be the remains of the AGB wind. Variations in this wind can sometimes lead to distinct inner and outer halos (see Balick, 1989). We shall refer to the "snowplowed" region as the "dense shell" of the PN.

Radio continuum observations of PN halos should prove superior to optical observations for understanding the nature of the emitting medium for three reasons: (1) the free-free radio continuum emission at freqencies of 5 GHz and

higher is optically thin, (Higgs, 1971), except perhaps in very young PNs, (2) the problems of radiative transfer in an expanding medium which are encountered in the interpretation of optical emission line observations can be avoided, and (3) there is no ambiguity with possible reflection nebulosity from dust in the halos. Thus, deep radio continuum profiles should be more easily and accurately deconvolved into PN density profiles.

The dim halos, however, need very long integration times to be detected in the radio continuum. Even more problematic is the wide dynamic range in radio surface brightness expected between the dense shell and halo. Optical surface brightness ratios between the inner shells and outer halos of PNs are typically greater than 100. We expect similarly large ratios for the radio continuum since optical and radio continuum emission processes both scale as the square of the density of ionized gas. Very few of the previous PN observations done at the VLA approach the integration times necessary to detect the low surface brightness of a typical PN halo.

In an attempt to detect and analyze the dim outer halos of PNs in the radio we observed two PNs, NGC 6804 and NGC 6826, known to have optical halos (Balick *et al.* 1992; Plait & Soker 1990; Middlemass, Clegg & Walsh 1989). The VLA D-array was used at a frequency of 8.4 GHz with integration times of about three and a half hours for each PN. Both nebulae were selected to exhibit the optimum combination of size and intensity for the D-array beam size and sensitivity at 8.4 GHz (see § 4.2).

We begin in § 4.2 by presenting the specifics of our observations and data reduction perfomed at the VLA. The observed intensity maps and averaged radial intensity profiles are presented in § 4.3. Also in § 4.3, we attempt to deconvolve the radial electron density profiles of the PN cores and halos. Finally, in § 4.4 we

summarize our results and discuss the implications of our analysis on the ionized mass of these PNs and their possible progenitor masses.

4.2 Observations and Data Reduction

The choice of which VLA sub-array to use for these observations had two conflicting requirements: first, enough resolution was needed in the synthesized beam to distinguish the halo from the PN's inner core, and second, the primary beam must be large enough, and the shortest u–v spacings small enough, to provide good sensitivity over the large angular extent of the faint halo. The wavelength of 3.6 cm (8.4 GHz) was chosen primarly to take advantage of the high sensitivity of the low temperature receivers available. It is also a wavelength where we expect the PNs to be optically thin. There is a slight reduction in intensity at 3.6 cm when compared to 6 cm due to the $\sim \nu^{-0.1}$ dependence of free-free emission, but this should be more than compensated for by the greater sensitivity of the receivers. At 3.6 cm, the D-array has a synthesized beam size of $8''$; significantly smaller than the $\sim 30''$ size of the inner structures of our PNs.

Also of importance is the largest structures visible. The smallest antenna spacings at a given wavelength determine the largest angular sizes of emission features that can be imaged. If the emission feature is larger than the space between the interference fringes for the smallest antenna spacings, then roughly equal amounts of emission will fall on the positive and negative parts of the interference pattern, and the flux will cancel. The largest structures visible at 3.6 cm by the D-array is $3'$, which is larger than the $\sim 2'$ diameter of the largest optical halo (NGC 6826).

NGC 6804 and NGC 6826 were observed on 24 July 1992. The integration times were $\sim$3.5 hours for each source and the observations were made in alternating blocks of $\sim$55 minutes for each source to improve coverage in the u–v

plane. The primary flux calibration source was 3C286. The secondary flux and phase calibration sources, which were chosen on the basis of their strength and proximity to the observed PNs, were 1923+210 for NGC 6804 and 2005+403 for NGC 6826.

The data were flagged for interference, and any phase errors or bad visibilitiy records were removed. The images were initially processed using natural weighting and standard AIPS cleaning algorithms CLEAN and MX. This processing yielded a sufficiently low noise level to detect the inner halo of NGC 6804 but not the expected fainter outer halo of NGC 6826. The main challenge of detecting the halo of NGC 6826 was the large dynamic range. While the inner halo of NGC 6804 needed only a dynamic range of ~200:1 to be detected, we esimated from optical H_β emission (Perek & Kohoutek, 1967) that a dynamic range of greater than 500:1 would be necessary to detect the faintest parts of the halo of NGC 6826. We used self calibration and the AIPS maximum entropy routine VTESS to further reduce the noise arising from imperfect subtraction of the beam's sidelobes. Even though the final cleaned image of NGC 6826 yielded a noise level corresponding to a dynamic range of over 1600:1, no obvious evidence of the faint outer halo was seen in the contour maps.

The final, best cleaned images of NGC 6804 and NGC 6826 are shown in Figures 4.1 and 4.2. NGC 6804 has a distinct inner halo beginning at a radius of ~18" to ~20". The halo of NGC 6826 is not as well defined, but seems to begin at a radius of ~13". The expected noise level for a ~3.5 hour integration at 3.6 cm is $\sim 10^{-5}$ Jy/beam. The rms noise levels in the images are of the same order as that expected: 3.26×10^{-5} Jy/beam for NGC 6804 and 4.05×10^{-5} Jy/beam for NGC 6826. The inner halo of NGC 6804 is obvious in Figure 4.1, but the very faint wisps of optical emission beyond ~40 " radius which Balick, *et al.*(1992) call

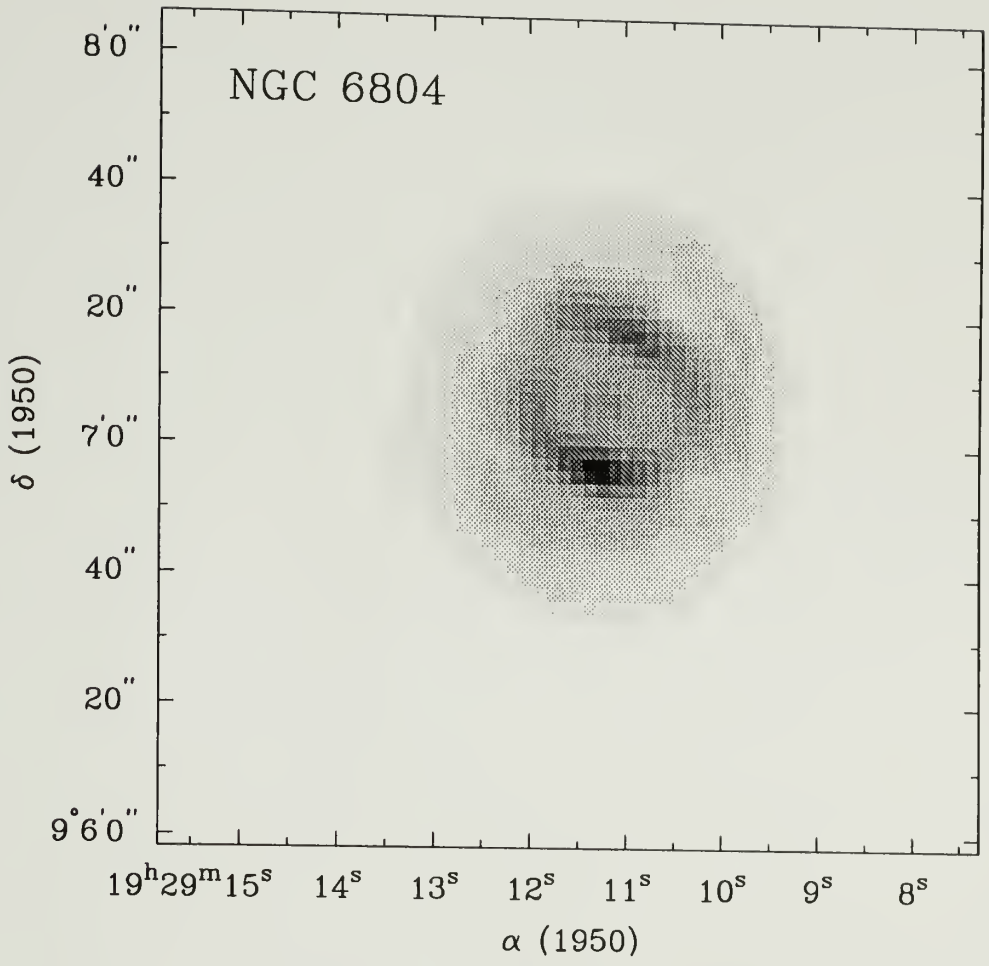

Figure 4.1. Final cleaned radio continuum image of NGC 6804 at 8.4 GHz. Compare this to the deep optical CCD image in Balick *et al.* (1992). Note the bright inner shell surrounded by the lower surface brightness inner halo.

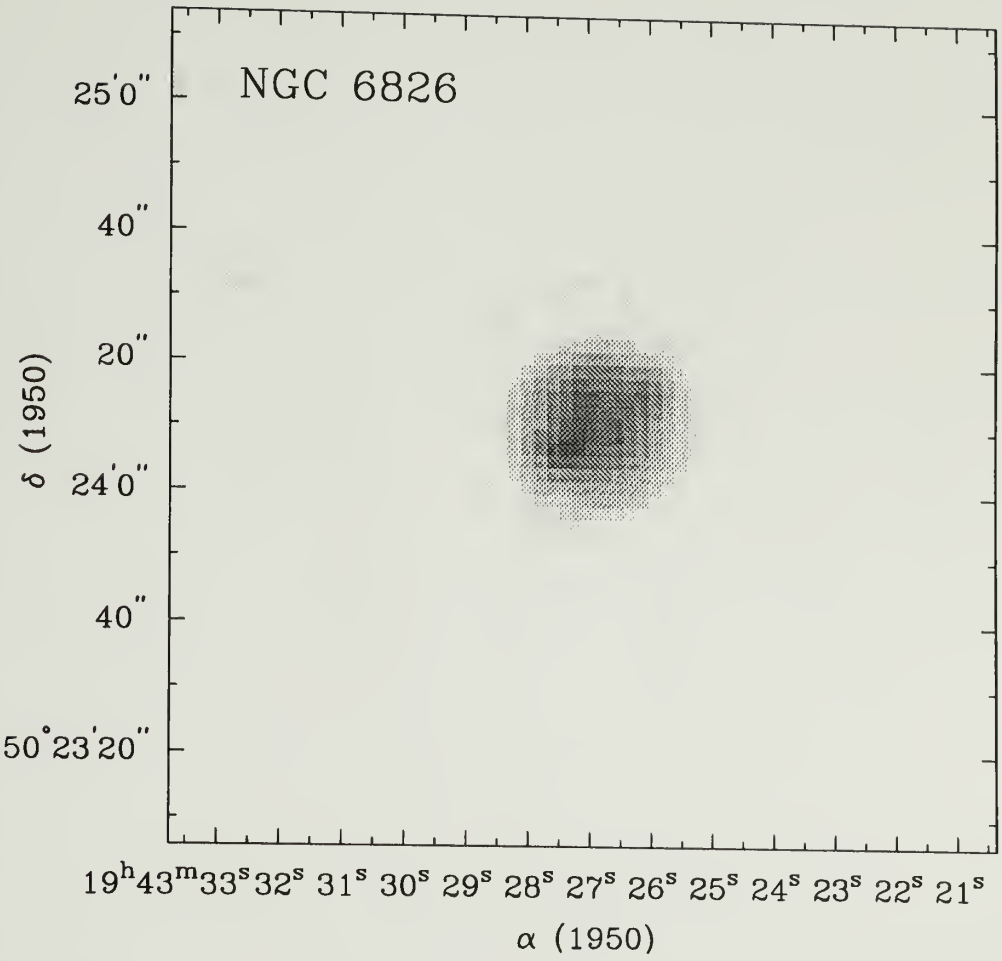

Figure 4.2. Final cleaned radio continuum image of NGC 6826 at 8.4 GHz. From optical images, Plait & Soker (1990) define the halo as the region beyond r = 13 ″. We detect emission well beyond that radius (as can be more easily seen in Figure 4.4), although the faint emission out to ~62 ″ seen in optical images (Balick *et al.* 1992) is not visible here.

flocculi, are not visible. Also, most of the faint extended halo of NGC 6826 seen in optical images (see Balick, *et al.* 1992) is not visible in Figure 4.2.

To construct a radial intensity profile, as well as to additionally enhance the signal-to-noise ratio by averaging over many pixels, the azimuthal average of both PNs' intensity distrubution was calculated. The image, however, was found to still contain systematic negative fluxes that needed to be removed by fitting a baseline to our radial profile. These negative fluxes were in the shape of a characteristic "bowl shaped depression" in the image which is is an artifact of the image processing routines caused by inaccuracies in the zero-spacing flux estimation. The minimum antenna separation causes a central "hole" in the u–v plane which is due to a lack of information about the flux over the largest size scales. The image processing routines attempt to "fill-in" this hole by interpolating the flux at the 0-0 position in the u–v plane, but underestimation of this flux often results in an image that is slightly depressed at the center relative to the edges. To correct for this we fit a baseline in the shape of a 4.09′ FWHM gaussian. This should approximate the characteristic shape of the missing flux since it has an angular extent corresponding to the fourier transform of the "hole" in the u–v plane. The absolute level of our baseline, although somewhat uncertain, was chosen so that the flux was not negative within the noise limits. The noise profile was estimated by multiplying the rms noise for each image by the primary beam shape and dividing by the square root of the number of beam areas used in each azimuthal average.

The final radial intensity profiles, with the baseline subtracted, are shown in Figures 4.3 and 4.4. The peak intensity for NGC 6826 is about an order of magnitude larger than that of NGC 6804, and this is a major reason why the dynamic range necessary to detect the faint halo of NGC 6826 was so large. The estimated noise level for the outer region is plotted as a dotted line with the same magnified vertical scale as the observed intensity for the dim outer regions.

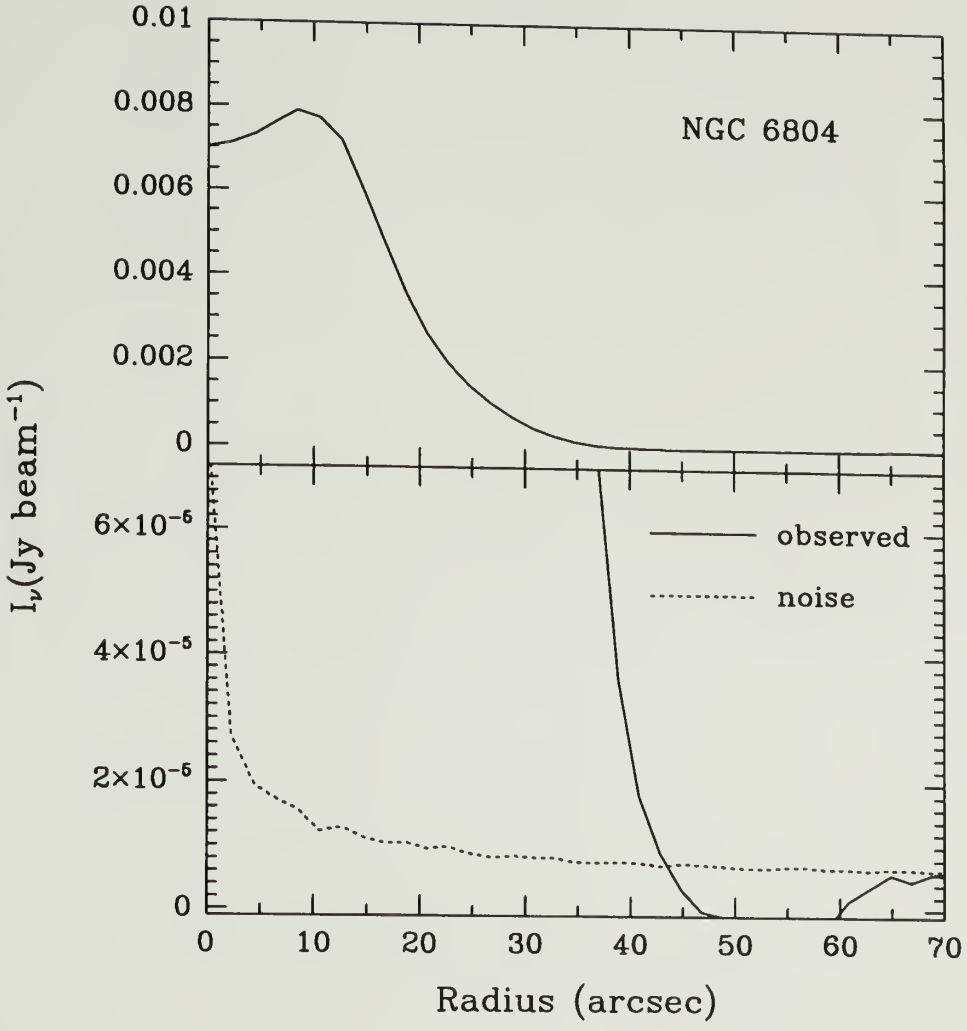

Figure 4.3. Azimuthally averaged radio continuum intensity profile at 8.4 GHz and estimated noise for NGC 6804.

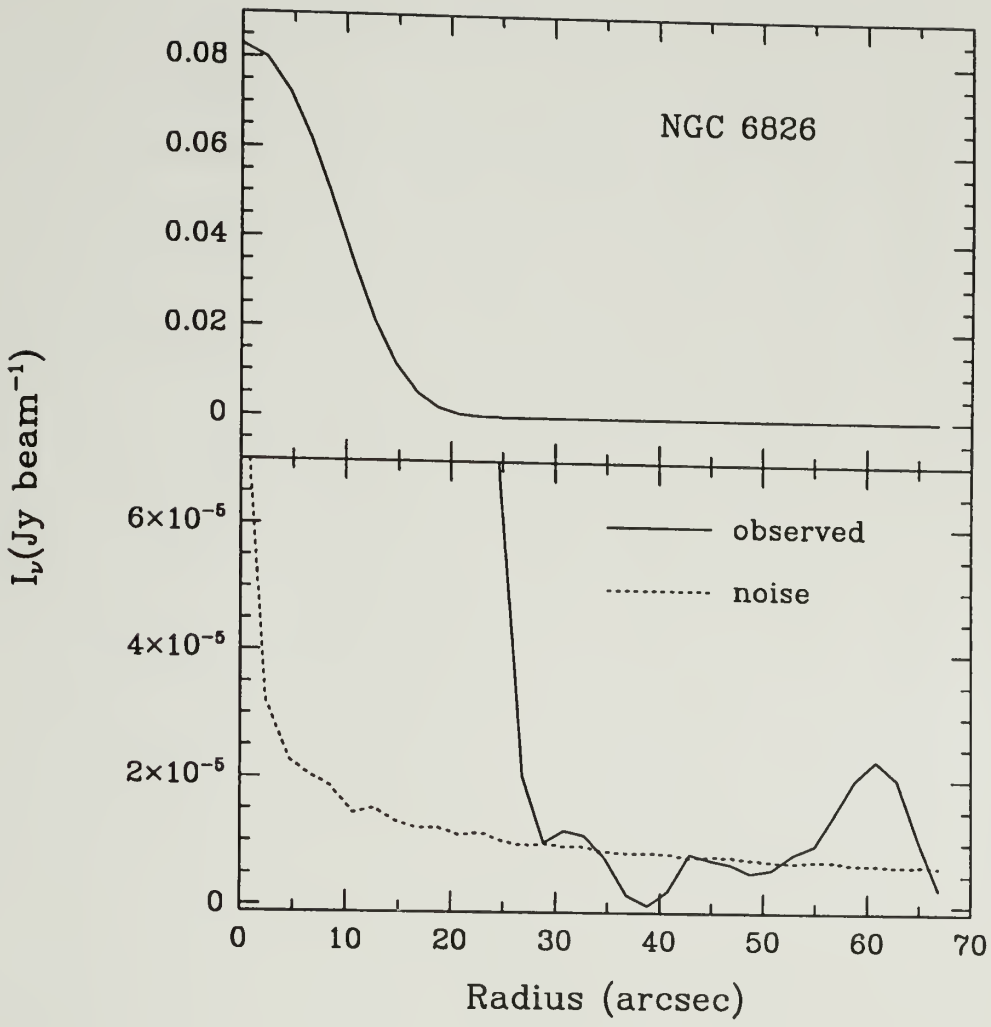

Figure 4.4. Azimuthally averaged radio continuum intensity profile at 8.4 GHz and estimated noise for NGC 6826. Note the larger dynamic range than NGC 6804 and the "bump" at a radius of ~60 ″, corresponding to the limb brightened ring seen in optical images.

Because the baseline we chose for our observed intensity profile was somewhat arbitrary, it is difficult to determine how the level of radio continuum emission in the outer reaches compares with the estimated noise level. This small uncertainty in the baseline does not have any appreciable effect on our analysis of the inner halo or shell, however, since the intensities there are two to three orders of magnitude higher than the baseline or noise.

4.3 Interpretation of the Observations

4.3.1 NGC 6804

An approximate radial density profile of ionized material in NGC 6804 was ultimately obtained by numerically calculating the free-free intensity profiles of spherically symmetric trial density distributions and comparing these to the observed azimuthally averaged intensity profile. To begin the process, a base electron density profile was constructed by assuming a uniform density core and a power law density profile for the inner halo. A rough initial estimate of the electron density of the core was made using a relation derived from Milne & Aller (1975) scaled to 8.4 GHz and (for this rough estimate only) assuming pure hydrogen:

$$n_e \approx (511)\frac{S_{8.4GHz}^{1/2} T_e^{1/4}}{\theta^{3/2} d^{1/2} \epsilon^{1/2}} \tag{4.1}$$

where θ is the angular radius in arcseconds, T is the electron temperature (assumed to be $\sim 10^4$ K), d is the distance in kpc, ϵ is the filling factor, and $S_{8.4GHz}$ is the flux density in mJy.

Various power laws of radius were tried for the halo density until the resultant "trial" intensity profile was reasonably close in shape and total emission to the observed profile. This base density profile was then attenuated iteratively from the edge of the visible halo inward until the observed and modeled intensity profiles converged. This procedure was carried out for two ionization cases: (1) all of the

emission is a result of H II and He II, or (2) there is additional continuum emission due to He III. For NGC 6804, spectroscopic observations suggest a significant ammount of He III, with a derived He III to H II ratio of 0.071 (Kaler 1970). Exactly how far into the PN the He III ionization front extends is impossible to tell from our observations. If all the helium is doubly ionized, then a lower electron density and a smaller total mass is needed to account for the observed emission. Since our mass results, of course, are distance dependent, it was important to establish the distance to NGC 6804. The *Strasbourg–ESO Catalog* quotes two values for the distance to NGC 6804: 2 kpc and 1.09 kpc. The distance derived from our radius – surface brightness method in Chapter 3 is 1.46 kpc. We use the value 1.46 kpc as reasonable distance estimate to NGC 6804. The electron density profile for NGC 6804 at d = 1.46 kpc is shown in Figure 4.5. We integrated this density profile for the dense shell ($\theta < 20''$) and the halo ($\theta > 20''$) to obtain the masses. The ratio of the halo mass to the shell mass (which is independent of distance) is approximately 2.1:1. The mass results for a distance of 1.46 kpc and both ionization scenarios are given in Table 4.1. Column 1 gives the PN name. Column 2 lists the ionized species used in the derivation of electron density. Column 3 lists the derived shell masses, while the derived halo masses are listed in Column 4. The distance independent halo-to-shell mass ratios are given in Column 5.

There is a concern, of course, that the convolution of the PN's true intensity distribution with the synthesized beam might "smear" some of the emission from the shell into the halo, leading to an overestimate of the halo mass, and an underestimate of the shell mass. Although the true deconvolved intensity profile of the PN cannot be uniquely determined, we can get an example of a deconvolved intensity profile by dividing the fourier transform of the observed intensity profile by the fourier tranform of the beam. This provides us with an estimate of the amount of emission that might be "smeared" into the halo region. The

deconvolved intensity profile does, in fact, have slightly more emission in the shell and less in the halo than the observed profile.

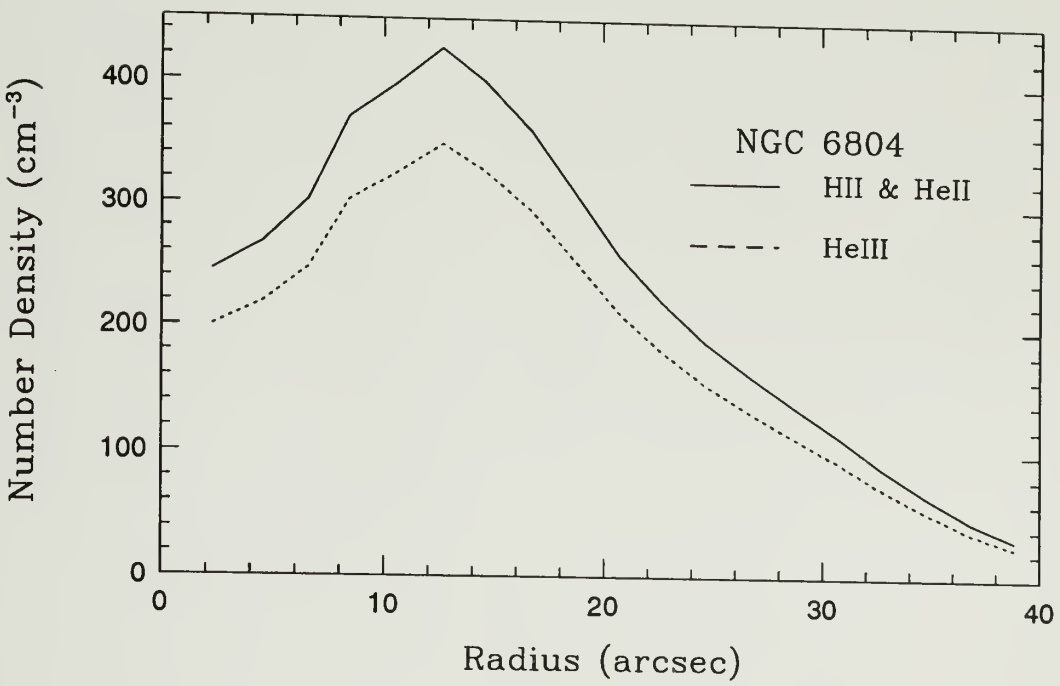

Figure 4.5. The derived electron density profile of NGC 6804 corresponding to the observed intensity profile with and without doubly ionized helium.

TABLE 4.1
DERIVED SHELL AND HALO MASSES

PN (1)	Ionization (2)	M_{Shell} ($M_\odot$) (3)	M_{Halo} ($M_\odot$) (4)	$\frac{M_{Halo}}{M_{Shell}}$ (5)
NGC 6804	(H II & He II)	0.136	0..29	2.1
	(+ He III)	0.101	0.21	2.1
NGC 6826	(H II & He II)	0.168	0.23[a]	1.4
			0.34[b]	2.0
			0.44[c]	2.6
	(+ He III)	0.125	0.17[a]	1.4
			0.25[b]	2.0
			0.32[c]	2.6

[a]lower limit (inner halo out to ~27")

[b]lower limit plus limb brightened halo at ~62"

[c]upper limit (assumes emission = noise between inner and outer halos)

However, the masses we derive from the deconvolved intensity profile of NGC 6804 differs by only a few percent from the masses derived from the observed profile. Clearly, the smearing due to the beam does not introduce large errors into our mass ratio determination for the nebulae.

4.3.2 NGC 6826

Plait and Soker (1990) define the halo of NGC 6826 to begin at an angular radius of 13 ″ from the center of the nebula. Clearly, our radially averaged intensity profiles show emission out to a radius of ∼27 ″. Notice also the small bump in the magnified intensity profile of NGC 6826 at a radius of ∼62 ″. Although this elevated emission is too close to the calculated noise level to be considered a clear detection, it is at the same radius as the limb-brightened edge of the outer halo seen in optical images. We will discuss this feature further below.

To obtain an approximate density profile for NGC 6826 we used a similar method as was used for NGC 6804, but with one major difference. For the initial base density profile we used the electron density profile of NGC 6826 determined optically by Plait and Soker (1990) and adopted their distance to the nebula: 1.54 kpc. Our distance estimate for NGC 6826 using our method in Chapter 3 is 1.46 kpc; but since it is within the uncertainty in our distance method, we will use 1.54 kpc to facilitate comparisons with the results of Plait & Soker. Figure 4.6 shows that this initial density profile yields an intensity distribution which is much too low in the inner core of the nebula, but matches the "bump" corresponding to the limb brightened edge of the outer halo reasonably well.

Figure 4.7 shows our derived electron density profiles with and without the contribution of doubly ionized helium as compared to the density profile of Plait & Soker (1990). If all the helium in the PN is doubly ionized, it would have an electron density profile quite similar to that of Plait & Soker in the inner regions.

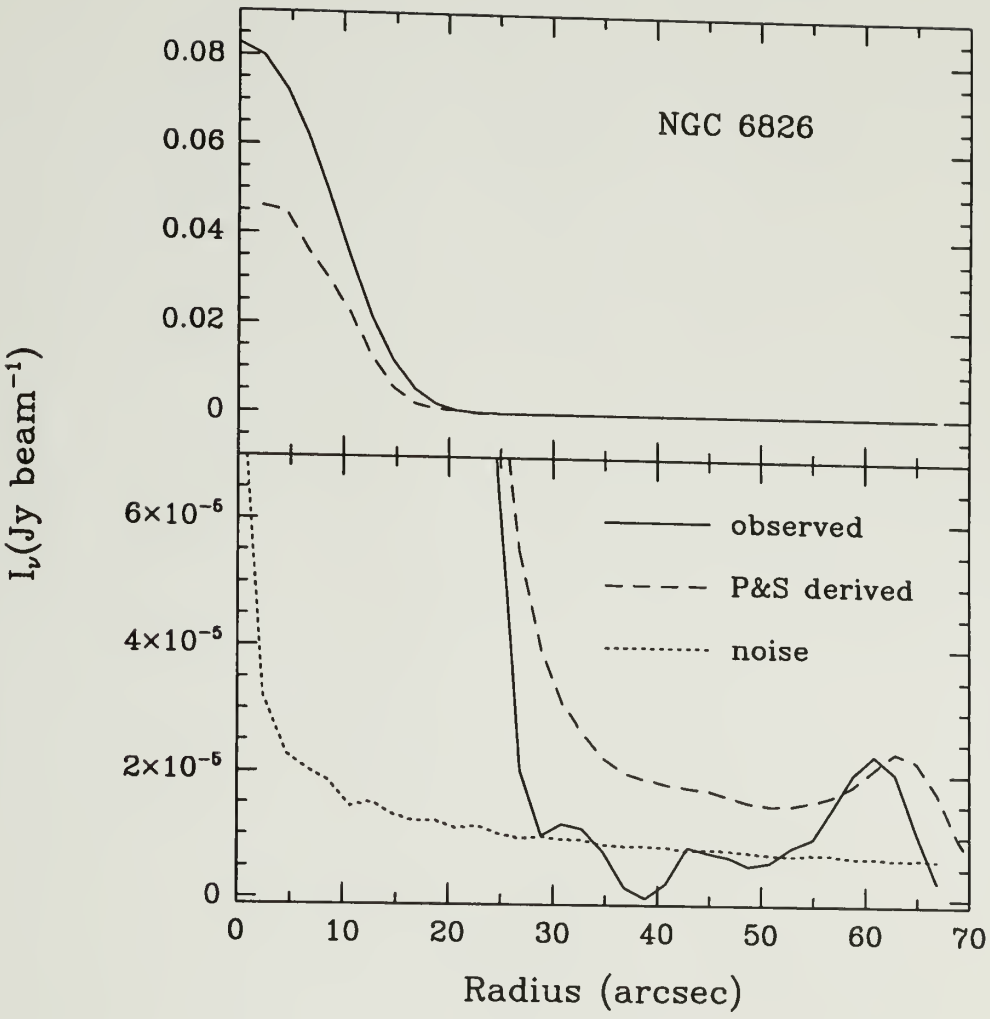

Figure 4.6. Comparison of the observed radio continuum intensity profile to the intensity profile predicted by the electron distribution of Plait & Soker (1990) assuming singly ionized helium.

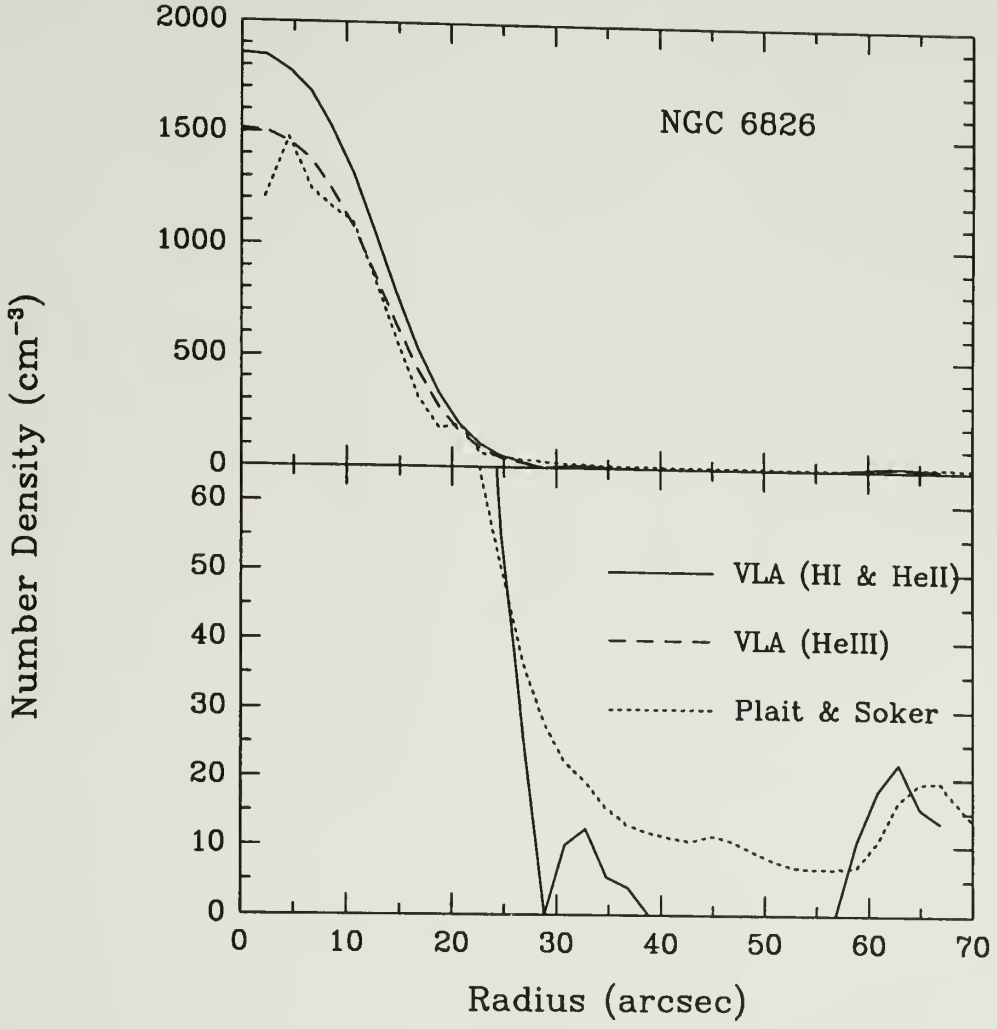

Figure 4.7. The derived electron density profile of NGC 6826 corresponding to the observed intensity profile with and without doubly ionized helium. The electron density profile of Plait & Soker (1990) (which was derived assuming singly ionized helium) is included for comparison.

However, because Plait & Soker assume the helium in the nebula to be only singly ionized throughout, they calculate an inner shell mass of $\sim$0.15 $M_{\odot}$, whereas our He III profile yields an inner shell mass of only $\sim$0.125 $M_{\odot}$. Spectroscopic studies (see Manchado & Potasch, 1989) suggest that NGC 6826 is nearly devoid of He III. If this is so, then the electron profile corresponding to our observed radio continuum distribution must have a significantly higher density in the central region than Plait & Soker's profile. However, because this inner region comprises such a small volume, the inner shell mass of our derived profile contains only a slightly higher mass than Plait & Soker's profile: $\sim$.168 $M_{\odot}$ to $\sim$.15 $M_{\odot}$ respectively (using 13 $''$ as the cutoff radius for the dense shell as explained above).

The halo mass of NGC 6826 was estimated by several methods. The numerical results of these estimates are also tabulated in Table 4.1. The first method, which we dub the "lower limit," integrates only the mass between the radius where the halo begins ($\sim$13 $''$) to the radius where the signal first becomes comparable to the noise level ($\sim$27 $''$). If we assume singly ionized helium this yields a mass of $\sim$0.23 $M_{\odot}$, or just over 1.4 times the mass of the inner shell. The second method includes the mass necessary to account for the barely detected limb brightened ring at $\sim$62 $''$ but assumes that the density drops to zero at any radius where the signal drops below the noise. This method (lower limit plus ring) yields a halo mass of $\sim$0.34 $M_{\odot}$, or $\sim$2.0 times the mass of the inner shell. To calculate an upper limit to the possible halo mass, we assumed that the emission was equal to the noise for radii where the signal dropped below the noise (between $\sim$27 $''$ and $\sim$56 $''$). This yielded a halo mass of $\sim$0.44 $M_{\odot}$, which is 2.6 times more massive than the inner shell. The assumption that He III is present merely reduces the absolute mass of both the core and halo, but would not change the ratio of the masses. For comparison, Plait & Soker (1990) derive a core mass of $\sim$0.15 $M_{\odot}$ and a halo mass of $\sim$0.39 $M_{\odot}$ for a halo to core ratio of $\sim$2.6, similar to our upper limit.

Deconvolution of the observed intensity profile with the synthesized beam again resulted in a profile with emission more highly concentrated in the inner shell. The mass distribution corresponding to this deconvolved intensity profile had a less than 4% increase in the shell mass and a less than 7% decrease in the upper limit halo mass. So the "smearing" of emission due to the beam seems to have little effect on our mass estimates of the shell and halo of either PN.

4.4 Discussion

The inner halo of NGC 6804 is best modeled with a density profile that goes roughly as radius to the -3.2 power. This is a much steeper decline than one would expect if the material in the inner halo were produced by a steady, uniform mass-loss wind – which would result in an inverse square density profile. This seems to indicate that the massive stellar wind from the AGB stage of the star's evolution does indeed vary over time. A wind with an increasing mass loss rate and constant velocity would certainly create a remnant envelope with a steeper than r^{-2} decline. A uniform-velocity wind which has a mass loss rate increasing linearly with time, for example, should yield an envelope with a r^{-3} distribution. What is not so clear, at least qualitatively, is what effect a variation in the AGB wind speed would have on the density distribution in the remnant AGB wind. If wind velocity were to increase with time, one would expect a general "bunching up" of previously ejected slow-moving material as the faster moving material overtakes it, and adds both mass and momentum to the remnant envelope. The effect would be similar to the interacting stellar winds model described in § 4.1, but with the impinging wind being much slower than the fastwind in the ISW model. If, on the other hand, the wind velocity suddenly slows, one could imagine a "gap" developing where the slower wind material cannot "fill in" the void left behind by the earlier, more rapid wind. The true density distribution resulting

from such variable winds would certainly depend on various hydrodynamic properties such as collisional mean free path, temperature, pressure and sound speed, and would not be as simple as the qualitative picture outlined above. But certainly variations in wind speed would result in density enhancements at certain radii, and density deficits in others. Frank *et al.* (1990) argue that variable winds are responsible for much of the morphological features of PN halos. The structures, such as "detached rings" and non- r^{-2} mass distributions are, they claim, a result of variable mass-loss rates from the AGB star as well as redistribution of matter via hydrodynamic waves. Our relatively poor understanding of the physical mechanisms involved in sustaining AGB stellar winds for an extended period of time prevents us from saying exactly what form these variable winds take.

It is unlikely that the progenitor of NGC 6804 could have kept up this accelerated mass loss rate in the late stages. If we assume that the shell of NGC 6804 is composed of material swept up by the fast wind, at a rate corresponding to the expansion of the dense shell ($\sim$24 km s^{-1} for NGC 6804 – slightly more than twice the presumed velocity of the AGB wind) we can make a rough calculation of the distribution of matter that might have been there before the "snow plowing" commenced. If we integrate a r^{-3} distribution inward to roughly half the radius of the shell ($\sim$10") we obtain a mass of $\sim$0.22 $M_{\odot}$. This is significantly more than the 0.136 $M_{\odot}$ mass of the shell that we observe. If we do the same for a r^{-2} profile, we obtain a mass of $\sim$0.16 $M_{\odot}$, similar to the 0.136 $M_{\odot}$ observed. So the star may have had a steady, or diminishing wind near the end of the AGB wind stage. There is material inward of the 10" radius, but this could be caused by backfilling if the thermal pressure of the dense shell has become large.

The inner halo of NGC 6804 contains more than twice the mass of the dense shell while accounting for only about one quarter of the total radio emission. It is entirely possible that there is more mass beyond the $\sim$40″ radius of the detected

halo that is too low in surface brightness to detect. If we were to assume that the AGB wind lasted for $\sim 10^5$ years at a velocity of 10 km s^{-1}, the edge of the AGB wind would be located at a radius of $\sim$3 pc (an angular radius of $\sim$7 arc minutes). If we integrated a r^{-3} mass distribution from the inner edge of the halo out to such a distance we would obtain a total halo mass of $\sim 0.97\ M_{\odot}$. Still, $\sim$88% of the emission of such a halo would come from within the 40" radius of the observed halo. A r^{-2} distribution integrated to that radius results in a mass of over 6 $M_{\odot}$. However, such a distribution would have almost 50

Our observations show that the halo of NGC 6826 contains at least 1.4 times, and possibly up to 2.6 times, the mass of the inner shell, while contributing only $\sim$24% of the nebula's total radio flux. The inner halo of NGC 6826 (from $\sim$14 " to $\sim$26 ") is best modeled with a density profile that goes (very) roughly as the radius to the -5 power. This implies even a greater increase in mass loss rate of the AGB wind (assuming a constant velocity), or a greater buching up of winds with a velocity gradient than in the case of NGC 6804. We speculate that the dearth of halo material between $\sim$28" and $\sim$52" might be caused by a wind with a mass loss rate increasing linearly with time, as NCG 6804 may have done, but with a wind speed that is accelerating over time. Perhaps the "detached" ring is merely bunched up material from an accelerating wind catching up with slower material. And perhaps the r^{-5} inner halo is merely the material "left behind" once the wind speed again diminished. If we integrate a r^{-3} profile (scaled using the density at $\sim$13") that would be produced by a non-accelerating (but increasing mass-loss) AGB wind from the inner edge of the halo ($\sim$13") out to beyound the ring ($\sim$70") we obtain a mass of $\sim 0.4\ M_{\odot}$. This is consistent with our upper limit to the halo mass of NGC 6826. (Integration of a r^{-2} profile over the same range yields a mass much higher than even our upper limit – $\sim 1.2\ M_{\odot}$.) So maybe it is the velocities rather than the mass loss histories that account for the difference in

the structure of the two halos. Frank *et al.* (1992) have modeled the halo of NGC 6826 with two episodes of enhanced mass loss "superwinds" during the AGB stage. Their model mirrors the structure of the halo of NGC 6826 quite well. They conclude that there must be more remnant AGB wind material beyond the outer ring to provide enough pressure to confine the ring material. Plait & Soker (1990), on the contrary, contend that it is the collision of the halo material with the interstellar medium (ISM) that produces the limb brightened ring. It is unlikely that the ISM could be responsible for this ring as well as other symmetric PN halo structures observed because the PN population as a whole has a fairly large velocity dispersion, on the order of $\sim$30 km s^{-1}, relative to the Galactic ISM. Motions of this magnitude through the ISM would certainly not produce symmetrical halos like that seen around NGC 6826.

The shell of NGC 6826 does not appear to have a central "hole". Also, its expansion velocity, tabulated as 11 km s^{-1} in the *Strasbourg–ESO Catalog*, is closer to the velocity we would expect of the halo material rather than a "snowplowed" shell (like NGC 6804, which has an expansion speed of $\sim$24 km s^{-1}). Perhaps this PN has not been acted on by a fast wind. We can examine whether the mass of the inner regions of NGC 6826 is consistent with a steady, increasing or decreasing mass loss wind. The density and velocity of ionized material at the inner edge of the halo implies a mass loss rate from the AGB star of $\sim 3 \times 10^{-}5$ $M_{\odot}$/yr. The expansion velocity and radius of this material suggests an age of $\sim$7500 years since its ejection. If such a mass loss rate were to continue for that amount of time it would produce an inner region with a mass of $\sim$0.23 $M_{\odot}$— roughly one third larger than the mass we deduce from our observations. Perhaps the mass loss rate of the AGB star had diminished slightly over time.

Although we have found additional mass in the halos of these two PNs, we have not resolved the problem of high progenitor masses and low nebular masses

described in Chapters 1 and 2. Keeping in mind that our derived masses are strongly dependent on our distance estimates, we have found total PN masses for these two nebulae of only slightly more than 1 $M_{\odot}$ (assuming central star masses of 0.6 $M_{\odot}$ for each). On the other hand, if more mass indeed exists beyond the halos, it may be nearly impossible to detect. One possibility of finding large, thin remnant AGB envelopes surrounding PN halos is by looking for dust. Since these dust grains are heated by the central stars of PNs, their temperature decreases with distance from the PNN. This diminishing temperature with distance may make the dust from the early stages of AGB mass loss almost as difficult to detect as the gaseous material. But it is a possibility worth investigating.

The distribution of halos with a greater than r^{-2} decline is something that needs to ultimately be addressed in our models in Chapter 2. One would qualitatively expect that a fast wind encountering a r^{-3} distribution would take longer to initially accelerate the shell since it encounters a greater bulk of material near the star. One would also think that the shell might accelerate out through the radially diminishing envelope since it encounters less and less as it moves out. But perhaps the amount of momentum being provided by the fast wind also changes. Yet we have shown in Chapters 2 and 3 that our model PNs agree quite well with the empirical properties of PNs with independent distances. Clearly, this is an area in need of further study. Careful observation and analysis of PN halos like that done by Plait & Soker (1990), Frank *et al.* (1992) and in this Chapter needs to be done for a great many more PNs than those done so far.

We have also tried to explore the viability of using radio synthesis imaging to study PN halos. We have obtained results which are in good general agreement with optical results of Plait & Soker (1990). We obtain a somewhat higher density of material in the inner shell of NGC 6826, although our derived shell mass is only 12% higher. Perhaps this discrepancy is caused by optical scattering or absorption.

Radio observations may be preferable for exploring the dense, inner regions of PNs. In the faint halos, however, optical analysis seems to be the clear winner. The low surface brightness levels and large dynamic ranges of the PN halos make radio synthesis detection uncertain and the data reduction and analysis extremely difficult.

4.5 Summary

Our observations and analyses of these two PNs have shown them to be similar in two important respects. First, their halos contain the majority of the PN's total ionized mass. Second, the high mass halo contributes less than a quarter of the total radio continuum emission. Yet they differ greatly in the way that their mass is distrubuted. NGC 6804 has a distinct inner dense shell with a hole in the middle surrounded by a gradually declining inner halo. NGC 6826 has no detectable central hole, a very steeply declining inner halo surrounded by an outer ring.

The mass distribution of both halos are much steeper than the r^{-2} distribution expected for a constant velocity, steady mass loss AGB wind. This suggests that the mass loss during the AGB wind stage varies in either mass loss rate, velocity or both. The steep declines in density also show that using a uniform density approximation, which works reasonably well for the dense shells of PNs, is completely inappropriate for finding PN halo masses.

Chapter 5

The Galactic Rotation Curve and Planetary Nebula Distances

5.1 Introduction

As we saw in Chapter 3, one of the main difficulties in assessing the validity of a statistical distance method for planetary nebulae is finding a relatively reliable, unbiased set of independent distance measurements against which to test the method. In Chapter 3, we used a sample of Galactic bulge PNs as well as a local sample of PNs with independent distances determined by Gathier (1987) to help derive and statistically test our new radius vs. radio surface brightness distance method. We show that the distances determined by this method ought to be good to within ~25%. In this Chapter, we test our distance method by comparison with Galactic kinematics. We also explore the kinematic behavior of the PN population and examine the implications on PN evolution. We use a sample of PNs with well known radio fluxes, known radial velocities, and diameters measured from VLA radio continuum contour maps and use our radius vs. radio surface brightness distance method to fit the PNs to the Galactic rotation curve.

The rotation of our Galaxy rises sharply from the core and reaches a relatively flat plateau at a radius of ~35% of the solar distance (see Mihalas & Binney 1981). The Galactic rotation curve within the solar circle is usually determined by 21 cm studies of H I and doppler shifts of CO spectral lines from molecular clouds. Most of the objects in the Galactic disk follow more or less circular orbits about the Galactic center. Disk stars often deviate from the general circular orbital motion of the Galactic disk. Furthermore, older stars often have a larger average

deviation or *velocity dispersion* from the general Galactic rotation than young stars. In general, the older a population of stars, the more its average kinematic behavior will deviate from the average Galactic rotation curve. The dispersion is caused by a star's gravitational interactions with molecular clouds and, to a lesser degree, with other stars in the Galactic disk during their stellar lifespan. The older the star, the larger the deviation from the general Galactic rotation that it is likely to have. Still, knowledge of the Galactic rotation curve and an object's radial velocity, coupled with some rudimentary trigonometry can be used to estimate its "kinematic" distance to within the uncertainties introduced by the velocity dispersion.

Planetary nebulae in the Galactic disk are highly evolved objects since they are derived from the red giant stage of stellar evolution. However, they are probably derived from progenitor stars with a wide range of masses. Thus, a PN from higher mass progenitor with a shorter lifetime will be more likely to match the general Galactic rotation than a PN from a longer lived, lower mass progenitor. We expect the most extreme deviations in velocities mainly in the Galactic bulge population of PNs, which presumably are derived from older and even lower mass Population II stars. For the most part we expect that the disk population's mean kinematic behavior follows the overall dynamics of the Galactic disk to within a range of velocity dispersions depending on their ages and dynamical history.

We begin in § 5.2 by describing the elements of our kinematic analysis of a sample of Galactic PNs. We describe the data set and measurements used to deduce PN distances along with the results of our analysis. A discussion and summary follows in § 5.3.

5.2 Kinematic Distance Analysis of Galactic PNs

The radial velocity of an object in the Galactic disk at a known distance d and Galactic latitude l and longitude b can be obtained by simple geometry if the Galactic rotation velocity Θ is known at that point. For this analysis we assume that all objects at a given cylindrical radius from the Galactic center will have the same rotational velocity. The radial velocity is given by:

$$v_r = \left[\Theta(R)\left(\frac{R_0}{R}\right) - \Theta_0\right] \sin l \cos b \tag{5.1}$$

where R is the radial distance of the object from the Galactic center projected onto the Galactic plane, and R_0 and Θ_0 are the Galactic radius and the rotational velocity at the solar circle respectively. R is calculated geometrically:

$$R = \sqrt{{R_0}^2 + {d_{proj}}^2 - 2R_0 d_{proj} \cos l} \tag{5.2}$$

where d_{proj} is the distance to the object projected onto the Galactic plane: $d_{proj} = d \cos b$.

We calculate $\Theta(R)$ using a linear fit to the Galactic rotation curve from Fich, Blitz & Stark (1989). We adopt a solar distance of $R_0 = 8.0$ kpc and a rotational velocity of $\Theta_0 = 220$ km s^{-1} for this study. This corresponds to one of the published linear fits and is also close to the distance of $R_0 = 7.8$ kpc used to derive and test our distance method in Chapter 3.

We must also subtract an "asymmetric drift" velocity from $\Theta(R)$, in equation 5.1. The asymmetric drift of a population of stars is an apparent rotational lag of the population which is a secondary effect of the velocity dispersion. It may be regarded as another measure of how far the PNs deviate from circular orbits: At a given radius from the Galactic center, at any given time, the velocity dispersion brings in PNs with both larger and smaller average orbital radii. Since the number of PNs grows larger toward the center of the Galaxy, the

local population of PNs is dominated by PNs with smaller than average orbital radii. These PNs are near the apocenter of their orbits and therefore orbiting slower by conservation of angular momentum. In this study we begin by assuming an asymmetric drift of 15 km s^{-1} for the PN population, which is a commonly quoted value for them and is representative of a fairly old disk population.

The radial velocity versus distance ($v_r - d$) curve corresponding to the galactic rotation will be different for each line of sight (l, b). A sample of such a $v_r - d$ curve for two lines of sight is shown in Figure 5.1, for $l = 45°$ and $l = 135°$. Note that for $|l| < 90°$, the curve is not a single valued function. Objects on opposite sides of the tangent point will have identical line-of-sight velocities. This makes kinematic distances for some objects with $|l| < 90°$ ambiguous. However, no such ambiguity exists for objects with $|l| > 90°$, and a unique kinematic distance can be determined from a measured radial velocity.

A difficulty in our kinematic analysis is that certain PNs have velocities which do not agree at all with the general Galactic rotation. For example (referring again to Figure 5.1) a PN at $l = 45°$ with a velocity greater than 65 km s^{-1} or at $l = 135°$ with a velocity greater than zero cannot be reconciled with the Galaxy's rotation. These PNs, in effect, have radial velocities that would exceed the velocity of disk objects at either the tangent point (for PNs with $|l| < 90°$), or at zero distance (for PNs with $|l| > 90°$). Also, PNs with radial velocities less than –80 km s^{-1} are beyond the range of the Galaxy's measured rotation curve. Such a velocity implies a kinematic distance that would place these PNs at more than twice the Sun's distance from the center of the Galaxy, which is not impossible, but is highly improbable given the rapid decline with radius of the number of PNs (see Chapter 3) We dub these PNs with peculiar radial velocities "extra rotational" since they either exceed the range of radial velocities allowed by Galactic rotation

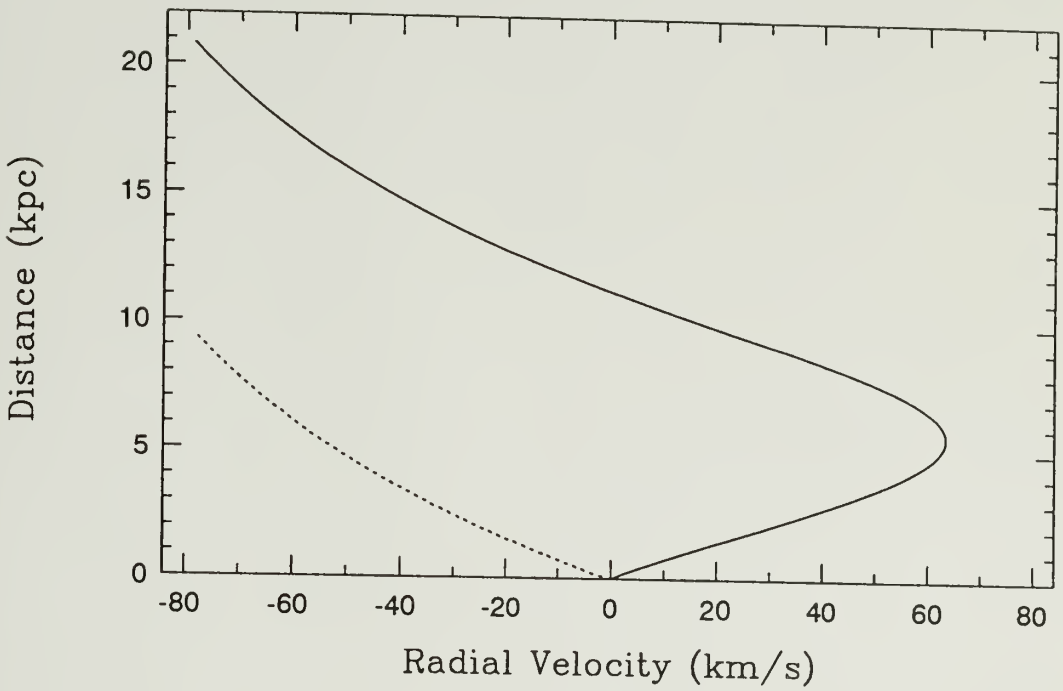

Figure 5.1. Radial velocity versus distance curves for objects in the Galactic disk. The solid line is for an object within the solar circle, l =45°. The dashed curve is for an object outside the solar circle, l =135°.

alone or have velocities beyond the range of the calibrated Galactic rotation curve. We will discuss the implications of these peculiar PNs in § 5.3.

5.2.1 *Kinematic versus Predicted Distances*

We can estimate kinematic distances for PNs with $|l| > 90°$ by fitting them to distance versus radial velocity curves like the one shown in Figure 5.1, but calculated for the specific values of l and b corresponding to each PN. To calculate the kinematic distances, we used the PN radial velocities tabulated by Schneider *et al.* (1983). We can then compare these kinematic distances with distance estimates based on our radius–surface brightness method given in equation 3.4. To avoid confusion, we will call the distances derived from our method the "predicted distances."

The PN radius used in equation 3.4 is the radius of the isophote where the *radio continuum* intensity falls to e^{-1} of the peak emission. These radii were determined by manually measuring published VLA contour maps from Zijlstra *et al.* (1989) and Aaquist & Kwok (1990). The radii were calculated by estimating the location of the e^{-1} isophote and taking the geometric mean of the long and short axes. We then matched as many of the measured PNs as possible to those in the list of radial velocity measurements of Schneider *et al.* (1983). We obtained values of the total 6 cm radio continuum flux density for these PNs from either Milne & Aller (1975), Zijlstra *et al.* (1989), or Aaquist & Kwok (1990).

We began with a primary sample of 123 PNs with measured radio radii, fluxes and radial velocities. To find unique kinematic distances, we needed to restrict our sample to 32 PNs with $|l| > 90°$. Out of this sample, we could only calculate kinematic distances to 20 PNs, and had to reject 12 PNs because their radial velocities were "extra rotational" as discussed above.

We do not, of course, expect our predicted and kinematic distances to agree exactly. Our predicted distances, as we stated in Chapter 3, are probably

uncertain by ~25%. The calculated kinematic distances also have errors, due to both the velocity dispersion of the PN population as a whole, and the uncertainty in the measured radial velocities. The uncertainties in the measured radial velocities were taken from Schneider *et al.* (1983). And to calculate the uncertainty in the kinematic distance it was necessary to estimate the value of the PN velocity dispersion along the line of sight.

The Π, Θ and Z components of the velocity dispersion of the Galactic disk PN population were taken from Mihalas & Binney (1981). They are:

$$\Delta\Pi = 45 \text{ km s}^{-1}, \quad \Delta\Theta = 35 \text{ km s}^{-1} \quad \text{and} \quad \Delta Z = 20 \text{ km s}^{-1} . \tag{5.3}$$

These are locally determined values, but we are assuming that they apply to the Galactic disk PN population as a whole. The radial component of the orbital velocity dispersion is calculated from the projection of the velocity ellipsoid (with the three axes described above) along the line of sight. The contribution of the three components are:

$$\sigma_\Pi = \Delta\Pi \left(\frac{R_0}{R} \cos l - \frac{d}{R} \right) \cos b$$

$$\sigma_\Theta = \Delta\Theta \frac{R_0}{R} \sin l \cos b \tag{5.4}$$

$$\sigma_Z = \Delta Z \cos b$$

and the standard deviation of the velocity dispersion along the line of sight is just the three components calculated above, added in quadrature.

The error in the kinematic distance due to these various velocity uncertainties is estimated empirically for each PN by varying its radial velocity by an amount equal to the expected 1σ uncertainty, and then calculating the resultant variation in the kinematic distance. To test how well the predicted and kinematic distances

agreed, we calculate a reduced χ^2 for our sample of PNs. The reduced χ^2 is the summation of the square of the difference between the predicted and kinematic distances divided by the square of the total standard deviation of the distance uncertainties, divided by the number of objects.

$$\chi^2 = \frac{1}{N_{PN}} \sum \left(\frac{(d_{pred} - d_{kin})^2}{(\Delta d)^2} \right) . \tag{5.5}$$

A reduced χ^2 value of unity in this case means that all the differences between the observed and predicted values can be attributed to the various measurement uncertainties.

Using this procedure and assuming a 1σ uncertainty of 20% for the predicted distances, we obtained a reduced χ^2 value of nearly or less than unity for the 20 PNs with $|l| > 90°$ depending on the value of the assumed asymmetric drift. We varied the asymmetric drift and found that the χ^2 statistic was minimized (0.85) at $v_{asym} = -15$ km s^{-1}. This seems to suggest that the asymmetric drift is the negative of the value we first assumed, which is not physically plausible since a velocity dispersion will always cause a positive asymmetric drift unless the number of PNs increased with Galactic radius. However, it should be noted that the value of χ^2 did not vary much for values of v_{asym} between -20 km s^{-1} (χ^2=0.87) and 5 km s^{-1} (χ^2=0.94). With such a small sample of PNs, such variations may not be statistically significant and an asymmetric drift near zero appears acceptable.

Since our distance method in Chapter 3 was originally tested against an older population of Galactic bulge PNs, it might also be expected that it needs to be scaled by some factor to apply to a presumably younger population of PNs. To test this we scaled our predicted distances by factors ranging between 1.2 and 0.8. The χ^2 statistic was minimized at unity, indicating that our distance method is valid without any additional scaling factor.

5.2.2 *General Fitting to the Galactic Rotation Curve*

To test our distances against a larger sample of PNs, we must approach the question of kinematic consistency from a slightly different direction. Although PNs with $|l| < 90°$ generally cannot have their kinematic distances uniquely determined, it is still possible to calculate the radial velocities of PNs predicted by equation 5.1 using the distance values calculated by our radius–surface brightness method. We can then compare these predicted velocities to the measured radial velocities of the PNs. This method is then applicable to the entire sample of PNs. The extent to which the observed and predicted radial velocities agree or disagree should tell us how well our distance method has placed the PNs on the Galactic rotation curve. As with our direct comparison of predicted and kinematic distances, we do not expect these two radial velocities to agree exactly. The predicted v_r is only good to within the uncertainties due to distance errors and the velocity dispersion of the PN population. And the measured v_r has its associated observational uncertainty. The uncertainty in the predicted radial velocity due to distance measurement errors were estimated empirically. This was done by varying each PN's distance by the expected 1σ distance uncertainty, and calculating the variation of v_r. We again use a reduced χ^2 statistic, this time to measure the agreement between the predicted and observed radial velocities:

$$\chi^2 = \frac{1}{N_{PN}} \sum \left(\frac{(v_r(pred) - v_r(meas))^2}{(\Delta v_r)^2} \right) . \tag{5.6}$$

To reduce the possibility of including bulge population PNs, which generally have peculiar orbits and do not follow the Galaxy's rotation, we eliminated any PNs with $|l| < 10°$. Using the remaining 76 PNs and again assuming a 1σ uncertainty of 20% for the predicted distances, we obtained a reduced χ^2 value of 2.05. This large χ^2 value was mainly due to to several PNs which had exceptionally high individual χ^2 values and could not be brought into line by any means. Most

of these PNs, have "extra rotational" velocities that can not be reconciled with *any* plausible choice of distance (see § 5.2. We found that 33 of the 76 PNs met our criteria for "extra rotational" velocity. This suggests that there is a fairly substantial group of disk PNs whose velocity has a very large dispersion relative to the general Galactic rotation. We will explore this point further in the § 5.3.

After eliminating these 33 "extra rotational" PNs, the remaining 43 PNs analyzed yielded a χ^2 value of 0.98 assuming a 1σ uncertainty of 20% for the predicted distances. The χ^2 statistic was minimized for an asymmetric drift of only 1 km s^{-1} . Again, however, there was a large range of asymmetric drifts between -10 km s^{-1} and 10 km s^{-1} where the value of χ^2 was between 1.01 and 0.98. Such a small variation with such a relatively small sample of PNs does not allow us to determine the actual asymmetric drift with great accuracy, but it suggests it is smaller than the nominal 15 km s^{-1} value. We again tried scaling factors and found that the χ^2 was minimized by scaling our distances by a factor of 0.88. Again, the reduction in χ^2 was minimal and it is uncertain whether this reduction is statistically significant. What is clear, however, is that our distance method is consistent with the 20% error level, within the uncertainties introduced by the disk PNs' velocity dispersion and uncertainties in radial velocities.

5.3 Discussion and Summary

Our analysis shows that our distance method is consistent with galactic kinematics to within the velocity uncertainties and a ~20% distance error. It should be noted, however, that our analysis is dominated by velocity uncertainties. The local velocity dispersion of PNs used in this analysis is so large that the method is not as sensitive to distance dispersion as we would like.

Our distance method was derived and tested using Galactic bulge PNs, most of which, we assume, are derived from Population II stars. One of the more

interesting results of this analysis is the fact that our distance method works well for disk (Population I) PNs with, at most, a minor scaling factor. This suggests that our radius–surface brightness relationship holds regardless of expected differences in envelope mass and chemical composition between the old bulge population and the presumably younger disk population of PNs.

The radius and surface brightness of our PNs is also ultimately linked to the PN mass (see Chapter 3). The success of our radius–surface brightness relationship for PNs derived from low mass as well as higher mass stars then supports observationally our finding in Chapter 2 that the estimated Shklovsky mass for PNs is invariant relative to the mass of the progenitor. In our method as well as Skhlovsky's distance method, we are really only observing the bright inner region of a PN. And the properties of that inner shell seem to be quite independent of any remnant envelope of material that might lie at larger radii.

Another interesting outcome of this investigation is the indication of two separate kinematic populations of PNs. It is obvious that there is a large proportion (40%) of disk PNs that have velocities that are highly dispersed relative to the general Galactic disk rotation. This raises the question of why these PNs are different.

Our first notion was that perhaps the "extra rotational" PNs were derived from older stars. Conversely, the low asymmetric drift of the disk PNs remaining in our sample suggests that they have a small dispersion relative to the Galactic rotation. They are therefore probably derived from a young, high mass population of progenitors. One way of investigating these possibilities is by searching for trends in chemical composition of the rejected and accepted PNs. We attempted to match as many of our PNs as possible to the chemical composition typing of Maciel & Dutra (1992). In Machiel & Dutra's typing scheme, Type I PNs are derived from the most massive (but $< 8\ M_{\odot}$) stars, Type II PNs are derived from less massive

disk stars and Type III are from older, lower mass stars. Unfortunately, we were only able to match about one third of our PNs to those that have been chemically typed by Machiel & Dutra. No clear correlation emerged from this attempt. Because of the small sample, we were unable to draw any conclusions from this.

So what are other possibilities? Perhaps these PNs are derived from "runaway stars" — binary stars in which the companion or PN has lost enough mass rapidly enough that the system has become unbound with positive total energy. Surveys of medium mass stars have shown that the incidence of binarity is ~60% (see Livio 1993), with ~17% in very close binary systems. If the loosely held binaries all became unbound after evolving to the PN stage, this might account for the proportion of PNs with these peculiar velocities.

Perhaps some of the "extra rotational" PNs might be associated with peculiar features in the Galaxy. Those angularly close to the to the Galactic bulge ($10° < |l| < 30°$) could conceivably be part of a nuclear bar. Such a feature would not follow the simple velocity–radius relation of the spiral arms. A study of the spatial structure of the peculiar–velocity PNs could investigate this speculation.

In summary, we have tested our radio radius versus radio surface brightness distance method against Galactic kinematics. We find that, once the PNs with obvious aberrant velocities are eliminated, our distance method agrees with kinematic distances to ~20% to within the errors implied by uncertainties in measured radial velocities and the velocity dispersion of the PN population. We find a large proportion (~40% of our sample PNs are "extra rotational". That is, they have velocities that are out of the range expected by the calibrated Galactic rotation curve. This suggests a separate population of PNs in the disk with relatively large random velocities. Our analysis also showed that the remaining disk PNs exhibited almost no asymmetric drift, suggesting that they have a small

dispersion relative to the Galactic rotation and are therefore probably from a young, high mass population of progenitors.

Chapter 6

Conclusions and Future Prospects

6.1 Current Work and Future Prospects

6.1.1 Young, High Surface Brightness PNs

One of the weaknesses in our PN simulations in Chapter 2 is the failure to produce the small, high surface brightness PNs that are often observed. It has long been assumed that these high surface brightness PNs are very young "growing" nebulae. The failure of our model in this respect is in part due to the uncertainty about the transition that the evolving star makes from the slow AGB wind to the low mass fast wind. In our model, we naively assume that the transition from AGB wind to fast wind is instantaneous. This should have no major effects on our simulated PNs once they age. However, this may effect the early stages of the PN's development significantly. In fact the highest surface brightness simulated PN in Chapter 2 was Model 22 – which had no fast wind at all! Perhaps then a delay in the fast wind "turn on" will produce the small, high surface brightness PNs that have always been assumed to be young.

To test this idea we ran simulations for all three of the PNN masses used in Chapter 2 and using the "standard model" (see Model 1, Chapter 2), but we delayed the onset of the fast wind until the PNN reached a temperature of $\log T = 4.5$ similar to Zhang & Kwok (1993). It is believed that this is the PNN temperature necessary for the resonant line absorption that is responsible for the fast wind to become effective. We expect this scenario to yield higher surface brightnesses since there is more material for ionizing close to the central star in the

early stages. In effect, the central hole caused mostly by the fast wind has not had time to develop. The lower density means that the still relatively cool PNN has an easier time ionizing the surrounding material. This procedure did give PNs with radio surface brightnesses (see Figure 6.1) which were about an order of magnitude larger than our previous highest. Furthermore, as the PNs evolved to lower surface brightnesses and larger radii, they seemed to behave very much like the nebulae with no time delay between winds. These simulated PNs were still, however, about an order of magnitude lower than the highest observed surface brightness PNs.

To attain even more surface brightness we need – more power! In essence, a higher mass PNN that evolves at a higher luminosity and increases its temperature more rapidly (while material is still very close to the PNN). We simulated the evolution of two PNs using central stars of 0.76 $M_{\odot}$ and 0.84 $M_{\odot}$. As Figure 6.1 shows, these models give very high surface brightnesses – beyond the range of any of the observed PNs in Figure 3.3. Such high mass PNNs are relatively rare, but have been measured (see Zhang & Kwok 1993). The high mass PNNs evolve very rapidly. In fact all of the points on Figure 6.1 beyond 100 mJy $arcsec^{-2}$ are for high mass PNNs younger than 500 years old. So there would be a strong selection effect against seeing any PNs with these extreme surface brightnesses.

A third possibility for producing young, high surface brightness PNs is a fast wind delay combined with an AGB wind that is time variable. As we saw in Chapter 4, some PNs have halo densities that are not simple inverse square distributions that we expect from a constant mass loss wind. A steeper than r^{-2} density distribution would probably yield a higher surface brightness before the onset of the fast wind since a larger proportion of the remnant AGB envelope's mass is near the central star. Because our semi-analytical model is only valid for interacting *constant* winds, a r^{-3} could not be followed into the ISW stage.

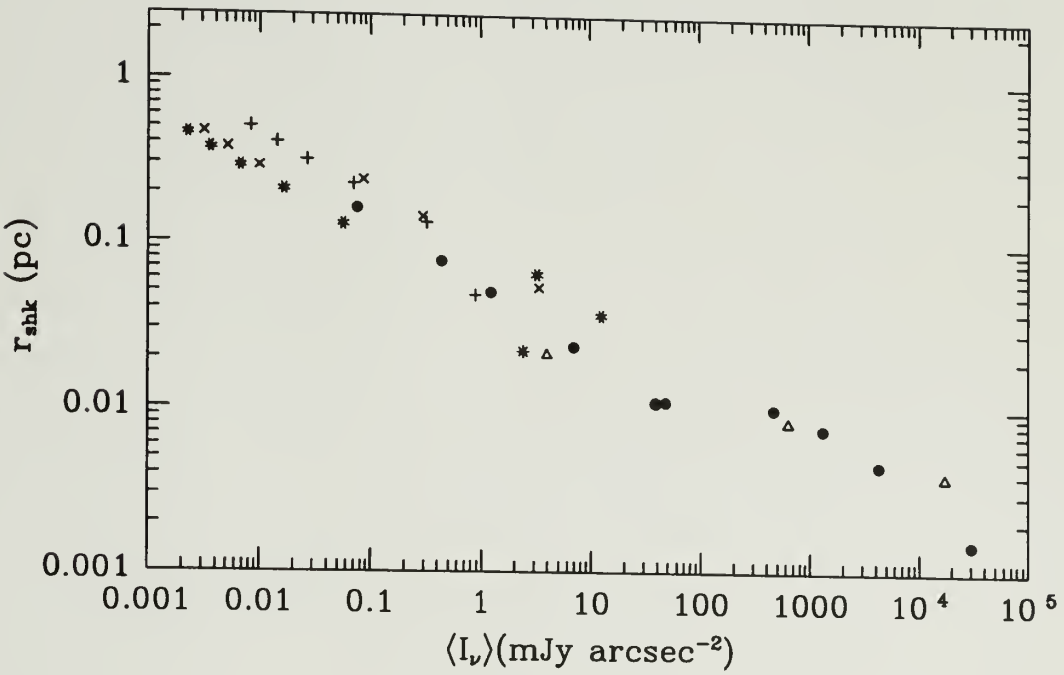

Figure 6.1. The radius–surface brightness relationship of simulated PNs with delayed fast wind. Plotted are PNs with central star masses of (+) 0.565 $M_\odot$, (×) 0.598 $M_\odot$, (*) 0.644 $M_\odot$, (△) 0.76 $M_\odot$, and (o) 0.84 $M_\odot$.

Investigating such a time dependent wind would likely require a time dependent hydrodynamic code.

6.1.2 Systematic Determination of Optical Radii of PNs

As we saw in Chapters 2 and 3, the measurements of angular radii of PNs available in the literature is a jumble of haphazard measurements often from inconsistent and/or very old sources. What is needed is a systematic survey of PNs just for measuring angular radius. The radius should be measured in a comparative way – relative to the peak intensity of the nebula. By using only relative photometry, we avoid difficulties due to interstellar extinction and sky transparency. The definition of the intensity level at the cutoff radius must be well defined, since as we have seen a PNs radius can be very large if one measures out to the edge of a giant halo. And uncertainties in the angular radii must be carefully estimated, since these errors can propagate into any measurement (such as mass or distance) that uses angular radius as an input. Such a survey could be done with modest equipment for numerous relatively large nebulae. A 12 inch f/10 Schmidt-Cassegrain with an ST-6 CCD camera, for example, has a possible resolution of 1". From a sea level site, most often the limiting factor would be atmospheric seeing. Still, even with only 5" seeing, a great number of PNs could be measured.

6.1.3 Where Has All the Mass Gone?

One of the main things that prompted this study was the question of where the PNs might be "hiding" all the mass from their prodigious progenitors. In our simulations, we have shown where the mass *may* be located (in low surface brightness halos), and in Chapter 4 we have shown how difficult it is to detect that mass using radio continuum observations. But we still have not balanced the mass

budget. And as we discussed in § 4.4, the sphericity of outer halos may provide indirect evidence of AGB wind material at large radii from the nebula. This wind material is the likely reason that these limb brightened halos have enough external dynamic pressure to bunch up at the edges. The large velocity dispersion of the PN population and the low density of the interstellar medium at high galactic latitudes make it unlikely that the ISM could cause these common, highly symmetric halos. It may ultimately be impossible to directly detect and measure all the mass lost from the AGB progenitors of PNs if that mass is too thinly spread out in the interstellar medium surrounding the PNs. However, some possibilities still remain.

Many PNs have been found to have neutral atomic and/or molecular envelopes (see Huggins 1992). This material, however, is notoriously difficult to detect at typical PN distances of a few kiloparsecs. For the most part, the molecular envelopes detected in CO have been found to have anywhere from 10^{-3} $M_{\odot}$ to nearly a full solar mass in rare cases. There also seems to be a rough inverse relationship between the radius of ionized gas and the amount of neutral material (see Dinerstein 1991). This suggests that the neutral material is part of the remnant AGB envelope and is progressively dissociated and ionized by the evolving PNN's radiation. However, even in some well evolved PNs like the Helix, molecular envelopes with masses on the same order as the ionized gas persist. Still, however, the most likely strategy for finding large amounts of neutral material would be to investigate relatively near and young PNs. Advancement in this field is closely related to advances in millimeter wave technology. The advent of the Large Millimeter Telescope and the Millimeter Array in the next decade could provide the increase in sensitivity needed to detect a great deal more neutral material in PN envelopes.

Another component of the remnant AGB wind which is more likely to survive the ionization of the nebula is dust. Near infrared observations have shown many

PNs to have dust embedded in their ionized shells. This dust is thought to be heated primarily by Lyman α radiation in the shell. The dust in the outer regions, however, is difficult to detect. The temperature drops with distance from the central star, and, for a hot evolved PNN, most of the star's luminosity is in the ultraviolet and is intercepted and used to keep the gas of the dense shell ionized. Thus, extended dust would probably be easiest to detect in young PNs, where the central star is luminous, but still cool enough that most of its radiation still reaches the outer envelope. In fact, the two PNs observed to have extended far IR dust emission from IRAS images are both young objects (see Preite-Martinez 1989). Close examination of nearby, young PNs in the IRAS data could yield more evidence of extended emission and yield information on the PN's extended envelope mass. A large advancement in these types of observations, however, await the increased resolution of a far IR telescope, as most PNs are below the resolution of IRAS pixels.

6.1.4 Loose Ends

There are several other avenues for investigating the masses and observed radii of PNs. Some of these are:

- Different geometries. Our spherically symmetric model gives a good first order view of PN properties. This could be extended to include more sophisticated 2 or 3 dimensional hydrodynamic models to see how the invariance of the "Shklovsky mass" and our distance method hold up. Such a study would be valuable considering the large number of non-spherically symmetric PNs observed.
- Variable winds. It is commonly thought (see Iben 1992), and our VLA halo observation bear out, that the AGB wind is probably not constant. Also, it is thought that the fast wind varies greatly and is likely liked to the evolution of the central star (Pauldrach *et al.* 1988). Simulating the effects of these varying winds

in a more advanced evolutionary model would be useful in testing the results of our simple model. It might also give us insight into why this fortunate conspiracy that makes the Shklovsky mass vary so consistent happens in the fist place.

- Varying onset of winds. There is evidence that the evolutionary ages of PNNs derived from theory do not always mesh with the dynamical ages of their PNs derived from shell expansion and sizes (see McCarthy *et al.* 1990). This may be due to variations in the transition time for the star to evolve from the AGB stage to the PNN stage. A surprisingly small additional amount of material in the envelope surrounding the core could have a significant effect.
- Additional testing of radius – surface brightness method. As pointed out in Chapter 5, a reliable data set of PNs with independent distances is hard to come by. One such set of PNs is found in the large Magellenic Cloud. Unfortunately, most of these PNs are not resolved. Measuring the radii of the LMC planetaries might be accomplished optically with the Space Telescope. However, radio fluxes are another problem. The small angular sizes make it necessary to obtain radio fluxes via synthesis imaging. Unfortunately, the LMC is, of course, below the horizon for the VLA.

6.2 Summary

We have undertaken a study of the closely related problems of masses and distances of planetary nebulae. In the process we have also looked at the evolution and structure of PNs and have explored their kinematic behavior within the Galaxy as well. We began by simulating the evolution of PNs from relatively high mass ($\sim$3 $M_{\odot}$) progenitors using a simple, spherically symmetric model based on the interacting stellar wind model (Kwok, 1982). We ran simulations using a wide variety of input parameters. We examined the implications of this evolutionary model on observationally derived ionized masses by, in effect, "observing" our

simulated nebulae and measuring their ionized mass using the standard methods. We also performed a statistical analysis of a set of PNs that had their masses determined using a variety of independent distance methods (Gathier 1987). Using this data set of PNs with independent distances and a sample of Galactic bulge PNs along with our simulated nebulae, we derived a semi-empirical relationship between the PNs' *observed* radius and radio surface brightness. This relationship was then used to measure distances to PNs by comparing their physical radius to their observed angular radius. We also explored the performance of the Shklovsky (constant mass) distance method in determining distances to PNs in the galactic bulge. We obtained deep radio synthesis images of two PNs with known optical halos to determine the amount of mass that these halos contained. Finally, we tested our new distance method against the kinematics of Galactic PNs and examined the kinematic behavior of PNs within the Galaxy.

The main conclusions of our work are as follows:

1) The nominal ionized mass that would be derived from observations of our simulated nebulae using the usual methods (the "Shklovsky mass") consistently remains on the order of a few tenths of a solar mass for PNs of moderate age (more than a few thousand years old). This result is quite insensitive to variations in the input parameters of our simulations or the true amount of ionized mass present. Observational mass determination methods generally only measure the bright, high density inner shell of a PN. In many cases, when the ionization front has proceeded beyond the dense shell, the low density halo may potentially contain several solar masses of ionized material but contribute only a small fraction of the nebula's emission due to the strong dependence of that emission on density. Hence, the standard techniques may severely underestimate the ionized mass of PNs by only "seeing" the bright inner shells.

2) Our error analysis of derived masses of PNs with independent distances (Gathier 1987) shows that the intrinsic variability in the PN ionized masses is much smaller than previously believed – only 42% (1σ) in $\log M_i$ – when the propagation of errors in measured input quantities is properly considered. This is consistent with the intrinsic variation of the Shklovsky masses of our simulated PNs. The "fortunate coincidence" that *observed* PN masses seem to invariably lie in a relatively narrow range around a few tenths of a solar mass may explain why the Shklovsky distance method works well despite the errors in its fundamental assumptions of constant, low mass PNs and total ionization.

3) We use a sample of Galactic center PNs to show that the Shklovsky method does indeed work well in predicting distances to relatively large, low surface brightness PNs. However, it overestimates the distances of small, high surface brightness PNs. We also show that the relationship between radius and mass for PNs converges to that which is predicted by the Shklovsky method for highly evolved PNs.

4) We develop a new distance determination method for PNs by deriving a theoretical/empirical relationship between PN radii and radio surface brightness using samples of local, Galactic bulge and simulated PNs. The method uses only easily obtained measurements of radio flux density and angular size as input. We test this method against the best available independent data on PN distances and show that it appears to be accurate to within $\sim$20% (1σ). The relationship that we find between the radius and surface brightness of PNs is in excellent agreement with our simulated nebulae. We find that no simple power law can describe the changing mass and radius of a PN as it ages, however our empirical relationship has a limiting behavior that is almost indistinguishable from the assumption made in Shklovsky's distance method that PNs have a constant ionized mass.

5) We have made deep radio observations at the VLA of two planetary nebulae, NGC 6804 and NGC 6826, to examine the radio continuum emission from their optically-known faint halos. We examine the question of PN halo masses and explore the viability The large dynamic ranges involved make detection extremely difficult. We used long integration times, self-calibration and maximum entropy techniques to achieve a large dynamic range. We detect the inner halos of both nebulae, and marginally detect the outer halo of NGC 6826 at a position and strength consistent with the optical halo. We derive electron density profiles and (distance independent) halo-to-shell mass ratios for both nebulae. In both cases, the halo contains more than ~60% of the total ionized mass while contributing less than about a quarter of the radio continuum emission.

6) We test our new distance method against Galactic kinematics using a sample of PNs with measured radio diameters and fluxes. We remove PNs with peculiar velocities that cannot possibly fit the Galactic rotation from our sample. After these "extra rotational" PNs are rejected, we find that our distance method performs to ~20% accuracy within the errors introduced by the disk PNs' estimated velocity dispersion. We find no significant asymmetric drift in the remaining disk population. The large percentage of rejected PNs in our sample suggests a large population of PNs with non-rotational kinematic behavior.

References

Aaquist, O. B., & Kwok, S. 1990, A&AS, 84, 229

Acker, A., Marcout, J., Ochsenbein, F., Stenholm, B., Tylenda, R., & Schohn, C. 1992, The Strasbourg–ESO Catalogue of Galactic Planetary Nebulae (Munich: European Southern Observatory)

Amnuel, P. R., Guseinov, O. H., Novruzova, H. I., & Rustamov, Yu. S. 1984, ApSS, 107, 19

Balick, B. 1987, AJ, 94, 671

Balick, B. 1989, in IAU Symp. 131, Planetary Nebulae, ed. S. Torres-Peimbert (Dordrecht: Kluwer), 83

Balick, B., Gonzalez, G., Frank, A., & Jacoby, G. 1992, ApJ, 392, 582

Basart, J. P., & Daub, C. T. 1987, ApJ, 317, 412

Bedding, T. R., & Zijlstra, A. A. 1994, A&A, 283, 955

Blöcker, T., & Schönberner, D. 1993, in IAU Symp. 155, Planetary Nebulae, ed. R. Weinberger & A. Acker (Dordrecht: Kluwer) 478

Boffi, F. R., & Stanghellini, L. 1994, A&A, in press

Bryce, M., Meaburn, J., & Walsh, J. R., 1993, in IAU Symp. 155, Planetary Nebulae, ed. R. Weinberger & A. Acker (Dordrecht: Kluwer) 377

Burton, W. B., & Gordon, M. A. 1978, A&A, 63, 7

Cahn, J. H., Kaler, J. B., & Stanghellini, L. 1992, A&AS, 94, 399

Cerruti-Sola, M., & Perinotto, M. 1985, ApJ, 291, 237

Cerruti-Sola, M., & Perinotto, M. 1989, ApJ, 345, 339

Chu, Y.–H., Jacoby, G. H., & Arendt, R. 1987, ApJS, 64, 529

Clegg, R. E. S., Harrington, J. P., Barlow, M. J., & Walsh, J. R. 1987, ApJ, 314, 551

Clemens, D. P., Sanders, D. B., & Scoville, N. Z. 1988, ApJ, 327, 139

Curtis, H. D. 1918, Publ. Lick Obs, 13, 55

Daub, C. T., 1982, ApJ, 260, 612

Dinerstein, H. L., 1991, PASP, 103, 861

Dopita, M. A. & Meatheringham, S. J. 1990, ApJ, 357, 140

Feast, M. W. 1987, in *The Galaxy*, eds. G. Gilmore & B. Craswell (Dordrecht: Reidel), 1

Fich, M., Blitz, L., & Stark, A. A., 1989, ApJ, 342, 272

Frank, A., Balick, B., & Riley, J. 1990, AJ, 100, 1903

Frank, A., Balick, B., Icke, V., & Mellema, G., 1993, ApJL, 404, L25

Gathier, R. 1987, A&AS, 71, 245

Gathier, R., Pottasch, S. R., & Goss, W. M. 1983, A&A,, 127, 320

Gathier, R., Pottasch, S. R., Goss, W. M., & van Gorkom, J. 1983, A&A,, 128, 325

Gurzadyan, G. A. 1969, Planetary Nebulae, (New York: Gordon and Breach)

Heap, S. R., & Augensen, H. J. 1987, ApJ, 313, 268

Higgs, L. A., 1971, Publ. Astrophys. Branch NRC, Canada, 1, 1

Huggins, P. J. 1993, in IAU Symp. 155, Planetary Nebulae, ed. R. Weinberger & A. Acker (Dordrecht: Kluwer) 147

Huggins, P. J. & Healy, A. P. 1986, ApJL, 305, L29

Huggins, P. J. & Healy, A. P. 1989, ApJ, 346, 201

Iben, I. 1993, in IAU Symp. 155, Planetary Nebulae, ed. R. Weinberger & A. Acker (Dordrecht: Kluwer) 587

Isaacman, R. 1984, MNRAS, 208, 399

Jewitt, D. C., Danielson, G. E., & Kupferman, P. N. 1986, ApJ, 302, 727

Johnson, H. M., Balick, B., & Thompson, A. R. 1979, ApJ, 233, 919

Juguet, J. L., Louise, R., Macron, A., & Pascoli, G. 1988, A&A, 205, 267

Kaler, J. B. 1970, ApJ, 160, 887.

Kaler, J. B. 1985, Ann. Rev. of Astron. Astrophys., 23, 89

Khromov, G. S., 1988, Space Sci. Rev., 51, 339

Kohoutek, L., & Martin, W. 1981, A&A, 94, 365

Kwok, S., Purton, C. R. & FitzGerald, P. M. 1978, ApJL, 219, L125

Kwok, S., Purton, C. R. & Keenan, D. W. 1981, ApJ, 250, 232

Kwok, S. 1982, ApJ, 258, 280

Kwok, S. 1985, ApJ, 290, 568

Liller, M. H., & Liller, W. 1968, IAU Symp. 34, Planetary Nebulae, ed. D. E. Osterbrock & C. R. O'Dell (Dordrecht: Reidel), 38

Livio, M. 1993, in IAU Symp. 155, Planetary Nebulae, ed. R. Weinberger & A. Acker (Dordrecht: Kluwer) 478

Maciel, W. J. & Dutra, C. M. 1992, A&A, 262, 271

Mallik, D. C. V. 1985, ApL, 24, 173

Manchado, A., & Pottasch, S. R. 1989, A&A, 222, 219

Masson, C. R. 1989, ApJ, 346, 343

McCarthy, J. K., Mould, J. R., Mendez, R. H., Kudritzki, R. P., Hunsfild, D., Herrero, A., and Groth, H. G. 1990, ApJ, 351, 230

Middlemass, D., Clegg, R. E. S., & Walsh, J. R. 1989, MNRAS, 239, 1.

Middlemass, D., Clegg, R. E. S., Walsh, J. R., & Hetherington, J. P. 1991, MNRAS, 251, 284

Mihalas, D. & Binney, J. 1981, Galactic Astronomy: Structure and Kinematics, (San Francisco: Freeman).

Milne, D. K. 1979, A&AS, 36, 227

Milne, D. K. 1982, MNRAS, 200, 51P

Milne, D. K. & Aller, L. H. 1975, A&A, 38, 183

Milne, D. K. & Aller, L. H. 1982, A&AS, 50, 209

Osterbrock, D. E. 1989, Astrophysics of Gaseous Nebulae and Active Galactic Nuclei, (Mill Valley, California: University Science Books)

Panagia, N., & Walmsley, C. M. 1978, A&A, 70, 411

Pauldrach, A., Puls, J., Kidritzki, R. P., Mendez, R. H. & Heap, S. R. 1988, A&A, 207, 123

Perek, L. & Kohoutek L., 1967, Catalogue of Planetary Nebulae, (Prague: Acadamia Press)

Phillips, J. P., & Mampaso, A. 1988, A&A, 190, 237

Phillips, J. P., & Reay, N. K. 1983, A&A, 117, 33

Plait, P. & Soker, N. 1990, AJ, 99, 1883

Pottasch, S. R. 1984, Planetary Nebulae, (Dordrecht: Reidel)

Pottasch, S. R., Bignelli, C., & Zijlstra, A., 1987, A&AS, 177, L49

Pottasch, S. R., & Zijlstra, A. A. 1992, A&A, 256, 251

Preite-Martinez, A. 1989, in IAU Symp. 131, Planetary Nebulae, ed. S. Torres-Peimbert (Dordrecht: Kluwer), 9

Ratag, M. A., & Pottasch, S. R. 1991, A&AS, 91, 481

Ratag, M. A., Pottasch, S. R., Zijlstra, A. A., & Menzies, J. 1990, A&A, 233, 181

Schmidt-Voigt, M. & Köppen J. 1987, A&AS, 174, 211

Schneider, S. E. & Terzian, Y. 1983, ApJL, 274, L61

Schneider, S. E., Terzian, Y., Purgathofer, A., & Perinotto, M. 1983, ApJS, 52, 399

Schneider, S. E., Silvergate, P. R., Altschuler, D. R. & Giovanardi, C. 1987, ApJ, 314, 572

Schönberner, D. 1981, A&AS, 103, 119

Schönberner, D. 1989, in Proc. IAU Symp. 131, Planetary Nebulae, ed. S. Torres-Peimbert (Kluwer, Dordrecht), 463

Schwarz, H. E., Corradi, R. L. M., & Melnick, J., 1992, A&AS, 96, 23

Shklovsky, I. S. 1978, Stars – Their Birth, Life, and Death, (San Francisco: Freeman), 194

Stasinska, G., Tylenda, R., Acker, A., & Stenholm, B., 1991, ApJ, 247, 173

Taylor, A. R., Gussie, G. T. & Pottasch, S. R. 1990, ApJ, 351, 515

Terzian, Y., Balick, B., & Bignell, C. 1974, ApJ, 188, 257

Tylenda, R., Acker, A., Stenholm, B., & Köppen, J. 1992, A&AS, 95, 337

Volk, K., and Kwok, S. 1985, A&A, 153, 79

Weidemann, V. 1987, A&A, 188, 74

Weidemann, V. 1989, A&A, 213, 155

Weidemann, V. & Koester, D. 1983 A&AS, 121, 77

Weinberger, R. 1989 A&AS, 78, 301

Zhang, C. Y. & Kwok, S. 1993, ApJS, 88, 137

Zijlstra, A. A., Pottasch, S. R., & Bignell, C. 1989, A&AS, 79, 329

Zuckerman, B. & Gatley, I. 1988, ApJ, 324, 501

Zuckerman, B., Kastner, J. H., Balick, B. & Gatley, I. 1990, ApJL, 356, L59 Acker, A., Marcout, J., Ochsenbein, F., Björn, S., & Romuald, T. 1992, Strasbourg–ESO Catalogue of Galactic Planetary Nebulae (European Southern Observatory: Munich, Germany)